CHARMONIUM DIPION TRANSITIONS

A Dissertation

Presented to the Faculty of the Graduate School

of Cornell University

in Partial Fulfillment of the Requirements for the Degree of

Doctor of Philosophy

by

James M^{c}Millin Hunt

February 2010

CHARMONIUM DIPION TRANSITIONS

James M^{c}Millin Hunt, Ph.D.

Cornell University 2010

Using a 7-dimensional unbinned likelihood fitter, we optimize decay amplitudes describing $e^+e^- \to \psi(2S) \to \pi\pi J/\psi$; $J/\psi \to e^+e^-$, $\mu^+\mu^-$ in 696,000 signal events collected by the CLEO-c detector at the Cornell Electron Storage Ring. The Kappa Model, which assumes a double gluon E1$\times$E1 operator and low-energy pion constraints, has an optimal value of $\kappa = 0.2740 \pm 0.0006_{\mathtt{stat}} \pm 0.0009_{\mathtt{sys}}$ but fails conservative χ^2 tests on histograms of projected quantities. Fitting three other models, one with final state interactions between the pions, one with $^3S_1 - {}^3D_1$ mixing and M1$\times$M1 gluons, and one with only pion constraints, moderately reduces χ^2 values. After a restriction to $\Delta m_{\mathtt{spin}} = 0$ transitions, we fit for the magnitude of the $\mathcal{D}/\mathcal{S}$ amplitude ratio in bins of $\mathtt{mass}(\pi\pi)$. Fits for the corresponding phase are not reliable due to a lack of sensitivity. Disallowing this phase while still assuming $\Delta m_{\mathtt{spin}} = 0$, we fit a quasi model-independent parameterization and obtain our best fit quality.

BIOGRAPHICAL SKETCH

James M^{c}Millin Hunt was born in Boston on February 11, 1982. He received his BA from Princeton University in 2004.

for my parents

ACKNOWLEDGEMENTS

When I entered graduate school, the physics department was merely part of Cornell University. Five years later, I now view it as an institution. Experiences changed my perception. I was sitting in David Cassel's office listening to stories about the great Hans Bethe. Jim Alexander provided valuable graduate career advice. David Kreinic found, in his office, the 20-year-old CBX document that I needed. On the plane back from Switzerland, Anders Ryd gave me a lecture on B decays. Peter Wittich and Julia Thom taught me the details of identifying $t \to Wb$ decays. Brian Heltsey and Hanna Mahlke revealed the intricacies of kinematic fitting with photons. Using sheer force of will, Dan Peterson would eventually convert me to drift-chamber-tracking with FORTRAN. Rich Galik, in our weekly meetings, guided me through the adventure that was the $\psi(2S) \to \pi\pi J/\psi$ analysis. In the office and down the hall, always with support, entertaining Root stories, and physics related insights were Souvik Das, Richard Gray, Dan Hertz, James Ledoux, Peter Onyisi, and Xin Shi. These are the colleagues that I shall never forget.

Movie nights were often spontaneous. A mass email would be sent out. Some would complain about being busy; some would delight at the perfect timing. The usual volunteers would compete for the title of master chef. A driver for the Wegman's run would materialize. Movies would be suggested. And just as the day's work would end, our house would be invaded by: Allison Bailey, Kevin Gillard, Sarah Hansen, Kristel Keegan, Ji-Min Kim, Aimee Krauss, Aaron Lenfestey, Fang Liu, Ryan Peterson, Megan Saucke, Marguerite Shaffer, Emmanuel Sharef, Mark Thomas, Ymir Vigfusson, Caroline Wee, and Yisong Yue. These are the friends I shall never forget.

TABLE OF CONTENTS

LIST OF TABLES

LIST OF FIGURES

CHAPTER 1

CLEO AND CESR

For the last 30 years, with contributions from a dozen institutions and hundreds of scientists, not to mention millions of taxpayer dollars, the CLEO collaboration has designed, implemented and analyzed the smashing of electrons and positrons. These collisions were manufactured to produce exotic states of matter, whose disintegrations could be compared with the predictions of theoretical physics. Confirmations, rare discoveries, and rigorous statistical analyses have been the subject of more than 500 journal publications. It was this dedicated effort that I had the opportunity to join as a graduate student at Cornell University. This dissertation serves as a record of an analysis, a measurement, that I was charged with performing on behalf of the collaboration.

The sub-atomic, sub-nuclear is a counter-intuitive world described by ad-hoc understandings developed from decades of experimental progress. When an electron (e^-) collides with a positron (e^+), the result is often the process, $e^+e^- \rightarrow e^+e^-$, where the two particles merely bounce off one another. Occasionally, a more complicated collision produces more than two outgoing particles. An example is figure 1.1, which provides a computer generated cross-section of a four particle event. The process is $e^+e^- \rightarrow \pi^+\pi^-\mu^+\mu^-$, where the electron and positron get converted into two charged pions ($\pi^\pm$), a muon (μ^-), and an anti-muon (μ^+). Far from science fiction, the computer image in figure 1.1 is fairly close to what the detector actually sees. The real mystery is the mechanism for converting two particles into four particles. It is as if two cannon balls were to collide in mid-flight, and instead of breaking into shrapnel, were to reassemble into four perfectly constructed baseballs.

A key property of these multiple-particle events is that they occur only when the e^+e^- pair has a very specific center-of-mass energy. Figure 1.2 plots the production rates of

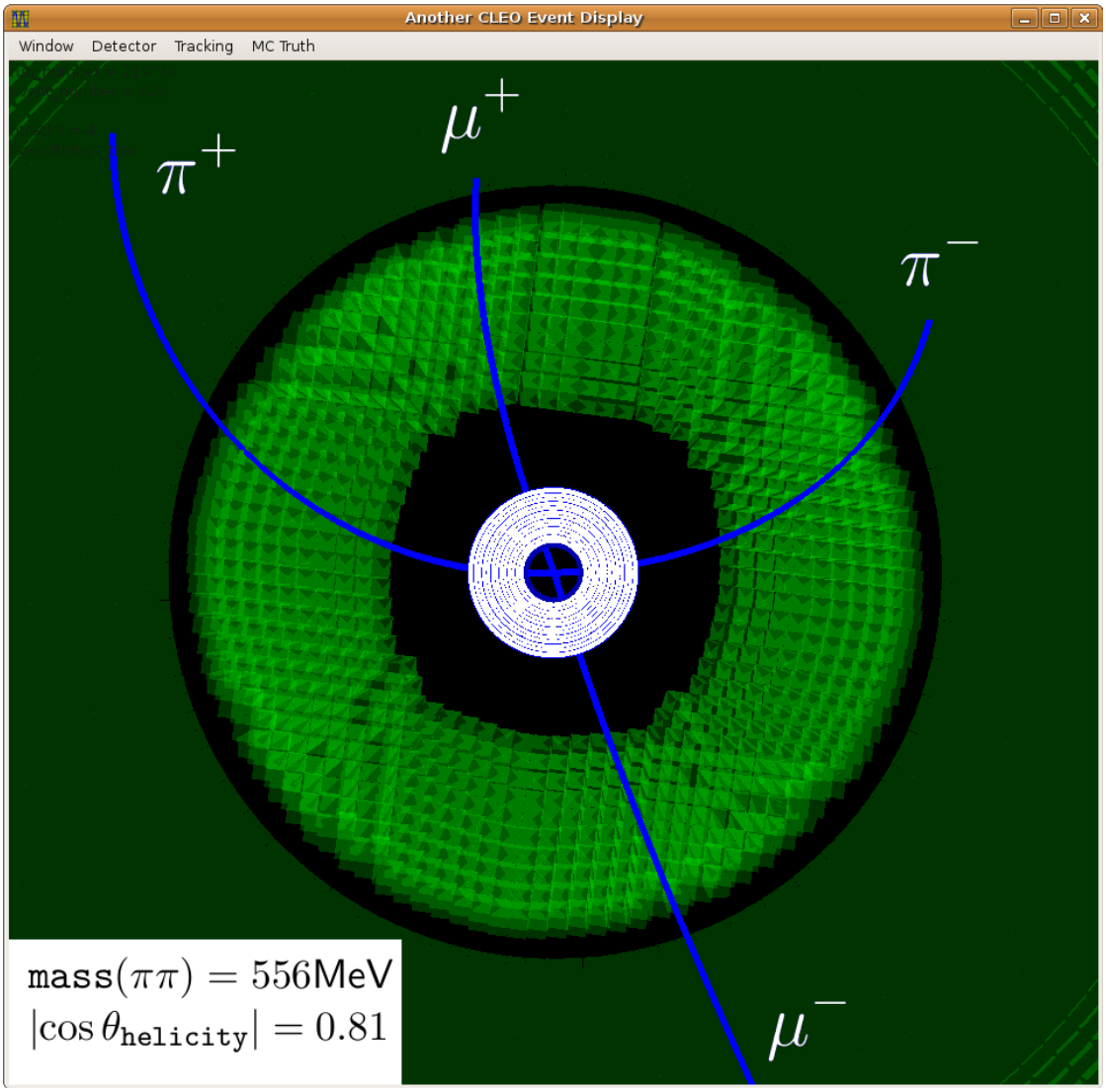

Figure 1.1: Monte Carlo event depicting $e^+e^- \to \psi(2S) \to \pi^+\pi^- J/\psi$; $J/\psi \to \mu^+\mu^-$.

multi-particle events as a function of center-of-mass energy. There are three distinct peaks, one at 9.44 GeV, one at 9.99 GeV and one at 10.33 GeV. The peaks represent the resonant processes, $e^+e^- \to b\bar{b}$, where the center-of-mass energy gets converted into a pair of bound b-quarks. The peak at the 9.44 GeV is the (vector) ground state, $b\bar{b}(1S)$, and the higher energy peaks are the (vector) $b\bar{b}(2S)$ and $b\bar{b}(3S)$. The modern names are the $\Upsilon(1S)$, $\Upsilon(2S)$, and $\Upsilon(3S)$.

These data were the first produced and collected at the newly built Cornell Electron

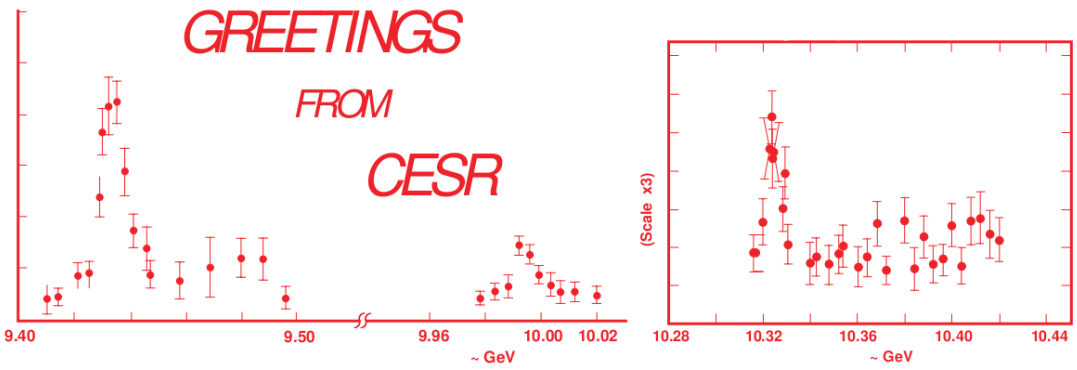

Figure 1.2: The 1979 CLEO Christmas Card plotting the production rates versus center-of-mass energy. The $\Upsilon(1S)$, $\Upsilon(2S)$, and $\Upsilon(3S)$ production peaks are visible from left to right.

Storage Ring (CESR) and CLEO detector. Figure 1.2 was a 1979 Christmas Card sent out by the CLEO collaboration in celebration of their re-discovery of the bottomonium states ($\Upsilon(nS)$, $n = 1, 2, 3$).

The CESR machine contains a linear accelerator, a synchrotron, and a storage ring (see figure 1.3). The entire process starts in a 150 KeV electron gun where electrons boil off of a hot filament. They then travel down a 30 meter linear accelerator reaching energies of 300 MeV. They are then sent into the synchrotron where they reach their target energies. Positrons are made by placing a tungsten target at the 150 MeV position in the linear accelerator. The electron-tungsten collisions produce a spray of particles, some of which are positrons. After being electromagnetically selected, the positrons are accelerated in the same fashion as the electrons (except in different directions).

Once in the single-pipe storage ring, the electrons and positrons are organized into "trains" of "bunches." The structure is maintained by super-conducting radio-frequency cavities, wiggler magnets, and over a hundred dipole and quadrupole magnets. Traveling in opposite directions, the bunches follow pretzel-like orbits in order to avoid undesired collisions. Only at one place, the interaction point, are the two trajectories focused into

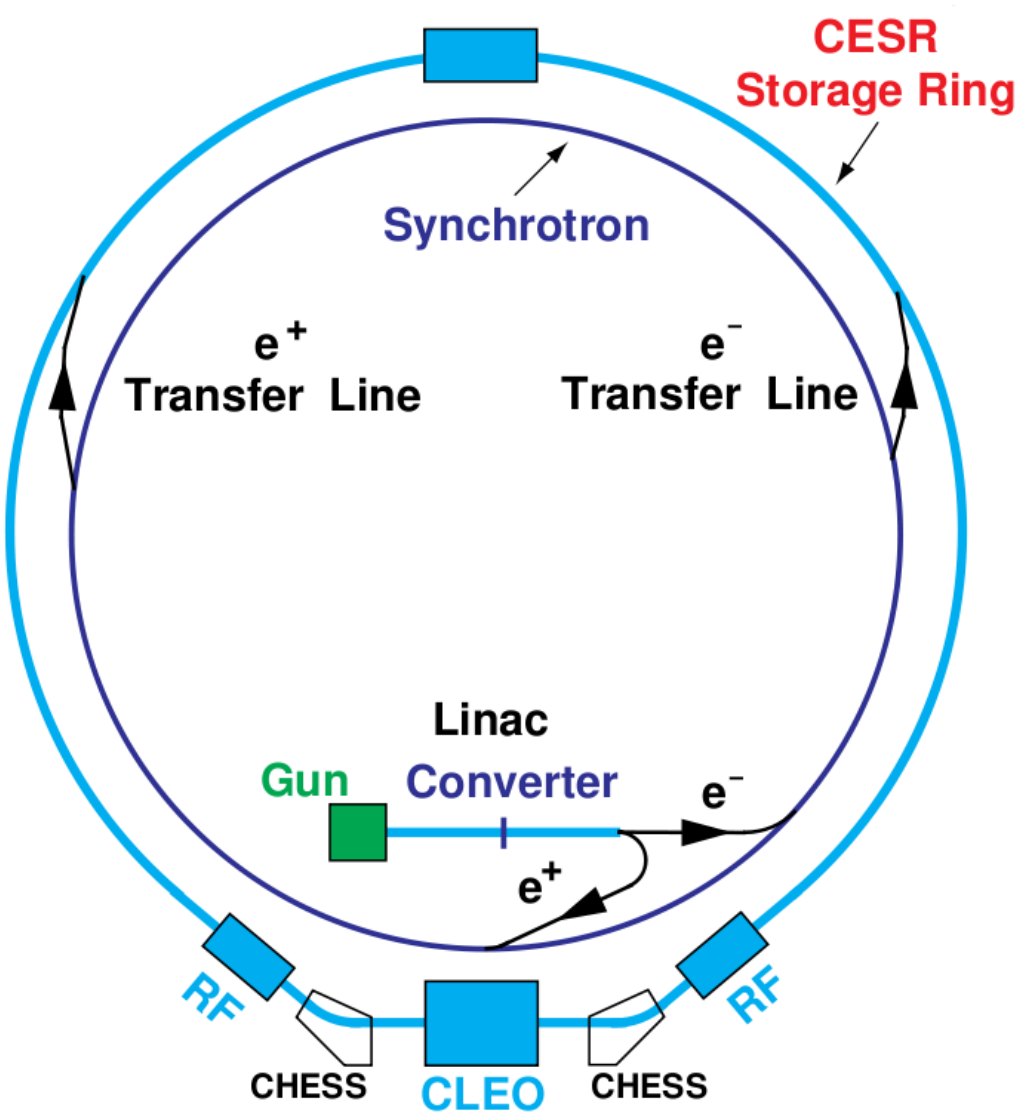

Figure 1.3: The Cornell Electron Storage Ring (CESR).

inevitable collisions.

At the interaction point, the e^+e^- collisions are surrounded by a massive three story structure, the CLEO detector. Over the years, this device has undergone numerous upgrades. The most recent version, CLEO-c, is shown in figure 1.4 and figure 1.5. The detector is designed to identify neutral and charged particles. The detector effectively takes a picture of the debris from e^+e^- collisions. The detector contains two drift cham-

bers, a crystal calorimeter and a Ring Imagining Cherenkov Detector (RICH). These major components are surrounded by a 1 Tesla axial magnetic field.

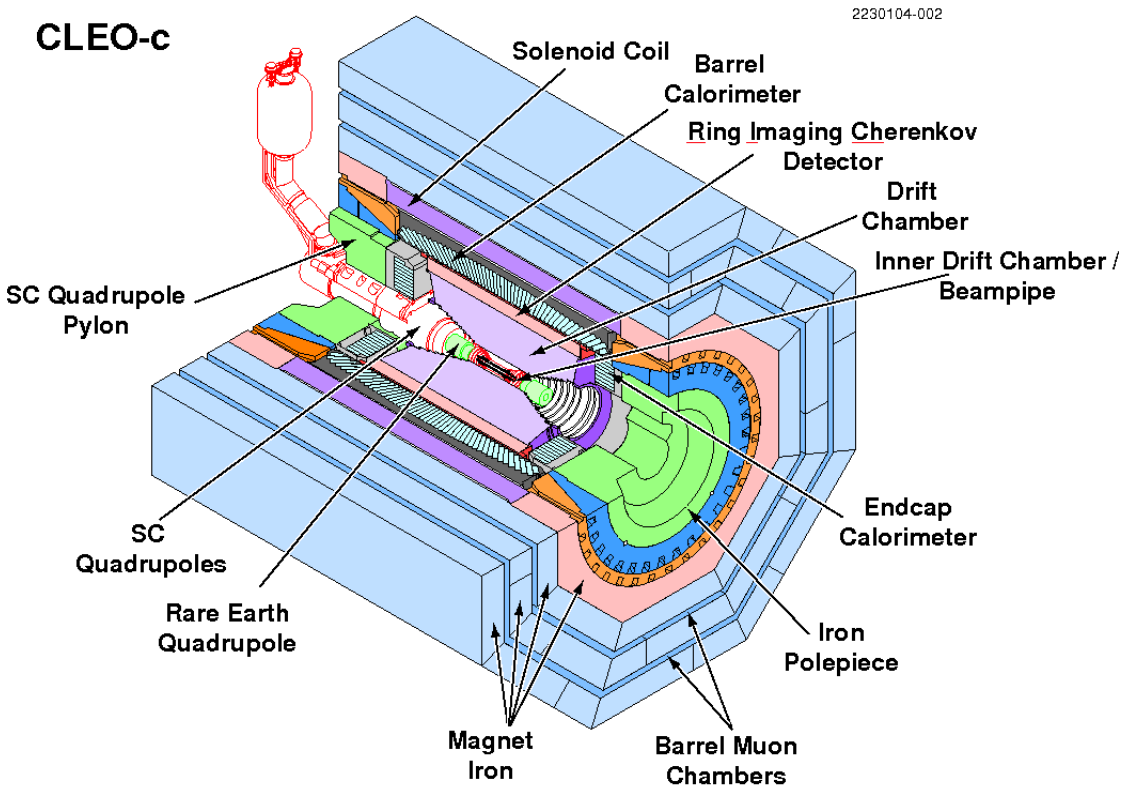

Figure 1.4: The CLEO-c detector.

Most relevant for my work are the two drift chambers and the crystal calorimeter. The drift chambers are designed to measure ionization of charged particles. The chambers contain helium-propane gas and a large number of near axial wires. Some of the wires are placed at high voltage, which creates regions of strong electric field. When a charged particle passes through the chambers, the ionization collides with the "sense" wires, and these are electrically read out. These signals, on wires with well-defined positions, provide "dots" that are then "connected" by reconstruction software. A full three-dimensional reconstruction (as opposed to two-dimensional) is possible because some of wires are given a small stereo angle. The result is an approximate helix that takes into account dE/dx information. The dE/dx information aids particle-id and the

helix provides a measurement of the particle's momentum.

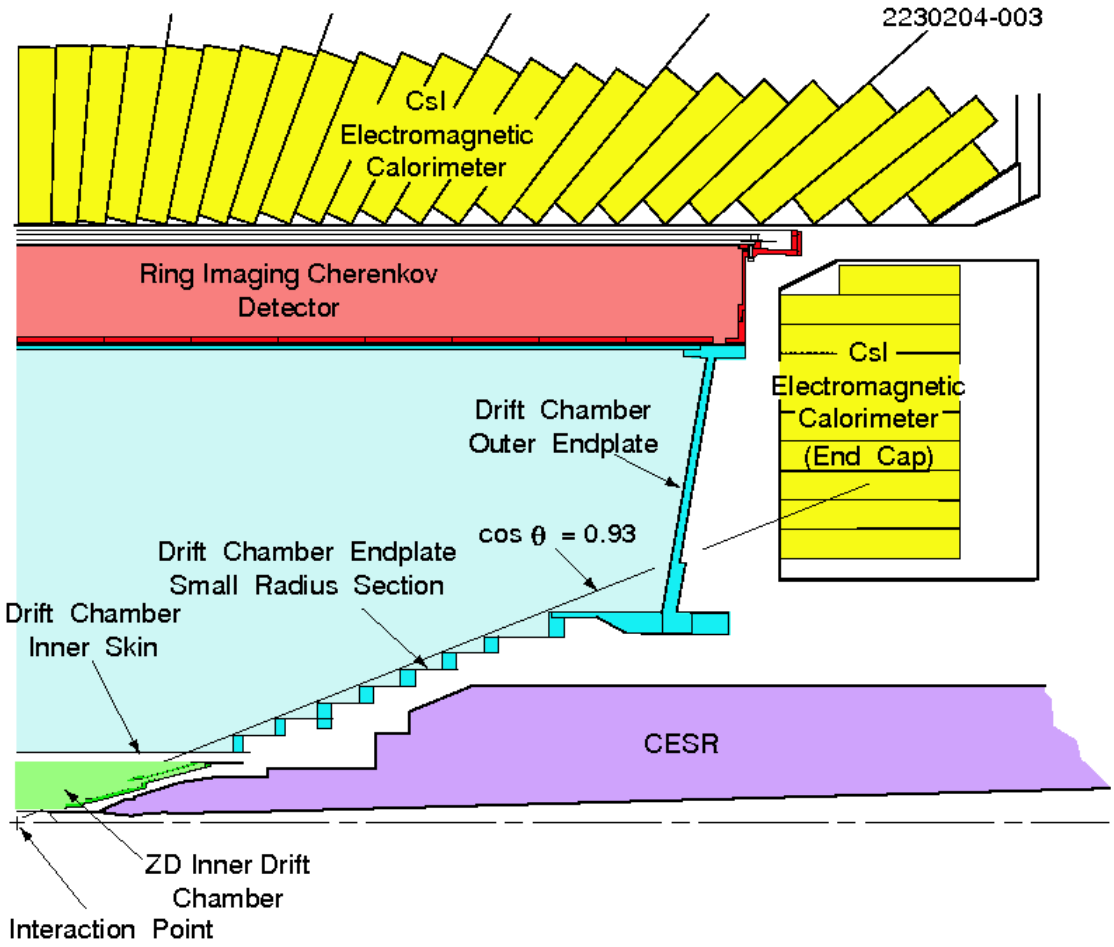

Figure 1.5: Side view of the CLEO-c detector.

The crystal calorimeter measures electromagnetic energy from photons and particle interactions. The nearly 8,000 crystals are made of thallium-doped cesium iodide. The deposited electromagnetic energy is read out by photodiodes mounted on the end of each crystal. When an energy deposit is aligned with a track from the drift chambers, reconstruction software can perform a rudimentary form of particle identification. The idea is to take the matched energy (E) and the momentum (p) of a track and compute the E/p ratio. Electrons typically have E/p values close to one while muons have E/p values closer to zero.

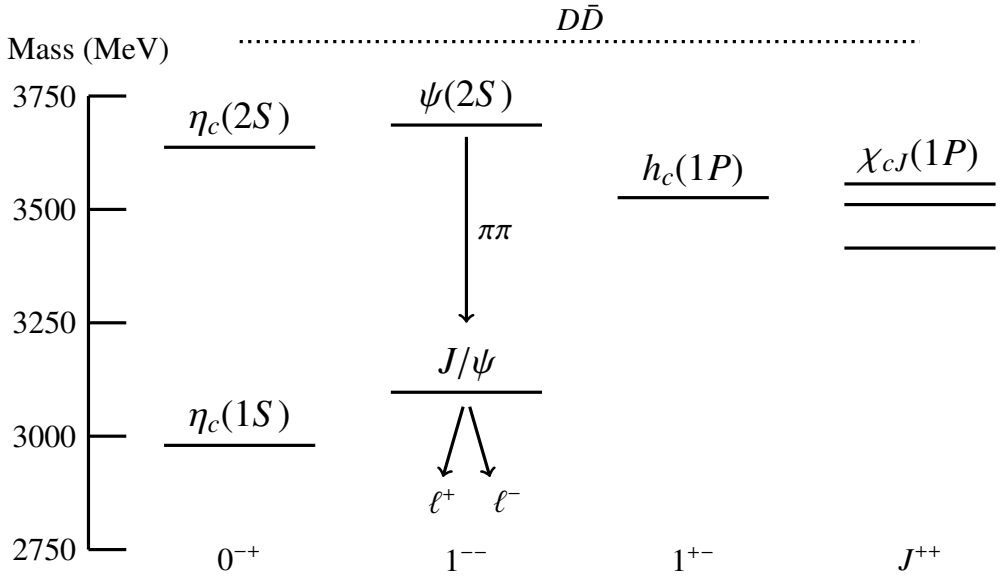

Figure 1.6: The Charmonium System.

In the final stage of the CLEO program, the center-of-mass energy was lowered to the charmonium regime and the detector was upgraded and renamed CLEO-c. Soon afterwords, I joined the CLEO collaboration under the advising of Rich Galik. One of the research topics that Rich suggested concerned the dipion transition within the charmonium system. CLEO had run at a center-of-mass energy of 3686 MeV, precisely the right energy for process $e^+e^- \to \psi(2S)$. Rich suggested we study $e^+e^- \to \psi(2S) \to \pi\pi J/\psi$ where $J/\psi \to e^+e^-, \mu^+\mu^-$. Figure 1.6 shows this transition within the charmonium system. It is the study of this reaction that we now turn.

CHAPTER 2

DIPION TRANSITIONS

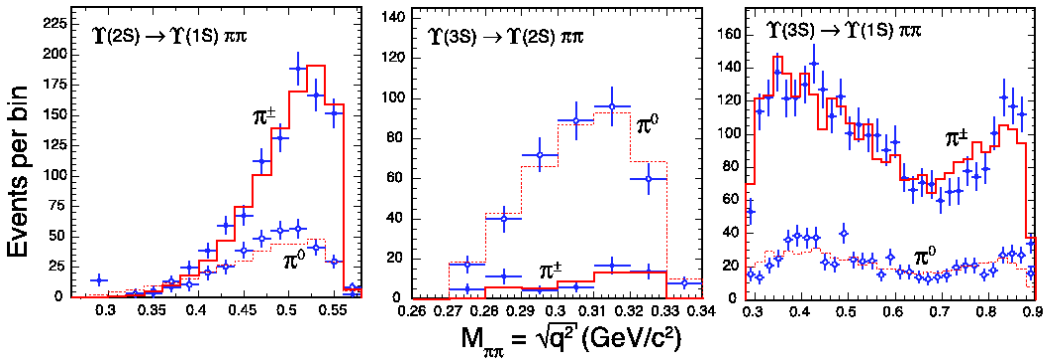

Figure 2.1: The single-peaking $\Upsilon(2S) \to \pi\pi\Upsilon(1S)$ and $\Upsilon(3S) \to \pi\pi\Upsilon(2S)$ along with the double-peaking $\Upsilon(3S) \to \pi\pi\Upsilon(1S)$. Plots are from a recent CLEO analysis [7].

The $\psi(2S) \to \pi\pi J/\psi$ [1, 2] decay is one of many observed dipion transitions between mesons. Started by $\eta' \to \pi\pi\eta$ [3], the group now includes $\psi(3770) \to \pi\pi J/\psi$ [4], $\chi_b(2P) \to \pi\pi\chi_b(1P)$ [5], eight[1] forms of $\Upsilon(nS) \to \pi\pi\Upsilon(mS)$, as well as $X(3872) \to \pi\pi J/\psi$ [11] and $Y(4260) \to \pi\pi J/\psi$ [12]. For two reasons, the relatively large branching fractions and ease of tagging the charged transitions, these decays often start both inclusive and exclusive measurements. Nevertheless, a problem persists in describing the decay dynamics. When sufficient statistics and phase space allow, these dipion transitions fall into two categories depending on the shape of their `mass`$(\pi\pi)$ distributions. For example, figure 2.1 shows the single-peaking $\Upsilon(2S) \to \pi\pi\Upsilon(1S)$ and $\Upsilon(3S) \to \pi\pi\Upsilon(2S)$ along with the double-peaking $\Upsilon(3S) \to \pi\pi\Upsilon(1S)$. The most common theoretical description, which we refer to as the `Kappa` Model, uses the QCD multipole expansion in conjunction with low-energy pion theorems, and predicts the single-peaking shape. The $\psi(2S) \to \pi\pi J/\psi$ decay, one of the single-peaking transitions and the subject of this analysis, was last examined by BES [2].

It is useful to write $\psi(2S) \to \pi\pi J/\psi$ as $\psi(2S) \to XJ/\psi$; $X \to \pi\pi$ in which X labels

[1] $2S \to 1S$ and $3S \to 2S, 1S$ [7, 8]; $4S \to 2S, 1S$ [9]; $5S \to 3S, 2S, 1S$ [10].

the $\pi\pi$ system. The mass of X, which we call q, is bounded above by $m_{\psi(2S)} - m_{J/\psi} \approx$ 589 MeV. The physical lower bound is $2m_{\pi^0} \approx 270$MeV or $2m_{\pi^\pm} \approx 280$MeV depending on whether the pions are neutral or charged. The experimental lower bound is set at 340 MeV, slightly above the physical lower bound, in order to avoid backgrounds from photon conversions where $\gamma \to e^+e^-$ fakes $\pi^+\pi^-$. Figure 2.2, on the left, shows this q-distribution from 340 MeV to 589 MeV in our `Data` and `Generic MC` after event selection. The peak at 550 MeV arises from an increasing squared absolute amplitude and a rapidly decreasing phase space factor.

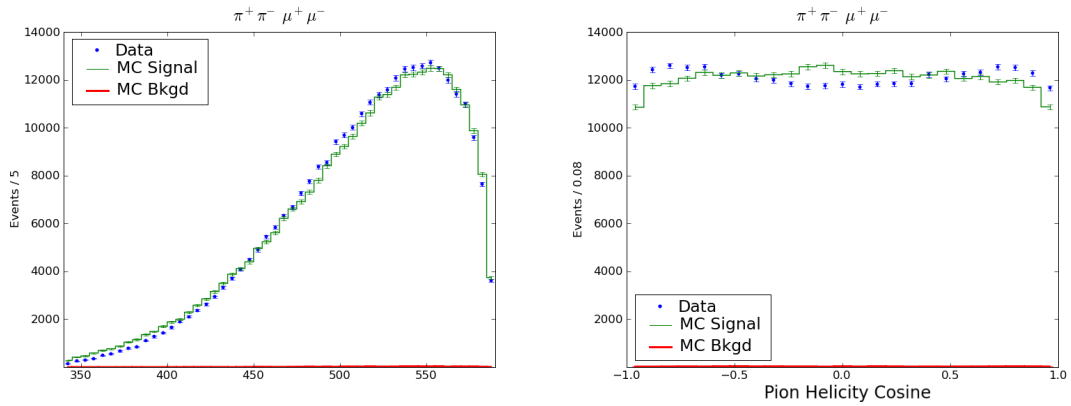

Figure 2.2: A comparison between our `Data` and `Generic MC` after event selection for $\psi(2S) \to \pi^+\pi^- J/\psi; J/\psi \to \mu^+\mu^-$. On the left is $q = \texttt{mass}(\pi\pi)$, and on the right is the pion helicity cosine. The `Generic MC` contains less than 0.25% background. Similar plots for the other channels are in figures 5.11 and 5.12 on pages 47 and 48.

In the X rest frame, where the pions are back-to-back, define the *negative* z-axis as pointing back toward the decayed $\psi(2S)$. The *positive* z-axis is then the direction of flight of the X as viewed from the $\psi(2S)$ rest frame. Still in the X rest frame, we define the *pion helicity angle* as the angle between the π^+ and the *positive* z-axis. This angle is useful because it gives information on the spin structure of the X system. In the language of the helicity spin formalism, an X with spin J and helicity λ has a decay amplitude proportional to $d^J_{0\lambda}(\cos\theta_{\text{helicity}})$. For $\pi^0\pi^0$ transitions, we compute a similar quantity by taking the angle between the higher energy π^0 and the z-axis. The absolute value of the

cosine of this angle has the same interpretation as the absolute value of the pion helicity angle (defined only for $\pi^+\pi^-$ transitions). Figure 2.2, on the right, compares the cosine of the pion helicity angle in our `Data` and `Generic MC` after event selection. The decay model in the `Generic MC` assumes a scalar X and produces a uniform $\cos\theta_{\text{helicity}}$ at the level of `MC-Truth`, and appears non-uniform because of efficiency distortion. The disagreement between our `Data` and `Generic MC` is evidence for X having non-scalar components.

Since the $\psi(2S)$ and J/ψ are iso-scalars, and $\psi(2S) \to XJ/\psi$ is a strong decay, one expects $I(X) = 0$. This assumption is experimentally verified by measuring the $\mathcal{B}(\psi(2S) \to \pi^0\pi^0 J/\psi)/\mathcal{B}(\psi(2S) \to \pi^+\pi^- J/\psi)$ ratio. Neglecting $m_{\pi^0} \neq m_{\pi^+}$ phase space corrections, $I(X) = 0$, 1, and 2 imply ratios of 0.5, 0, and 2 respectively. The recent CLEO measurement [13] puts the ratio at $0.5047 \pm 0.0022 \pm 0.0102$, which is only consistent with an iso-scalar X. Combining this iso-scalar assumption with $\psi(2S)$ and J/ψ having $I^G(J^{PC}) = 0^-(1^{--})$ requires X to have $I^G(J^{PC}) = 0^+(\text{even}^{++})$. In this language, the pion helicity cosine distribution suggests that $\psi(2S) \to XJ/\psi$ proceeds mostly through $J^{PC}(X) = 0^{++}$ with a small contribution from $J^{PC}(X) = 2^{++}$. The shape of the q-distribution and inconsistency of a scalar X are well known features of the $\psi(2S) \to \pi\pi J/\psi$ transition. And as we will see below, most theoretical models also predict these two features. But from an experimental perspective, the predicted angular correlations have yet to receive a thorough experimental vetting. Part of the problem is the vector nature of the $\psi(2S)$ and J/ψ, which requires the matrix elements to contain both kinematic and spin components. In other words, the analysis must use the spin information in the decay of the J/ψ. Using about 696,000 essentially background-free events of the form $\psi(2S) \to \pi^+\pi^+(\mu^+\mu^-)$, $\pi^+\pi^+(e^+e^-)$, $\pi^0\pi^0(\mu^+\mu^-)$, and $\pi^0\pi^0(e^+e^-)$, this analysis uses an unbinned likelihood fitter that takes into account all angular correlations.

CHAPTER 3

ANALYSIS OVERVIEW

We begin with an overview of the analysis. Later sections will elaborate on our procedures and conclusions.

Event selection starts by selecting two- or four-track events allowing for both $\psi(2S) \to \pi^0\pi^0 J/\psi$ and $\pi^+\pi^- J/\psi$. The two tracks or two highest-momentum tracks are candidates for leptons in $J/\psi \to e^+e^-$ or $\mu^+\mu^-$, must be oppositely charged, are electron-like or muon-like depending on E/p values, and must pass a kinematic `1C` fit to the J/ψ mass. Calorimeter showers aligned within 100 mrad of a lepton track , presumably arising from Bremsstrahlung or final state radiation, are included in the mass fit.

The remaining two tracks in the four-track events must be oppositely charged, are assumed to be charged pions, and are combined with the fitted J/ψ in a kinematic `4C` fit to the `LabNet4Momentum`. The two-track events must provide showers such that two π^0 candidates, when combined with the fitted J/ψ, can pass a kinematic `4C` fit to the `LabNet4Momentum`. Multiple candidates are disambiguated by choosing the $\pi^0\pi^0$ pair with the lowest $\chi^2_{\texttt{fit}}/d.o.f.$ in the `4C` kinematic fit.

Event selection results in about 696,000 events evenly split between electrons and muons with a charged to neutral ratio of 5.1 to 1. Backgrounds are negligible and arise from non-e, μ two-body decays of the J/ψ (mainly from $J/\psi \to \pi^+\pi^-$).

We fit for shape parmeters in six decay models. The first model, referred to as the `Kappa` Model, is parameterized by κ, is the lowest order theoretical decay amplitude, and takes the covariant form,

$$\mathcal{M} \propto \left[\left(q^2 + m_\pi^2\right) - \kappa\left(1 + \frac{2m_\pi^2}{q^2}\right)\left(\frac{(q \cdot P')^2}{P'^2} - \frac{1}{4}q^2\right) + \frac{3\kappa}{2}\frac{l_{\mu\nu}P'^\mu P'^\nu}{P'^2}\right](\epsilon' \cdot \epsilon)\,. \qquad (3.1)$$

The fourvectors, q^μ and P^μ, represent X and $\psi(2S)$ respectively. The $l_{\mu\nu}$ tensor represents $J^{PC}(X) = 2^{++}$. It is the symmetric, traceless, space-like object formed from the pion fourvectors, and has definition (see appendix on page 106),

$$l^{\mu\nu} = r^\mu r^\nu + \frac{1}{3}\left(1 - \frac{4m_\pi^2}{q^2}\right)\left(q^2 g^{\mu\nu} - q^\mu q^\nu\right) \qquad \text{where} \quad q^\mu = q_1^\mu + q_2^\mu \text{ and } r^\mu = q_1^\mu - q_2^\mu. \quad (3.2)$$

The common fitting approach would write the above amplitude in terms of a small set of kinematic variables, simulate the reconstruction efficiency in these variables, and perform a (binned) fit in these variables for the unknown parameter κ. We do not work within this paradigm.

Our unbinned likelihood fitter evaluates absolute squared amplitudes directly from fourvectors avoiding any intermediate set of kinematic variables. Instead of simulating the point-wise efficiency, $\epsilon = \epsilon(p_{\pi_1}^\mu, p_{\pi_2}^\mu, p_{\ell^+}^\mu, p_{\ell^-}^\mu)$, which would require "infinite" computational resources, we exploit an algebraic trick that writes the likelihood entirely in terms of integrated efficiency terms, quantities that are efficiently computed from `MC`. For each model that we fit, we merely transcribe their covariant form into `C++`, without having to worry about Clebsch-Gordan coefficients or helicity formalisms.

Our fitter computes the optimal parameter value(s), symmetric errors and asymmetric errors for each of the four channels, $\pi^+\pi^-(\mu^+\mu^-)$, $\pi^+\pi^-(e^+e^-)$, $\pi^0\pi^0(\mu^+\mu^-)$, and $\pi^0\pi^0(e^+e^-)$, as well as the combined channels $\pi^+\pi^-(\ell^+\ell^-)$, $\pi^0\pi^0(\ell^+\ell^-)$, and $\pi\pi(\ell^+\ell^-)$. The fit results for the `Kappa` Model are in figure 3.1. The four independent channels are in statistical agreement in the sense that the χ^2 has a `p-value` equal to 16%. We view

the the neutral transitions as a systematic check on the charged transitions, whose fit result is $\kappa_{\pi^+\pi^-(\ell^+\ell^-)} = 0.2740 \pm 0.0006_{\texttt{stat}}$ (the third entry from the bottom in the table). This result is larger than the BES result [2] of $\kappa = 0.183 \pm 0.002 \pm 0.003$ (there is a qualification in this comparison, see page 90).

channel	κ	stat error
$\pi^+\pi^-(\mu^+\mu^-)$	0.2744	0.0009
$\pi^+\pi^-(e^+e^-)$	0.2735	0.0009
$\pi^0\pi^0(\mu^+\mu^-)$	0.2732	0.0021
$\pi^0\pi^0(e^+e^-)$	0.2785	0.0021
$\pi^+\pi^-(\ell^+\ell^-)$	0.2740	0.0006
$\pi^0\pi^0(\ell^+\ell^-)$	0.2757	0.0015
$\pi\pi(\ell^+\ell^-)$	0.2743	0.0006

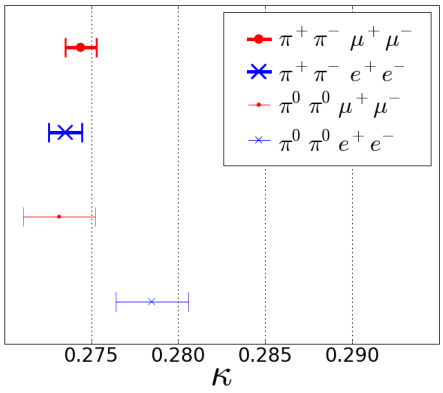

Figure 3.1: Fit results for the `Kappa` Model in our `Data`. The quoted errors are the symmetric, statistical errors as computed by the likelihood fitter.

We estimate systematic error with a simulation of resolution smearing, a study of cut variation, and a data-driven reweighting of pion tracking efficiency. For the `Kappa` Model, these three contributions in the $\pi^+\pi^-(\ell^+\ell^-)$ channel are 0.0006, 0.0002, and 0.0007 respectively, giving rise to our final result of $\kappa_{\pi^+\pi^-(\ell^+\ell^-)} = 0.2740 \pm 0.0006_{\texttt{stat}} \pm 0.0009_{\texttt{sys}}$. The result for the $\pi^0\pi^0$ transitions is $\kappa_{\pi^0\pi^0(\ell^+\ell^-)} = 0.2757 \pm 0.0015_{\texttt{stat}} \pm 0.0035_{\texttt{sys}}$.

The fitter, by the nature of a likelihood fit, does not produce a goodness of fit statistic. We proceed by reweighting phase space `MC` by our models evaluated at their optimal parameter(s). We then compare these pseudo-datasets with our `Data` by performing χ^2 tests on histograms of projected kinematic quantities. Somewhat surprisingly, the `Kappa` Model fails these χ^2 tests with infinitesimal `p-values`.

We explore this discrepency by fitting three other theoretical models. The first adds to the Kappa Model a q-linear-dependent relative phase shift between $J^{PC}(X) = 0^{++}$ and $J^{PC}(X) = 2^{++}$ (we call this the KappaFSI Model). The second starts with the Kappa Model and allows for ${}^3S_1 - {}^3D_1$ mixing and M1 $\times$ M1 gluons (Voloshin Model). The third weakens the Kappa Model by allowing for all multipole terms (ABCλ Model). We are surprised how these extra degrees of freedom do little to improve fit quality.

Without an adequate description of our Data , we next develop a quasi-model independent parametrization that passes χ^2 tests. One of our assumptions in this model is the irrelevance of FSI in the descriptions of our Data . This is motivated by a fit for the $\mathcal{D}/\mathcal{S}$ amplitude ratio in bins of mass($\pi\pi$) where MC simulations reveals a lack of sensitivity to the phase of the complex ratio (statistical fluctuations are too large for us to claim a non-zero fitted phase).

We summarize with three conclusions. First, the Kappa Model has an optimal parameter that is statistically different from the BES result but does not pass χ^2 tests (the fit quality is poor). Second, higher order theoretical corrections do not describe the discrepency between our Data and the Kappa Model. Third, we offer a quasi-model independent paramatrization (QMI) that describes our Data . This parameterization should aid future theoretical work and the development of MC packages.

The most important plot is in figure 8.6 on page 98. It shows the Kappa, VVPIPI and QMI Models for $\pi^+\pi^-(\ell^+\ell^-)$. The plot reveals precisely how the Kappa Model fails to properly model our Data .

CHAPTER 4

MODELS

Section 4.1 starts by describing VVPIPI, the decay model in EvtGen. Section 4.2 then provides some historical context by outlining the partial wave technique of Robert Cahn. The six decay models that we optimize are then discuessed. The ABCλ Model is in section 4.3. The Kappa Model is in section 4.4. The Voloshin Model is in section 4.5. The KappaFSI Model is in section 4.6.1 The $\mathcal{D}/\mathcal{S}$ ratio fit is in section 4.6.2, and the QMI Model is in section 4.7.

For reference, we provide a table of kinematic symbols.

Table 4.1: Kinematic Symbols

Symbol	Definition
P' or P'^{μ}	Fourvector of $\psi(2S)$
P or P^{μ}	Fourvector of J/ψ
q_1 or q_1^{μ}	Fourvector of π^+ or higher energy π^0
q_2 or q_2^{μ}	Fourvector of π^- or lower energy π^0
X	$\pi\pi$ system
q^2	Squared Mass of X
m_π	Charged or Neutral Pion mass (depends on context)
q	Mass or Fourvector of X (depends on context)
q^{μ}	Fourvector of X
r or r^{μ}	$q_1^{\mu} - q_2^{\mu}$
$l^{\mu\nu}$	$r^{\mu}r^{\nu} + \frac{1}{3}\left(1 - \frac{4m_\pi^2}{q^2}\right)\left(q^2 g^{\mu\nu} - q^{\mu}q^{\nu}\right)$
ϵ' or ϵ'^{μ}	Polarization Fourvector of $\psi(2S)$
ϵ or ϵ^{μ}	Polarization Fourvector of J/ψ
$\epsilon^{\mu\nu}$	$\epsilon'^{\mu}\epsilon^{\nu} + \epsilon^{\mu}\epsilon'^{\mu} + \frac{2}{3}(\epsilon' \cdot \epsilon)\left(\frac{P'^{\mu}P'^{\nu}}{P'^2} - g^{\mu\nu}\right)$

4.1 `VVPIPI` Model

The `VVPIPI` model is the standard way to implement $\psi(2S) \to \pi\pi J/\psi$ inside of EvtGen. The model implements the decay according to,

$$\mathcal{M}(\psi(2S) \to \pi\pi J/\psi) \propto \underbrace{\left(q^2 - 4m_\pi^2 \right)}_{\text{mass distribution}} \times \underbrace{\left(\epsilon' \cdot \epsilon \right)}_{\text{spin alignment}}. \tag{4.1}$$

To start with, notice how the model assumes the kinematic and spin pieces factorize. The spins of the $\psi(2S)$ and J/ψ are then aligned (via the dot product between polarization fourvectors). The kinematic factor, far from being a Breit-Wigner, introduces a q-dependence that favors high invariant mass. Experimentally, the `VVPIPI` model has two major problems. The first is how the q-distribution first overestimates, then underestimates, and then overestimates data as q increases (figure 2.2, on the left). Secondly, since the `VVPIPI` model is a function of the fourvector of X but in no way distinguishes the individual pions, the X system is treated as a scalar. But this is at odds with experimental data (figure 2.2, on the right).

4.2 Partial Waves According to Cahn

Now what may not be immediately obvious is that there are many different ways to couple $J^{PC}(X) = 2^{++}$ to the $\psi(2S)$ and J/ψ. Speaking very generally, you can add a spin-2 component to `VVPIPI` by modifying the spin part, or by modifying the mass distribution, or by modifying both. Cahn [14] was the first to propose a systematic way of analyzing this decay. His perspective starts by pulling out the polarizations of the vector particles,

$$\mathcal{M}(\psi(2S) \to \pi\pi J/\psi) = \epsilon'_{\mu}\epsilon_{\nu}\mathcal{M}^{\mu\nu}. \tag{4.2}$$

This expression says that $\mathcal{M}$ should really be thought of as containing two Lorentz indices. Next, without loss of generality, use the pion fourvectors, written as q_1^μ and q_2^μ or as the combinations $q^\mu = q_1^\mu + q_2^\mu$ and $r^\mu = q_1^\mu - q_2^\mu$, to factor out the Lorentz indices in exchange for the introduction of *five* form factors,

$$\mathcal{M}^{\mu\nu} = \mathcal{A}g^{\mu\nu} \; + \; \mathcal{B}q^\mu q^\nu \; + \; \mathcal{C}q^\mu r^\nu \; + \; \mathcal{D}r^\mu q^\nu \; + \; \mathcal{E}r^\mu r^\nu. \tag{4.3}$$

Why are there five form factors? A simple answer (provided by Cahn) is to consider the crossed reaction $\psi(2S)\pi \to J/\psi\pi$ and notice how there are five unique helicity amplitudes ($\langle\lambda_{\psi(2S)}|\lambda_{J/\psi}\rangle = \langle 1|1\rangle$, $\langle 1|0\rangle$, $\langle 1|-1\rangle$, $\langle 0|1\rangle$, $\langle 0|0\rangle$ and the other helicity amplitudes are related by parity). Each of the five form factors is then a function of any scalar invariants left in the problem. There are two of them, one of which can be q. If the $\psi(2S)$ has fourvector P', a second invariant can be $P' \cdot r$, which is proportional to the difference in pion energies as viewed from the $\psi(2S)$ frame. We are saying that $\mathcal{A} = \mathcal{A}(q, P' \cdot r)$, $\mathcal{B} = \mathcal{A}(q, P' \cdot r)$, etc.

In order to simplify the analysis, Cahn diagonalized the system with respect to the spin of X, denoted by $\vec{l}$, and the orbital angular momentum between X and the J/ψ, denoted by $\vec{L}$ (see figure 4.1). In terms of the six helicity angles, Ω_π, $\Omega_{J/\psi}$, and Ω_{l^+}, the spins of the $\psi(2S)$ and J/ψ denoted by $\vec{s'}$ and $\vec{s}$ (both of which are of unit magnitude), the total final state spin $\vec{S} \equiv \vec{l} + \vec{s}$, and the net helicity of the muons denoted by λ, the partial wave expansion is,

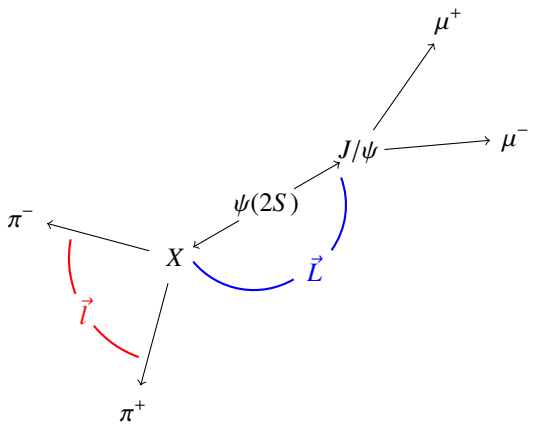

Figure 4.1: Nonrelativistic Partial Wave Expansion in terms of $\vec{L}$ and $\vec{l}$.

$$\langle \pi\pi J/\psi|\mathcal{M}|\psi(2S)\rangle = \sum_{\substack{l,L,S;\\ l_z,L_z,S_z}} \mathcal{M}_{l,L,S} \times \langle 1, s'_z|L, L_z; S, S_z\rangle\langle S, S_z|1, s_z; l, l_z\rangle \times D^{L*}_{L_z 0}\left(\Omega_{J/\psi}\right) D^{l*}_{l_z 0}\left(\Omega_\pi\right) D^{1*}_{s_z \lambda}\left(\Omega_{l^+}\right) \tag{4.4}$$

where the amplitudes, $\mathcal{M}_{l,L,S}$, are functions of only q. The final step introduces dynamics and argues that the infinite sum can be truncated after a few terms. Cahn recommended keeping the first three, $\mathcal{M}_{0,0,1}$, $\mathcal{M}_{0,2,1}$ and $\mathcal{M}_{2,0,1}$.

It is useful to enumerate the possible $\mathcal{M}_{l,L,S}$ amplitudes associated with X having definite spin. Start with the scalar case where $l = 0$. Parity always requires the orbital angular momentum, L, to be even. For $l = 0$, there are only two options, either $L = 0$ or $L = 2$. In these cases, the total spin $\vec{S}$, the angular momentum sum of $\vec{l}$ and the spin of the J/ψ, is always one. If L is zero or two, then $L + S$ can add up to one, the spin of the $\psi(2S)$. These two possibilities are tabulated in the first two rows of table 4.2. The case for $l = 2$ proceeds in the same fashion. Compute all possible (l, L, S) consistent with L being even and $s' = 1$. This exercise has the following conclusion. For any $l > 0$, there are *five* $\mathcal{M}_{l,L,S}$ values (see table 4.2). The switch from the five form factors

(eq. 4.3) to Cahn's partial wave expansion (eq. 4.4) is a replacement of the second scalar, $P' \cdot r$, with an infinite sum of $\vec{l}$ terms. It is effectively an expansion in terms of Legendre polynomials, followed by a basis change within each subspace of definite l (the $l = 0$ situation is a special case where some of the leading terms are zero). In other words, restricting the angular distributions to $l = 0$ or $l = 2$ allows for a total of $7 = 2 + 5$ amplitudes (seven $\mathcal{M}_{l,L,S}$), each of which is a function of q.

Table 4.2: Partial waves: $\vec{l}$ is the spin of the $\pi\pi$ system. $\vec{s'}$ and $\vec{s}$ are the spins of the $\psi(2S)$ and J/ψ. $S \equiv \vec{l} + s$ is the net spin. $\vec{L}$ is the orbital angular momentum between the $\pi\pi$ system and the J/ψ.

$\pi\pi$ spin	$\vec{l}$	$\vec{s}$	$\vec{S} \equiv \vec{l} + s$	$\vec{L}$	$\vec{s'} = \vec{S} + \vec{L}$	$\mathcal{M}_{l,L,S}$
spin-0	0	1	1	0	1	$\mathcal{M}_{0,0,1}$
spin-0	0	1	1	2	1	$\mathcal{M}_{0,2,1}$
spin-2	2	1	1	0	1	$\mathcal{M}_{2,0,1}$
spin-2	2	1	1	2	1	$\mathcal{M}_{2,2,1}$
spin-2	2	1	2	2	1	$\mathcal{M}_{2,2,2}$
spin-2	2	1	3	2	1	$\mathcal{M}_{2,2,3}$
spin-2	2	1	3	4	1	$\mathcal{M}_{2,4,3}$

4.3 ABCλ Model

How do theorists derive $\mathcal{M}_{l,L,S}$ from first principles? Brown and Cahn [15] were the first when in 1975 they used low-energy pion theorems to constrain the matrix elements. Their efforts resulted in what we refer to as the ABCλ model,

$$\mathcal{M} = \mathcal{A}\left(q^2 - 2m_\pi^2\right)(\epsilon' \cdot \epsilon) + \lambda m_\pi^2 (\epsilon' \cdot \epsilon) + \mathcal{B} E_1 E_2 (\epsilon' \cdot \epsilon) + C(\epsilon' \cdot q_1 \;\; \epsilon \cdot q_2 + \epsilon' \cdot q_2 \;\; \epsilon \cdot q_1). \tag{4.5}$$

Both λ, the so-called σ-term, and C, the "spin flip" term, were expected to be small. Notice how the $\mathcal{A}$ term is similar to but not identical to VVPIPI, which subtracts $4m_\pi^2$

instead of $2m_\pi^2$. The energies in the $\mathcal{B}$ term, E_1 and E_2, are the energies of the pions as viewed in the $\psi(2S)$ rest frame. If you try and relate E_1E_2 to the $\mathcal{M}_{l,L,S}$ amplitudes, you will discover that the $\mathcal{B}$ term contains a mixture of both $l = 0$ and $l = 2$ contributions. Furthermore, the mixing has a q-dependence (for details, see page 23 of CBX 06-31 [7]). Compare this to the C term, which explicitly relates the motion of the pions with the polarizations of the $\psi(2S)$ and J/ψ. Putting it a different way, any measurement that tries to differentiate the $\mathcal{B}$ term from the C term must model two complicated distributions, involving different types of spin-2 configurations.

4.4 Kappa Model

The next development was the QCD Multipole expansion, which could analyze the process before pion hadronization. Gottfried, Yan and many others (see references in [17]) argued that the $c\bar{c}$ transition from $2S \rightarrow 1S$ would have to be generated at lowest order by a double gluon E1 $\times$ E1 operator. When combined with the usual low-energy pion theorems, their argument led to a κ-parameterized amplitude,

$$\mathcal{M} \propto \left[\left(q^2 + m_\pi^2\right) - \kappa\left(1 + \frac{2m^2}{q^2}\right)\left(\frac{(q \cdot P')^2}{P'^2} - \frac{1}{4}q^2\right) + \frac{3\kappa}{2}\frac{l_{\mu\nu}P'^\mu P'^\nu}{P'^2}\right](\epsilon' \cdot \epsilon)\,. \tag{4.6}$$

This is the "Kappa Model" that was mentioned in the overview. The two fourvectors, P' and q, are for the $\psi(2S)$ and X respectively. The $l_{\mu\nu}$ tensor, represents $J^{PC}(X) = 2^{++}$, is symmetric, traceless, space-like and is a function of the pion fourmomenta,

$$l^{\mu\nu} = r^\mu r^\nu + \frac{1}{3}\left(1 - \frac{4m_\pi^2}{q^2}\right)\left(q^2 g^{\mu\nu} - q^\mu q^\nu\right) \qquad \text{where} \quad q^\mu = q_1^\mu + q_2^\mu \text{ and } r^\mu = q_1^\mu - q_2^\mu. \tag{4.7}$$

Since the Kappa Model and the ABCλ model use the same low-energy pion theorems, they should be related. This is indeed the case as the extra assumptions in the Kappa Model fully determine the ABCλ parameters,

$$\frac{\mathcal{B}}{\mathcal{A}}(\kappa) = \frac{-6\kappa}{1+\frac{3}{4}\kappa} \quad ; \quad \frac{C}{\mathcal{A}}(\kappa) = 0 \quad ; \quad \frac{\lambda}{\mathcal{A}}(\kappa) = \frac{3}{1+\frac{3}{4}\kappa}. \tag{4.8}$$

The need to divide out $\mathcal{A}$ is a consequence of the equality in eq. 4.5 and proportion in eq. 4.6.

By conventional wisdom, the Kappa Model is the best description of dipion transitions with single-peaking mass distributions. Notice how the E1 $\times$ E1 assumption requires the absence of the "spin-flip" C term. Later, we will fit for a non-zero value of C, which will add evidence for the inadequacy of the Kappa Model. But even when allowing for this ABCλ deviation from the Kappa Model, the fit quality will still be poor as judged from χ^2 values on projected quantities.

4.5 Voloshin Model

Meanwhile, back on the experimental side, other dipion transitions such as $\Upsilon(nS) \to \pi\pi\Upsilon(mS)$ complicated the picture by revealing two classes of transitions. The odd transitions, such as $\Upsilon(3S) \to \pi\pi\Upsilon(2S)$, were similar to $\psi(2S) \to \pi\pi J/\psi$. But the even transitions such as $\Upsilon(3S) \to \pi\pi\Upsilon(1S)$ disagreed with $\psi(2S) \to \pi\pi J/\psi$ by having a double-peaking q-distribution instead of a single-peaking q-distribution. There is no consensus on the nature of these double-peak dipion transitions. But for the sake of this analysis, we want to discuss a suggestion by Voloshin. He has argued [16] that the $\Upsilon(3S) \to \pi\pi\Upsilon(1S)$ transition may have E1 $\times$ E1 suppressed. If this is indeed the case,

then the shape of the amplitude may receive large contributions from ${}^3S_1 - {}^3D_1$ mixing and the M1 $\times$ M1 multipole term. His suggested amplitude contains the usual κ parameter, along with two new parameters, χ_2 and χ_m, describing the relative strength of the ${}^3S_1 - {}^3D_1$ mixing and magnetic transition respectively,

$$\begin{aligned}\mathcal{M} \propto & \left[(1-\chi_m)\left(q^2+m^2\right) - (1+\chi_m)\,\kappa\left(1+\frac{2m^2}{q^2}\right)\left(\frac{(q\cdot P')^2}{P'^2} - \frac{1}{4}q^2\right)\right](\epsilon'\cdot\epsilon) \\ & + (1+\chi_m)\,\frac{3}{2}\kappa\frac{l_{\mu\nu}P'^{\mu}P'^{\nu}}{P'^2}\,(\epsilon'\cdot\epsilon) \\ & - \left(\chi_2 + \frac{3}{2}\chi_m\right)\frac{\kappa}{2}\left(1+\frac{2m^2}{q^2}\right)q_\mu q_\nu \epsilon^{\mu\nu} \\ & - \left(\chi_2 + \frac{2}{3}\chi_m\right)\frac{3\kappa}{4}l_{\mu\nu}\epsilon^{\mu\nu} \qquad . \end{aligned} \tag{4.9}$$

The new symbol, $\epsilon_{\mu\nu}$, with definition,

$$\epsilon^{\mu\nu} = \epsilon'^{\mu}\epsilon^{\nu} + \epsilon^{\mu}\epsilon'^{\mu} + \frac{2}{3}\,(\epsilon'\cdot\epsilon)\left(\frac{P'^{\mu}P'^{\nu}}{P'^2} - g^{\mu\nu}\right), \tag{4.10}$$

is a spin-2 object representing the angular momentum sum of $\psi(2S)$ and $J/\psi(1S)$ projected onto $J = 2$, which originates from ${}^3S_1 - {}^3D_1$ mixing. The $\psi(2S) \to \pi\pi J/\psi$ decay, having a single peak q-distribution, should have "small" values of χ_2 and χ_m. This will indeed be the case, which, unfortunately, means that the `Voloshin` Model, just like the `Kappa` Model, will poorly describe our data.

So far, we have used the Cahn partial wave expansion to count degrees of freedom. And then we wrote down the `ABC`λ model, `Kappa` Model, and `Voloshin` Model in terms of covariant quantities. How are these two approaches related? For example, in the `Voloshin` Model there are four types of terms,

$$\epsilon' \cdot \epsilon \qquad l_{\mu\nu} P'^{\mu} P'^{\nu} \epsilon' \cdot \epsilon \qquad q_\mu q_\nu \epsilon^{\mu\nu} \qquad l_{\mu\nu} \epsilon^{\mu\nu}. \tag{4.11}$$

Whereas the partial wave discussion concluded that there are 7 possible terms with $l \leq 2$. If there are only 4 terms in the `Voloshin` Model, where are the other 3 terms? The answer is that they are predicted to be zero.[1] Part of confusion here is the notational difference between relativistic and non-relativistic models. For example, although it is possible to relate the `Voloshin` Model back to the $\mathcal{M}_{l,L,S}$ amplitudes, this exercise is algebraically tedious. The reason is that the Cahn expansion is non-relativistic, and as a result, it obfuscates the `Voloshin` Model's Lorentz invariance by acquiring complicated energy dependent $\mathcal{M}_{l,L,S}$ amplitudes. It is partly for this reason that we fit the `ABC`λ, `Kappa` and `Voloshin` Models, and do not fit the non-covariant Cahn partial waves.

4.6 Final State Interactions

Final state interactions between the pions are expected to play a role in the experimental study of $\psi(2S) \to \pi\pi J/\psi$. These final state interactions (FSI) are expected to add a relative q-dependent phase shift between $0^{++} \to \pi\pi$ and $2^{++} \to \pi\pi$. The amplitude for $\psi(2S) \to \pi\pi J/\psi$, before FSI take effect, may be written as,

$$\mathcal{M} = \mathcal{S} + \mathcal{D}. \tag{4.12}$$

The $\mathcal{S}$ and $\mathcal{D}$ terms are meant to represent $J^{PC}(X) = 0^{++}$ and $J^{PC}(X) = 2^{++}$. When

[1] Any additional terms, such as $q_\mu q_\nu l^{\mu\nu} q_\alpha q_\beta \epsilon^{\alpha\beta}$, would necessarily go as the fourth power of the pion momenta. One way to think of the `Voloshin` Model is a truncation of the expansion at second order in pion momenta. Recall that low-momenta pions are required for putting constraints on the hadronization of X. Now you might say that the pions in $\Upsilon(3S) \to \pi\pi\Upsilon(1S)$ are certainly not of low-momentum. Voloshin and the rest of the theoretical community are well aware of the problems with this approximation, but know of no other approach.

FSI are turned on, these two terms respectively receive an iso-scalar spin-0 phase shift, $\delta^{I=0}_{J=0}(q)$, and an iso-scalar spin-2 phase shift, $\delta^{I=0}_{J=2}(q)$,

$$\mathcal{S} \rightarrow e^{i\delta^{I=0}_{J=0}(q)}\mathcal{S}, \tag{4.13}$$

$$\mathcal{D} \rightarrow e^{i\delta^{I=0}_{J=2}(q)}\mathcal{D}. \tag{4.14}$$

The angular distributions in $\psi(2S) \rightarrow \pi\pi J/\psi$ should be sensitive to the q-dependent difference between these two phase shifts in the sense that,

$$|\mathcal{M}|^2 = |\mathcal{S}|^2 + \cos(\Delta\delta) \times 2\mathrm{Re}(\mathcal{S}\mathcal{D}) + |\mathcal{D}|^2 \qquad \text{where} \qquad \Delta\delta = \delta^{I=0}_{J=0}(q) - \delta^{I=0}_{J=2}(q). \tag{4.15}$$

The (arbitrary) q-dependence complicates the fitting procedure. There are basically two options, the first of which is to parameterize the q-dependence and float the parameters while fitting across all values of q. The second option is to perform a fit in bins of q, effectively allowing the q-dependence to be an arbitrary step-function. We try both methods.

4.6.1 `KappaFSI` Model

The first option is what we refer to as the `KappaFSI` Model. The idea is to take the `Kappa` Model and add a parameterized phase shift,

$$\mathcal{M} = \underbrace{\left[\left(q^2 + m_\pi^2\right) - \kappa\left(1 + \frac{2m^2}{q^2}\right)\left(\frac{(q\cdot P')^2}{P'^2} - \frac{1}{4}q^2\right)\right](\epsilon'\cdot\epsilon)}_{\mathcal{S}} + \underbrace{e^{-i\Delta\delta(q)}}_{\text{phase shift}}\underbrace{\frac{3\kappa}{2}\frac{l_{\mu\nu}P'^{\mu}P'^{\nu}}{P'^2}(\epsilon'\cdot\epsilon)}_{\mathcal{D}} \tag{4.16}$$

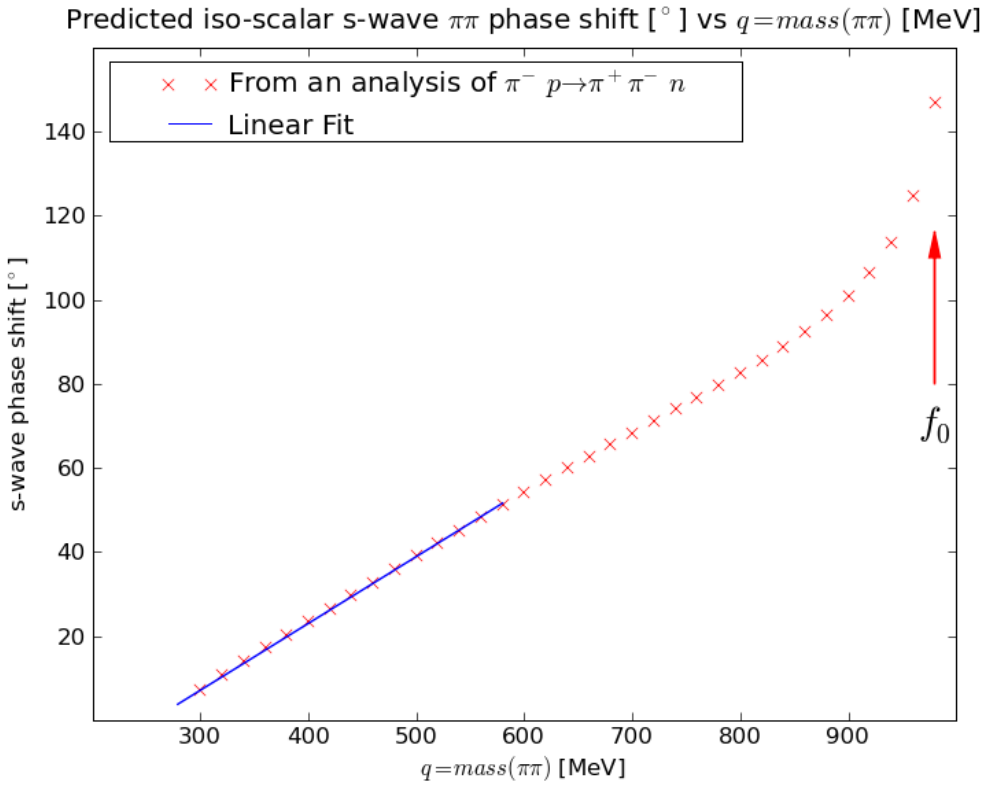

Figure 4.2: The iso-scalar spin-0 $\pi\pi$ phase shift as a function of q taken from an analysis [18] of $\pi^- p \to \pi^+\pi^- n$. The solid line is a linear fit in the mass range relevant to $\psi(2S) \to \pi\pi J/\psi$.

In order to parameterize the relative phase shift, $\Delta\delta = \delta^{I=0}_{J=0}(q) - \delta^{I=0}_{J=2}(q)$, we need to make assumptions about the spin-0 and spin-2 phase shifts. For spin-0, we turn to an analysis [18] of $\pi^- p \to \pi^+\pi^- n$, which uses analyticity and related arguments to extract phase shifts. Figure 4.2 plots the phase shift from one of their data tables, along with a linear fit in the mass range relevant to $\psi(2S) \to \pi\pi J/\psi$. The steep rise around 900 MeV is from the $f_0(980)$ resonance.[2] Although the spin-2 phase shift has never been measured, it is expected to be relatively constant and small in our mass range. Through personal correspondence, Mikhail Voloshin tells us that the spin-2 phase shift should be

[2]The possibility of another resonance below 900 MeV with $J^{PC} = 0^{++}$, namely the σ, is certainly relevant to shape of the phase shift. However, for lack of time, and because of the complicated nature of the physics, we avoid the σ in this analysis.

of order q^4/M^4 where M is the "typical hadronic mass scale." The $f_2(1270)$, being the nearest 2^{++} state, should set this scale. Substituting $M = 1270$ MeV and $q = 590$ MeV into q^4/M^4 gives 3°. Combining a good linear fit to spin-0 and a constant spin-2 provides a justification for modeling the relative phase shift as a linear function. A believer in this model would expect a fitted phase shift that resembles the solid line in figure 4.2 with a vertical negative offset arising from the constant spin-2 phase shift.

Specifically, a linear phase shift could be written as,

$$\Delta\delta(q) = a + bq \qquad \text{with parameters } a \text{ and } b. \tag{4.17}$$

But in anticipation of fitter optimization, it is better to write,

$$\Delta\delta(q) = a + bx \qquad \text{with} \qquad x = \frac{(q - 464\text{ MeV})}{124\text{ MeV}}, \tag{4.18}$$

where x defines a scale parameter that is -1 and 1 at the endpoints of the $\texttt{mass}(\pi\pi)$ range. Putting the pivot point at the center of the mass interval reduces correlation between the parameters a and b.

4.6.2 The $\mathcal{D}/\mathcal{S}$ Ratio in $\texttt{mass}(\pi\pi)$ Bins

The second option is to take $\texttt{mass}(\pi\pi)$ bins, which effectively converts q-dependent s- and d-waves,

$$\mathcal{M} = s(q)\mathcal{S} + d(q)\mathcal{D}, \tag{4.19}$$

into q-independent s- and d-waves in the i^{th} bin,

$$\mathcal{M}_i = s_i\mathcal{S} + d_i\mathcal{D} \qquad \text{or} \qquad \mathcal{M}_i \propto (\mathcal{S} + r_i\mathcal{D}) \text{ where } r_i = \frac{d_i}{s_i}. \tag{4.20}$$

Turning on phase shifts converts

$$r_i = \frac{d_i}{s_i} \quad \Longrightarrow \quad \frac{d_i e^{i\delta^{I=0}_{J=2}(q)}}{s_i e^{i\delta^{I=0}_{J=0}(q)}} \quad \Longrightarrow \quad \frac{d_i}{s_i} e^{i\delta^{I=0}_{J=2}(q) - i\delta^{I=0}_{J=0}(q)} \quad \Longrightarrow \quad r_i e^{-i\Delta\delta_i}. \tag{4.21}$$

In other words, a fit for the complex number $a_i + b_i i$ in

$$\mathcal{M}_i \propto (\mathcal{S} + (a_i + b_i i)\mathcal{D}) \tag{4.22}$$

would yield the d-wave to s-wave amplitude ratio, whose phase, $\tan^{-1}(b/a)$, is the isoscalar phase difference, $\Delta\delta(q_i)$.

But in order for this procedure to work, we need to choose $\mathcal{S}$ and $\mathcal{D}$. Recall how there are 2 s-waves and 5 d-waves (see Table 4.2). The simplest option, which we choose, is to assume,

$$\begin{aligned} \mathcal{S} &= \epsilon' \cdot \epsilon \\ \mathcal{D} &= d^2_{00}(\cos\theta_{\texttt{helicity}}) \;\; \epsilon' \cdot \epsilon. \end{aligned} \tag{4.23}$$

These are the same s-wave and d-wave terms that are present in the Kappa Model (see the appendix on page 106 for a discussion of $l^{\mu\nu}P'_\mu P'_\nu$ vs $d^2_{00}(\cos\theta_{\texttt{helicity}})$). But when we fit for,

$$\mathcal{M}_i \propto \left(\epsilon' \cdot \epsilon + (a_i + b_i i) d^2_{00}(\cos\theta_{\texttt{helicity}})\epsilon' \cdot \epsilon\right), \tag{4.24}$$

the binning effectively allows for a non-Kappa-Model q-dependence.

Unfortunately, when performing systematic studies, we discover that we cannot distinguish between a zero and a non-zero phase. We simply do not have enough events in mass($\pi\pi$) bins. Turning the lack of statistics around, we conclude that the FSI phase is not important in the description of our Data . Nevertheless, we can reliably extract the magnitude of the $\mathcal{D}/\mathcal{S}$ amplitude ratio.

4.7 QMI Model

At this point, having exhausted most of the literature, still without a satisfactory description of our Data , we turn to a quasi model-independent parameterization (QMI). The "quasi model-independent" criteria is guided by two ideas. The first is how the $\mathcal{D}/\mathcal{S}$ ratio in mass($\pi\pi$) bins is not sensitive to FSI. We turn this into an assumption and ignore FSI. The second idea is how the Voloshin Model does not improve fit quality. Since the Voloshin Model adds $\Delta m_{\texttt{spin}} \neq 0$ transitions, it is reasonable to assume $\Delta m_{\texttt{spin}} = 0$.

Assuming $\Delta m_{\texttt{spin}} = 0$ and that there are is no FSI phase shift, the most general amplitude is,

$$\mathcal{M} = \mathcal{S}(q)\epsilon' \cdot \epsilon + \mathcal{D}(q) d^2_{00}(\cos\theta)\epsilon' \cdot \epsilon, \tag{4.25}$$

where $\mathcal{S}(q)$ and $\mathcal{D}(q)$ are one parameter functions of mass($\pi\pi$). The dynamical assumption that angular momentum costs energy requires that $\mathcal{D}(q)$ be zero at the minimum and

maximum dipion mass (see appendix on page 106). One could enforce this requirement by replacing $d^2_{00}(\cos\theta)$ with $P'_\mu P'_\nu l^{\mu\nu}$. We choose instead to use $d^2_{00}(\cos\theta)$ and check that the fitted $\mathcal{D}(q)$ goes to zero at the endpoints.

We use the unitless scale parameter, $x = x(q) = (q - 464\text{ MeV})/(124\text{ MeV})$, that ranges from -1.0 to 1.0 across the dipion mass range, and write $\mathcal{S}(x)$ and $\mathcal{D}(x)$ as polynomials,

$$\mathcal{S}(x) = 0.5 + s_1 x + s_2 x^2 + s_3 x^3 + s_4 x^4 \tag{4.26}$$

$$\mathcal{D}(x) = d_0 + d_1 x + d_2 x^2 \tag{4.27}$$

The parameterization succeeds in significantly improving fit quality. When performing χ^2 tests, this parameterization is the only null hypothesis that cannot be rejected.

CHAPTER 5

EVENT SELECTION

Event selection starts by asking for high-quality tracks. These tracks have a successful Kalmin fit, $\chi^2/d.o.f. < 50$, hit fraction greater than 0.5, distance of closest approach to beamspot $<$ 2cm in $r-\phi$ and $<$ 10cm in z, $|\cos\theta| < 0.93$, track-momentum to beam-energy ratio between 0.01 and 1.2, `err` $(\cot\theta) < 0.3$ and `err`$(z_0) < 0.5$. Two-track events are kept as $\psi(2S) \to \pi^0\pi^0 J/\psi$ candidates and four-track events are kept as $\psi(2S) \to \pi^+\pi^- J/\psi$ candidates.

5.1 Lepton ID

For both $\pi^0\pi^0$ and $\pi^+\pi^-$ candidate events, the two highest-momentum tracks are called leptons and must be oppositely charged. Each lepton has a ratio of matched energy (E) to momentum (p). If the larger of the two E/p ratios is greater than 0.6 we assume the leptons are electrons, otherwise we assume the leptons are muons. After track and E/p

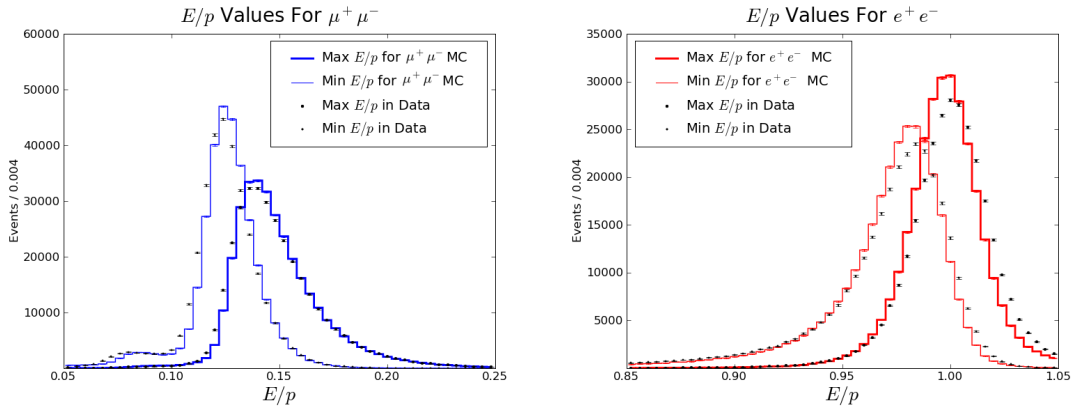

Figure 5.1: `Min` and `Max` E/p values for muon and electron pairs in `Generic MC` and our `Data` . The `max`$(E/p) > 0.85$ & `min`$(E/p) > 0.5$ electron cuts and `max`$(E/p) < 0.5$ & `min`$(E/p) < 0.25$ muon cuts are extremely loose. The muon plot (on the left) has the `min`$(E/p) < 0.25$ cut at the right-hand edge of the plot. The electron plot (on the right) has the `max`$(E/p) > 0.85$ cut at the left-hand edge of the plot.

cuts, each candidate event falls into one of four channels, which we write as $\pi^+\pi^-(\mu^+\mu^-)$, $\pi^+\pi^-(e^+e^-)$, $\pi^0\pi^0(\mu^+\mu^-)$, and $\pi^0\pi^0(e^+e^-)$.

The E/p cut is non-standard and requires some explanation. A common high-energy electron-id requirement (see for example [13]) is $E/p > 0.85$ for one electron and $E/p > 0.5$ for a second electron. Likewise, a value of $E/p < 0.25$ and $E/p < 0.5$ typically tags the first and second muon respectively. According to `Generic MC` as depicted in Figure 5.1, these cuts appear to be *extremely* loose.

Nevertheless, these E/p cuts behave badly in the region between barrel and endcap. The problem is due to missing half-crystals in the `Geant` description. A cross-section of the calorimeter, generated from the detector database, is on page 34 (figure 5.4). In the real detector, these half-crystals sit on top of the endcap, and are in the range $0.83 < |\cos\theta| < 0.84$. Because these crystals are only *half*-crystals and somewhat oddly shaped,[1] the matched energy (E) in our `Data` is reduced. But in `MC`, where there are no half-crystals, the matched energy (E) is significantly reduced. Figure 5.2 plots the E/p distributions in our `Data` and `MC` when at least one of the leptons has $0.83 < |\cos\theta| < 0.84$. The disagreement for muons is of no consequence because the E/p cuts are sufficiently far away. For electrons, the $\texttt{min}(E/p) > 0.5$ cut removes more `MC` and than our `Data` . The $\texttt{max}(E/p) > 0.85$ cut is less affected because typically only one of the leptons has $0.83 < |\cos\theta| < 0.84$.

Figure 5.3 shows the $\cos\theta$ distributions for both $\pi^+\pi^-(e^+e^-)$ and $\pi^0\pi^0(e^+e^-)$ at two levels of binning. The poorly modeled $\texttt{min}(E/p) > 0.5$ cut results in a `MC` dip but no visible problem in electron data. Putting it a different way, *if you were only to look at our* `Data` *you would not see the crack in the detector!* Faced with these issues, we changed strategies on lepton-id. We now merely compare $\texttt{max}(E/p)$ with 0.6 to

[1] which is exactly why they were not included in the `Geant` description.

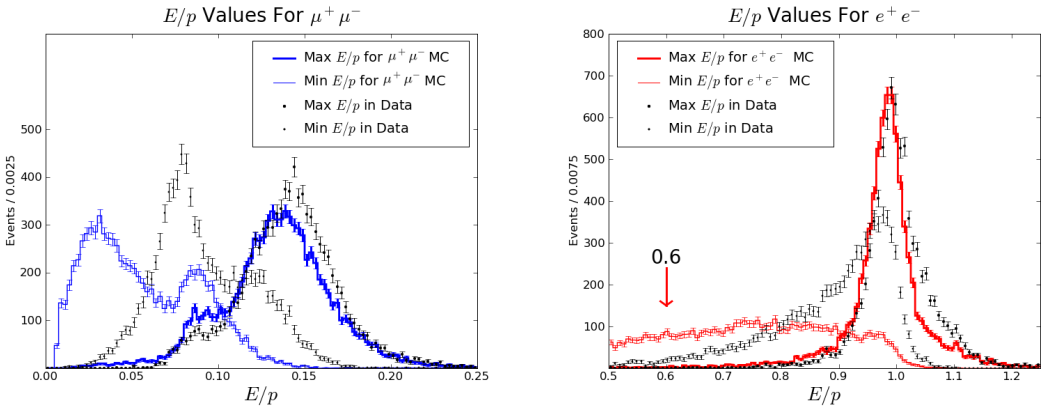

Figure 5.2: A repeat of figure 5.1 with the additional requirement that at least one lepton has $0.83 < |\cos\theta| < 0.84$. Both our `Data` and `Generic MC` shift to lower values because there are fewer crystals between the barrel and endcap. However, the `MC` drops further because of missing half-crystals in the `Geant` description.

differentiate electron from muon pairs. This cut is labeled in figure 5.2. And because of kinematic fitting (described below), the weakening of our lepton-id does not increase background rates.

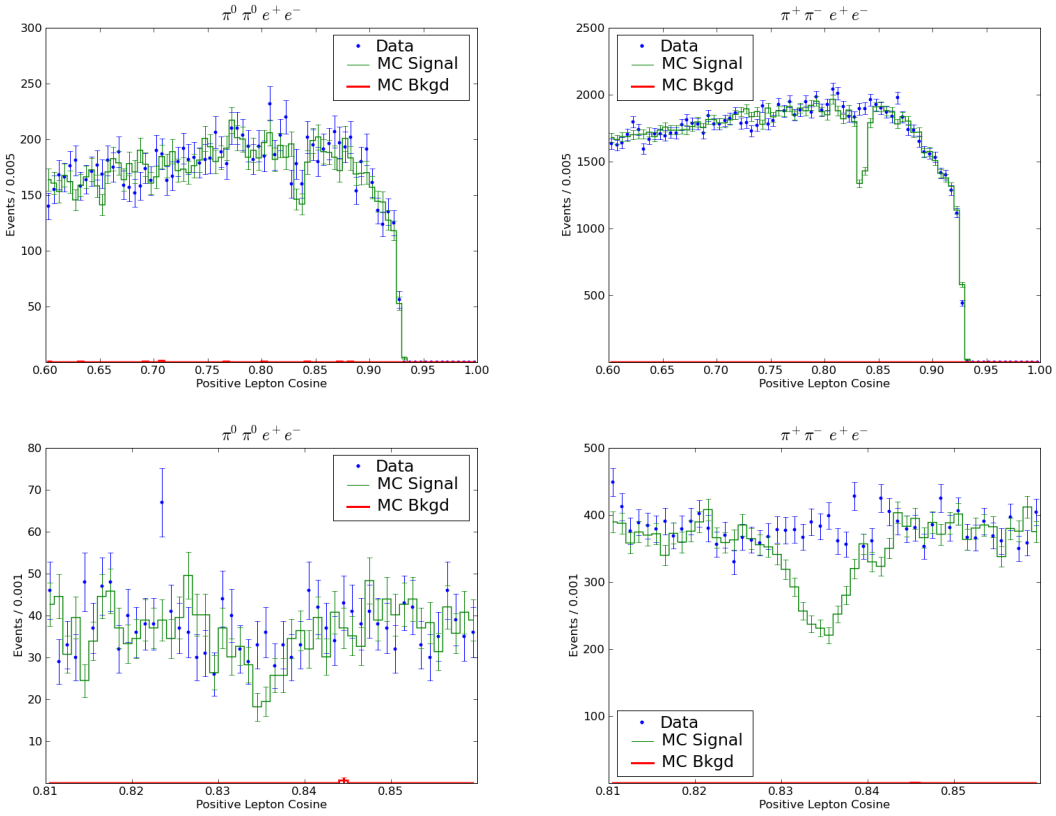

Figure 5.3: $\cos\theta$ for the positron in $\pi^+\pi^-(e^+e^-)$ (first column) and $\pi^0\pi^0(e^+e^-)$ (second column). The second row zooms in to the $0.83 < |\cos\theta| < 0.84$ region. The `Generic MC` dip is eliminated when switching to a $\texttt{max}(E/p) \sim 0.6$ cut. The minimal background ($\ll 1\%$) is visible in the lower left plot between 0.84 and 0.85.

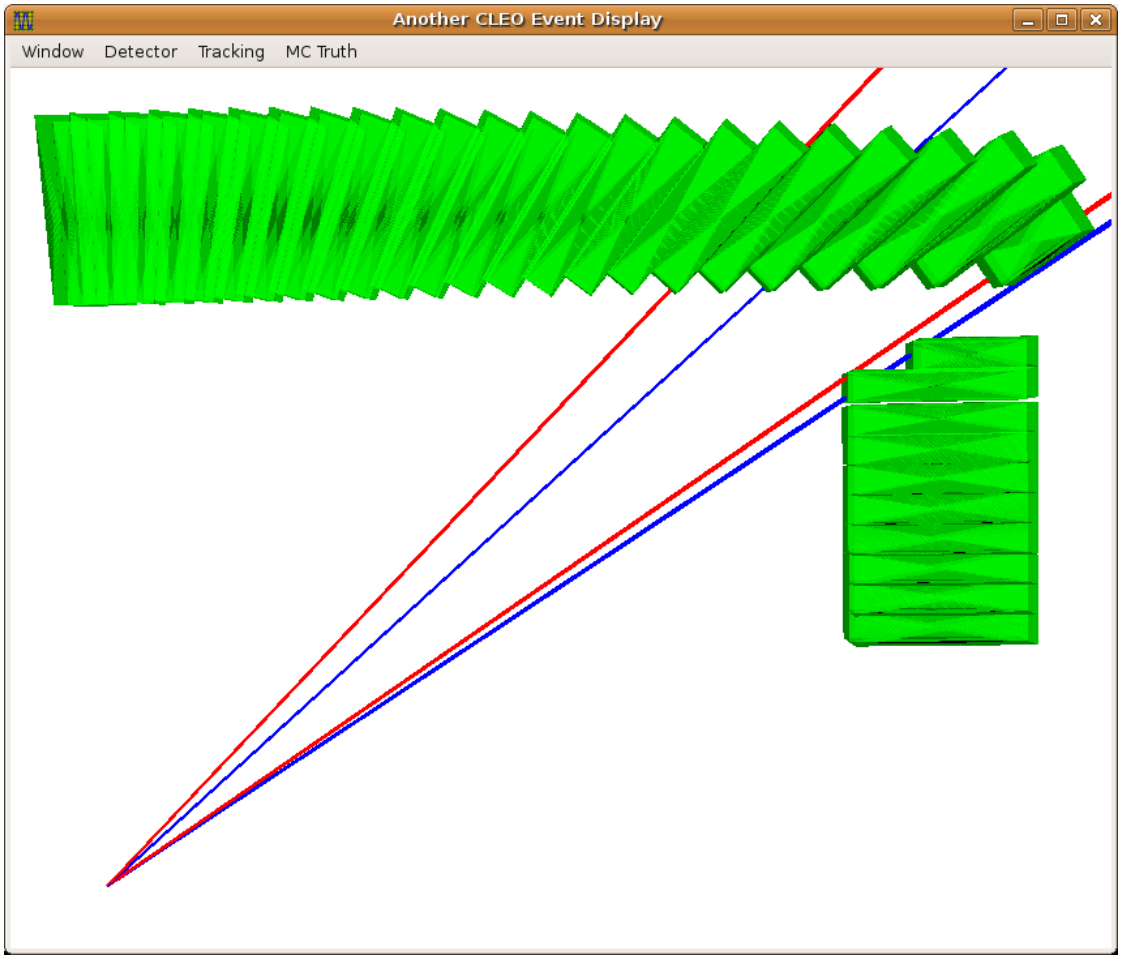

Figure 5.4: A crosssection of the calorimeter, generated from the detector database. The lines from the lower-left to upper-right denote $\cos\theta = 0.70$, $\cos\theta = 0.75$ (important for π^0 shower systematics) and $\cos\theta = 0.83$, $\cos\theta = 0.85$ (important for lepton id).

5.2 Pion Selection

For $\pi^+\pi^-$ candidate events, the two remaining (low-momentum) tracks, must be oppositely charged and are called charged pions.

For $\pi^0\pi^0$ candidate events, we start with the set of good showers. These showers are not matched to a track, are not associated with hot crystals, have $0.01 < E/E_{\text{beam}} < 1.2$, have $E_\gamma > 30$ MeV and are either "good barrel" ($|\cos\theta| < 0.81$) or "good endcap" ($0.85 < |\cos\theta| < 0.93$). And in order to avoid radiation from $J/\psi \to e^+e^-$, we ignore showers that are aligned within 100 mrad of a track. Signal events are expected to have four showers; we skip events with seven or more showers.

We use `PhotonDecaysProd` to form π^0 candidates. Given the combinatorics, there at least six π^0 candidates in signal events. For each $\pi^0\pi^0$ pair, we apply a `4C` fit (the details of which are discussed in section 5.5). We choose the $\pi^0\pi^0$ pair with the smallest $\chi^2_{\texttt{fit}}/d.o.f.$ in the `4C` fit.

5.3 The `LabNet4Momentum` and $\pi\pi$ Recoil Mass

The $\pi\pi$ recoil mass is defined in the following way. Conservation of four-momentum requires,

$$p^\mu_{\psi(2S)} = p^\mu_{\pi\pi} + p^\mu_{J/\psi}, \tag{5.1}$$

which implies,

$$m_{J/\psi} = \sqrt{\left(p_{\psi(2S)} - p_{\pi\pi}\right)^2}. \tag{5.2}$$

The right hand side of eq. 5.2 is by definition the $\pi\pi$ recoil mass. We require this recoil mass to be within 20 MeV of the J/ψ mass.

But when we began comparing `MC` with our `Data`, we noticed something strange. The `MC` recoil mass peaked, as expected, at mass(J/ψ) $\approx$ 3097 MeV. But the recoil mass in our `Data` peaked at 3099 MeV, about 2 MeV above the J/ψ mass. Our calculation took the pion four-momenta the standard reconstruction software and the $\psi(2S)$ four-momentum from the `LabNet4Momentum`. The `LabNet4Momentum` internally computes a four-momentum from the known crossing angle and beam energy, *not from the* $\psi(2S)$ *mass*. The code is equivalent to,

$$\text{LabNet4Momentum} = \begin{cases} t = 2E_{\text{beam}} \cos\theta \\ x = -2E_{\text{beam}} \sin\theta \\ y = 0 \\ z = 0 \end{cases} . \tag{5.3}$$

Our 2 MeV difference arose because the *average* center of mass energy in e^+e^- crossings in our `Data` is slightly above the $\psi(2S)$ mass. Part of the issue here is that the width of the $\psi(2S)$ (about 0.4 MeV) is significantly smaller than the beam energy spread (a few MeV). Physically, the $\psi(2S)$ preferentially gets created when the beam energy fluctuates downward (or there is initial state radiation). The end result is that the `LabNet4Momentum` returns a four-momentum that is not the four-momentum of the $\psi(2S)$. This problem does not occur in `Generic MC` because the beam energy is explicitly set to give the correct $\psi(2S)$ mass.

In order to reconcile the situation, we rescale the components of the LabNet4Momentum according to,

$$P^{\mu}_{LabNet4Momentum} \rightarrow P^{\mu}_{\psi(2S)} = \frac{P^{\mu}_{LabNet4Momentum}}{\sqrt{(P_{LabNet4Momentum})^2}} \times m_{\psi(2S)}. \tag{5.4}$$

In our Data , this effectively alters the beam energy without changing the crossing angle. In MC, the scaling does not make much of a difference. The change shifts the $\pi\pi$ recoil mass spectrum in our Data down by 2 MeV giving much better agreement with MC. The scaling also improves kinematic fitting as the corrected LabNet4Momentum is used to when performing 4C-fits.

In summary, we rescale the LabNet4Momentum and cut on the $\pi\pi$ recoil mass,

$$m_{J/\psi} - 20\text{MeV} < \sqrt{(p_{\psi(2S)} - p_{\pi\pi})^2} < m_{J/\psi} + 20\text{MeV}. \tag{5.5}$$

5.4 Photon Conversion

Figure 5.5 plots mass($\pi\pi$) for $\pi^+\pi^-(e^+e^-)$ and $\pi^+\pi^-(\mu^+\mu^-)$ events in our Data . Kinematic fitting, which is described in the next section, has been applied and successfully removed almost all backgrounds. The one remaining background is visible in the lower left-hand corner (below 300 MeV) where the plots begin to rise as the mass goes down to 280 MeV.

The background is primarily radiative Bhabha events where the photon converts. The photon in $e^+e^- \rightarrow \gamma e^+e^-$, when hitting the beam pipe, pair produces making the event look like $e^+e^- \rightarrow (e^+e^-)e^+e^-$. The two high-momentum leptons, the two not from

photon conversion, occasionally 1C fit to the J/ψ mass. If this happens, event selection will think the other two tracks (from $\gamma \to e^+e^-$) are charged pions.

Kinematically, these fake events are characterized by two properties. The first is the dipion mass. The virtual photon that converts has a small but nonzero mass. When the electron and positron are misidentified as charged pions, their invariant mass gets raised from slightly above zero to slightly above twice the charged pion mass. This explains why the background peaks near 280MeV in figure 5.5. The second property is the preferential alignment of the photon in $e^+e^- \to \gamma e^+e^-$ with one of the two leptons. In other words, a fake dipion will almost always have minimum mass and be aligned with one of the leptons.

After a continuum study using our `continuum Data` we decided to cut out the `mass`($\pi\pi$) region below 340MeV. We did not find it necessary to cut on the alignment of the dipion with the leptons. Figure 5.5 shows the open question before the continuum

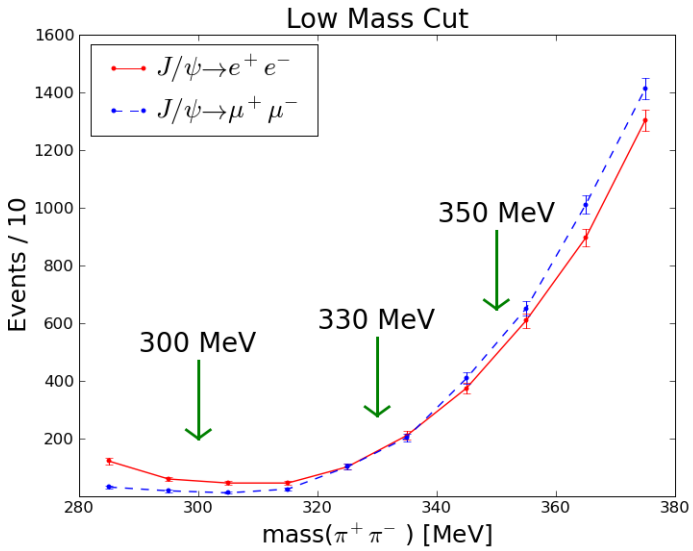

Figure 5.5: The $\pi\pi$ mass for $\pi^+\pi^-(e^+e^-)$ and $\pi^+\pi^-(\mu^+\mu^-)$. The background from radiative Bhabhas and μ-pairs is visible below 300 MeV. Before a continuum study we were not sure where to cut. Possibilities are indicated at 300 MeV, 330MeV, and 350MeV. We eventually settled on 340MeV.

study. Although we could see the radiative Bhabha contamination below 300MeV, we were worried about a tail going out to higher mass, and as such, were unsure about precisely where to cut.

Our continuum study applies event selection to our `continuum Data`, which has a beam energy at 1836 MeV instead of the on-resonance 1844 MeV data.[2] Given that we are looking for $e^+e^- \to \gamma\ell^+\ell^-$ off resonance, we do not scale the `LabNet4Momentum`. We also need to adjust the `1C` fit mass because the fake rate depends on the $E_{\texttt{1C mass}}/E_{\texttt{cm}}$ ratio. For simplicity, we do five fits per event, one with the true J/ψ mass, two with ± 10 MeV and two with ± 20 MeV. The "modified J/ψ mass" affects the `1C` fit and the center of the $\pi\pi$ recoil mass window. Figure 5.6 shows the `mass`$(\pi\pi)$ distributions for these five fits. The continuum yields are scaled[3] up to match the luminosity in our `Data`

.

Figure 5.6 reveals how radiative μ-pairs with conversion (on the left) occur at a negligible rate. The radiative Bhabha events with conversion (on the right) happen much

[2] It turns out the "off-resonance" data was close enough to the resonance peak to produce a small but non-negligible number $\psi(2S)$'s (for details see [13]).

[3] There is also a $1/s$ correction that we have neglected. We have only attempted to do an order of magnitude estimate in this study. Again, for a more detailed description see [13].

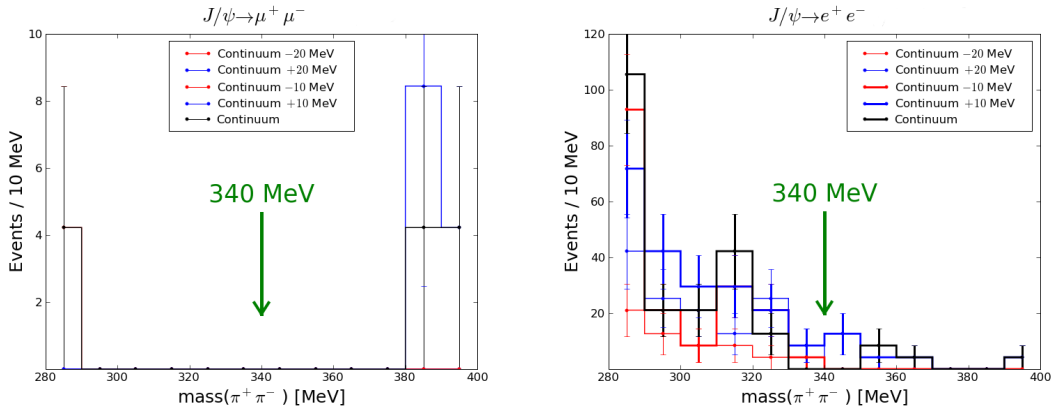

Figure 5.6: `mass`$(\pi\pi)$ scaled yields from event selection applied to our `continuum Data`.

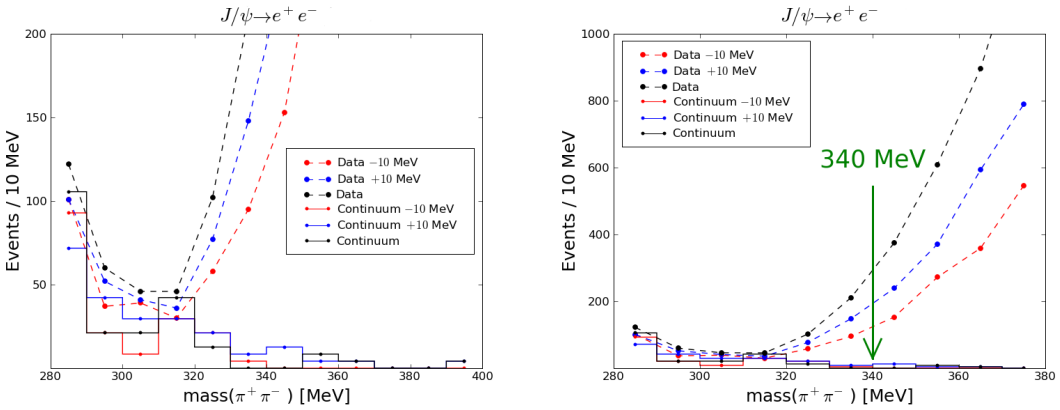

Figure 5.7: mass($\pi\pi$) distributions for our continuum Data and our Data . The Continuum data have been scaled to match on-resonance data. The cut at 340 MeV is visible on the right.

more regularly. In order to compare this background with our Data , Figure 5.7 plots scaled our continuum Data and our Data at two levels of binning. The figure contains the standard data and continuum 1C fit masses as well as ±10MeV. Our cut at 340 MeV is visible on the right. Figure 5.6 also demonstrates how above 340 MeV, the yields are very dependent on the numerical value chosen for the J/ψ.

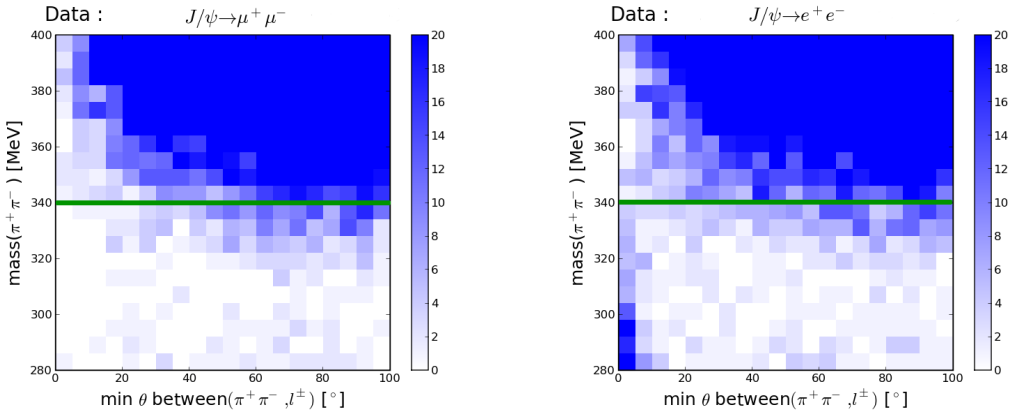

Figure 5.8: mass($\pi^+\pi^-$) versus alignment angle for $\pi^+\pi^-\mu^+\mu^-$ and $\pi^+\pi^-e^+e^-$ in our Data . The 340 MeV cut is denoted by the horizontal green lines.

Figure 5.8 adds the alignment angle and plots in two dimensions the $\pi^+\pi^-(\mu^+\mu^-)$ and $\pi^+\pi^-(e^+e^-)$ channels. The vertical axes is the low end of the dipion mass. The horizontal axis is the minimum angle between the dipion and one of the leptons. For $\pi^+\pi^-(e^+e^-)$,

the background below 340 MeV is concentrated where $\theta < 5^\circ$, consistent with radiative Bhabha events

Although it is encouraging to see the radiative Bhabha "spot" in figure 5.8 (on the right), the two plots indicate the presence of other backgrounds. There are events with minimum dipion mass with large alignment angle in *both* $\pi^+\pi^-(\mu^+\mu^+)$ and $\pi^-\pi^+(e^+e^-)$. These cannot be from $e^+e^+ \to \gamma\ell^+\ell^-$. One clue as to what is going on is in on the left in figure 5.7. This is a plot of $\pi^+\pi^-(e^+e^-)$. Notice how the "background" peak in data goes down when the J/ψ mass is moved by both +10 MeV and −10 MeV, which is suggestive that there really are J/ψ's in these events.

We speculate that the background is from $\psi(2S) \to \gamma(\chi_c, \eta_c') \to \gamma(\gamma J/\psi)$ where $J/\psi \to \ell^+\ell^-$ and of one of the photons converts. We ran full detector `MC` for $\psi(2S) \to \gamma\gamma J/\psi$; $J/\psi \to \mu^+\mu^-$ where the $\psi(2S) \to \gamma\gamma J/\psi$ decay is phase space. For `MC` events with a photon conversion in the `MC-Truth` table, we apply event selection and plot the result against $\pi^+\pi^-(\mu^+\mu^-)$ in figure 5.9. The normalization is manually changed to line up with our `Data` . Figure 5.9 confirms the shape of $\psi(2S) \to \gamma\gamma J/\psi$ looks correct. The fall off in our `Data` with ±10 MeV `1C` fit masses below 300 MeV also adds evidence that real J/ψ's are in these events.

Figure 5.10 shows the two dimensional plots (dipion mass versus alignment angle) for continuum and $\psi(2S) \to \gamma\gamma J/\psi$ `MC`. The three continuum plots are for $\pi^+\pi^-(e^+e^-)$, are in the upper left, lower left, and lower right, and show the characteristic radiative Bhabha "spot" in the lower left-hand corners of the plots. Meanwhile, the `MC` plot (upper right) has dipion masses below 340 MeV characteristic of photon conversions. But it does not have small alignment angles making it inconsistent with $e^+e^- \to \gamma\mu^+\mu^-$, which, of course, it is not.

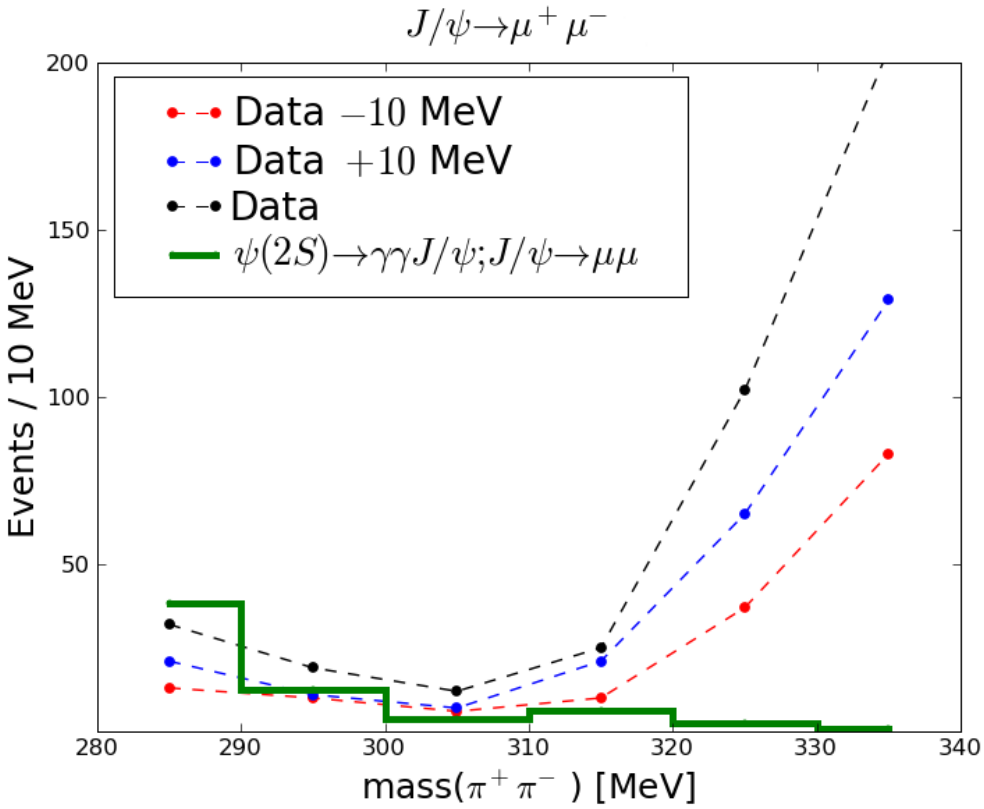

Figure 5.9: `mass`($\pi^+\pi^-$) for $\pi^+\pi^-(\mu^+\mu^-)$ and full detector simulation of $\psi(2S) \to \gamma\gamma J/\psi$; $J/\psi \to \mu^+\mu^-$. The normalization of the `MC` was manually set to agree with our `Data` .

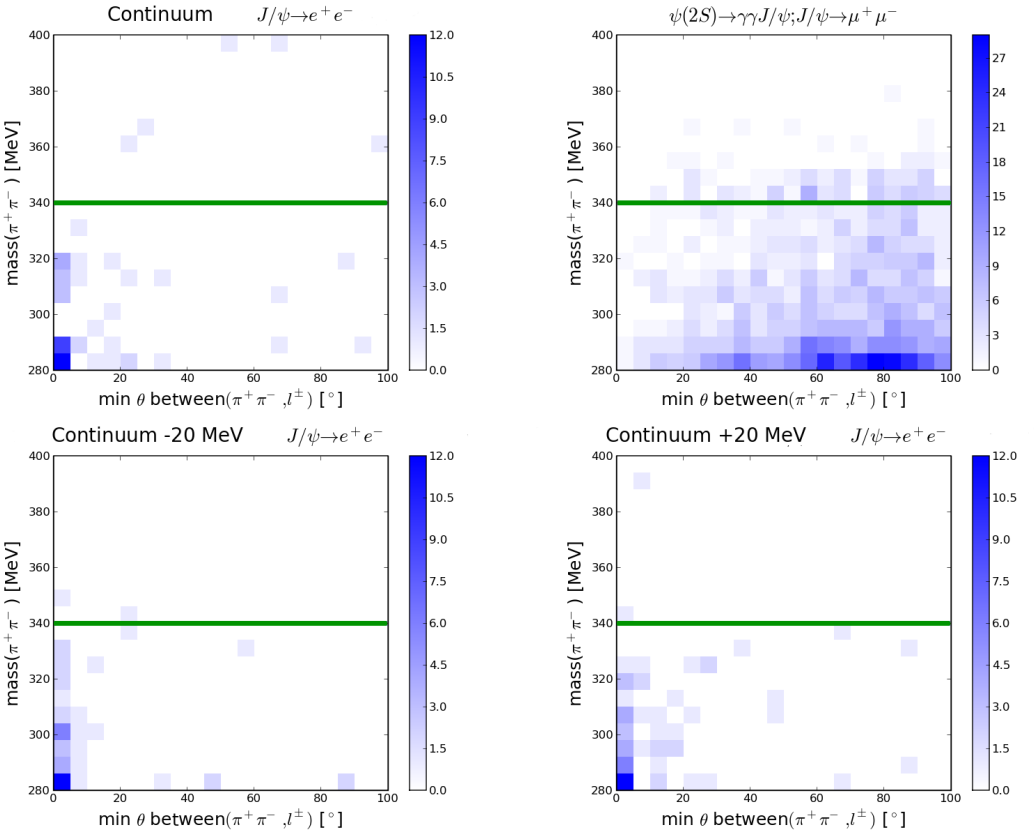

Figure 5.10: mass($\pi^+\pi^-$) versus alignment angle for $\pi^+\pi^-e^+e^-$ Continuum and full detector simulation of $\psi(2S) \to \gamma\gamma J/\psi$; $J/\psi \to \mu^+\mu^-$. The 340 MeV cut is denoted by the horizontallines.

5.5 Kinematic Fitting

We use kinematic fitting to both reduce background and minimize resolution smearing. Roughly speaking, the leptons are 1C fit to the J/ψ mass and then the entire event is 4C fit to the LabNet4Momentum.

We actually try to do these two fits twice, one without and one with Brehmsstrahlung recovery. Predominately for electrons but occasionally for muons, the $J/\psi \to \ell^+\ell^-$ decay may emit photons in the form of final state radiation. And after the decay, when these leptons are traversing the inner detector, they may emit further photons through Brehmsstrahlung. Recovering both types of photons is essential for getting accurate momentum and polarization fourvectors for the J/ψ.

When performing kinematic fitting we use FitEvt. In the 4C fits, we use the scaled[4] version of the LabNet4Momentum.

- FitWithoutBrem (No Bremsstrahlung Recovery): First, the two leptons are 1C fit to the J/ψ mass. Second, the fitted fourvector the J/ψ and two pion tracks are 4C fit to the LabNet4Momentum. If the pions are neutral they are placed at the J/ψ vertex (with inflated errors). Notice how there are four fits: two vertex fits, a mass fit and a 4C fit.
- FitWithBrem (With Bremsstrahlung Recovery): If there are any bremShowers associated with at least one of the leptons then we do the following. First, a vertex fit combines the two leptons. If the pions are charged, then they are included in this vertex fix. Next, the leptons and bremShowers are 1C fit to the J/ψ mass. During this fit, the showers are added at the vertex of the previous fit (with inflated errors). And finally, a 4C fit combines the two pion tracks with the fitted

[4] see section 5.3

J/ψ fourvector. Again, if the pions are neutral, the pions are placed at the J/ψ vertex (with inflated errors). Notice how there are five fits: three vertex fits, a mass fit, and a `4C` fit.

If no `bremShowers` are present then only `FitWithoutBrem` is made. Otherwise, both `FitWithoutBrem` and `FitWithBrem` are performed. Logistically, we do not cut on the $\chi^2/d.o.f.$ values during the first skim. So in principle, an event with `bremShowers` should have both `FitWithoutBrem` and `FitWithBrem` unless of course one of the kinematic fits fails without producing a χ^2.

We define `MaxChi2` as the maximum $\chi^2/d.o.f.$ for all fits in the event. For `FitWithoutBrem` and `FitWithBrem` this is the maximum of four and five values respectively. We keep the event (during a secondary skim) if at least one of the two `Fits` has `MaxChi2` less than 50. This is an extremely loose cut. The plots relevant to systematic studies are on page 77 (figure 7.3).

5.6 Yields in our Data

At this point event selection is done. As shown in the following table, our Data provides about 696,000 events with a background rate of less than 0.25%. This background, mainly from $J/\psi \rightarrow \pi^+\pi^-$, is discusssed in the next section. The background from continuum is negligible above 340 MeV.

Figure 5.11 and 5.12 show the mass($\pi\pi$) and $|\cos(\theta_{\text{helicity}})|$ distributions comparing our Data with Generic MC across the four channels. The $\pi^+\pi^-(\mu^+\mu^-)$ plots were already shown in the motivation section (figure 2.2 on page 9).

Table 5.1: The yields from our Data after event selection.

Channel	Events in our Data	MC Bkg	Bkg Events in our Data
$\pi^+\pi^-(\mu^+\mu^-)$	302,345	0.24%	≈726
$\pi^+\pi^-(e^+e^-)$	280,498	0.09%	≈254
$\pi^0\pi^0(\mu^+\mu^-)$	58,871	0.65%	≈ 382
$\pi^0\pi^0(e^+e^-)$	54,417	0.41%	≈ 223
$\pi^+\pi^-(l^+l^-)$	582,843	0.17%	≈978
$\pi^0\pi^0(l^+l^-)$	113,288	0.53%	≈ 606
$\pi\pi(l^+l^-)$	696,131	0.23%	≈ 1583

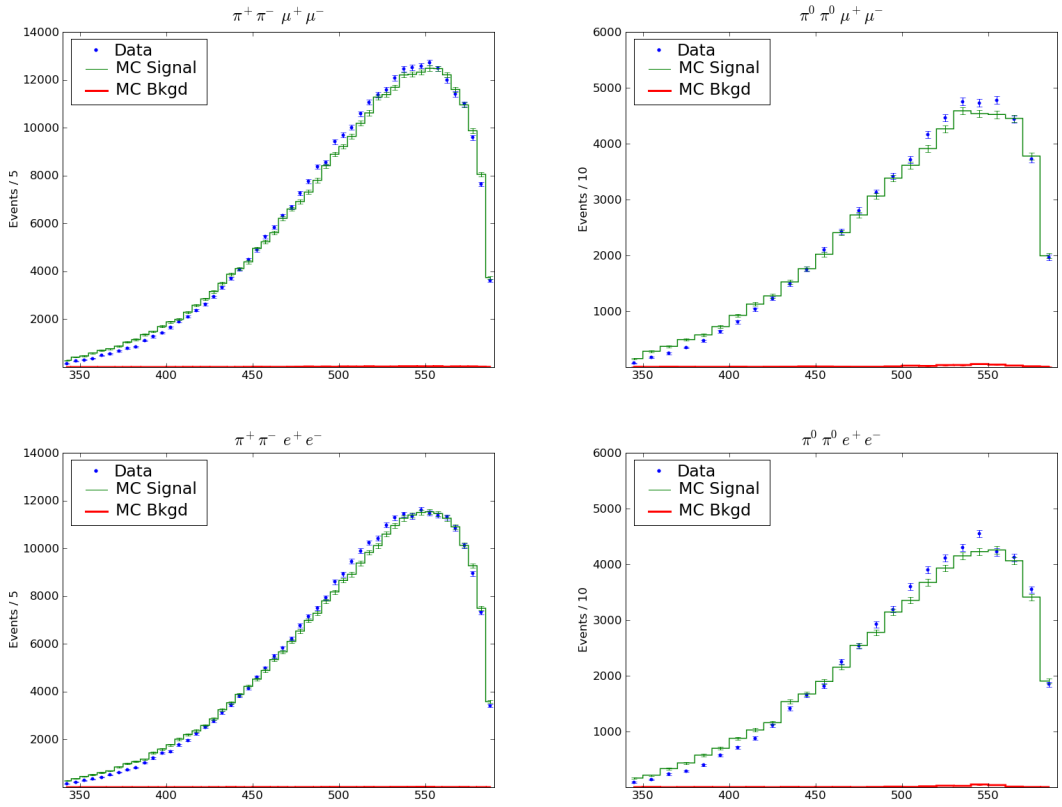

Figure 5.11: The `mass`($\pi\pi$) comparing `Generic MC` with our `Data`. The `Generic MC` decay model, `VVPIPI`, poorly models data (see table 8.6 and the discussion on page 99).

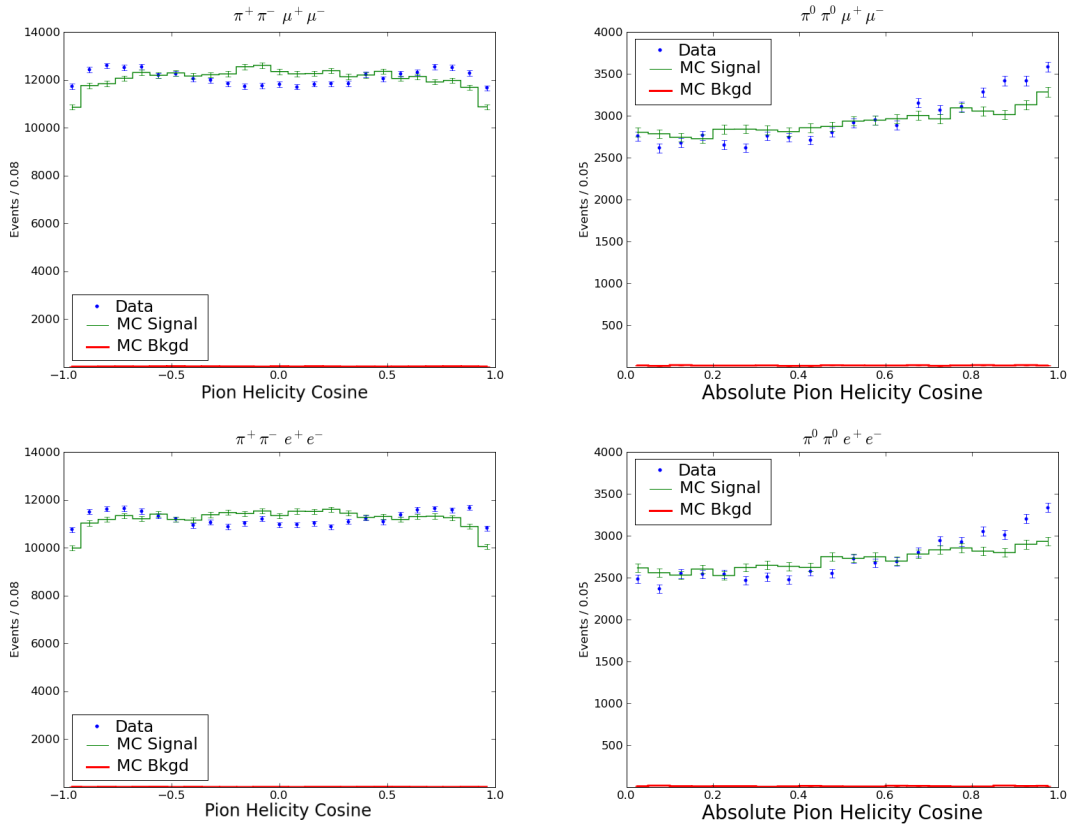

Figure 5.12: The (absolute) pion helicity cosine comparing `Generic MC` with our `Data`. The `Generic MC` decay model, `VVPIPI`, poorly models data (see table 8.6 and the discussion on page 99).

5.7 Backgrounds

The 0.23% background is mainly from $\psi(2S) \rightarrow \pi\pi J/\psi$ where $J/\psi \rightarrow \pi^+\pi^-$. The problem is that the pions from the J/ψ look like muons. There is also some background from $J/\psi \rightarrow K^+K^-$ and $J/\psi \rightarrow p\bar{p}$, but these heavier particles generally have $\chi^2/d.o.f$ values in the kinematic mass fit to the J/ψ that are above the cut at 50. Figure 5.13 shows the `MaxChi2`, defined as the maximum $\chi^2/d.o.f$ value in all kinematic fits in each event, for these backgrounds. The signal `MaxChi2` is indistinguishable from the $J/\psi \rightarrow \pi^+\pi^-$ background; the cut at 50 cannot remove the pion background. The thing that saves this analysis is the small branching fraction. For reference, EvtGen uses $\mathcal{B}(J/\psi \rightarrow \pi^+\pi^-) = 0.000147$ and $\mathcal{B}(J/\psi \rightarrow K^+K^-) = 0.000237$ which are less than one percent of $\mathcal{B}(J/\psi \rightarrow \mu^+\mu^-) = \mathcal{B}(J/\psi \rightarrow e^+e^-) = 0.05953$.

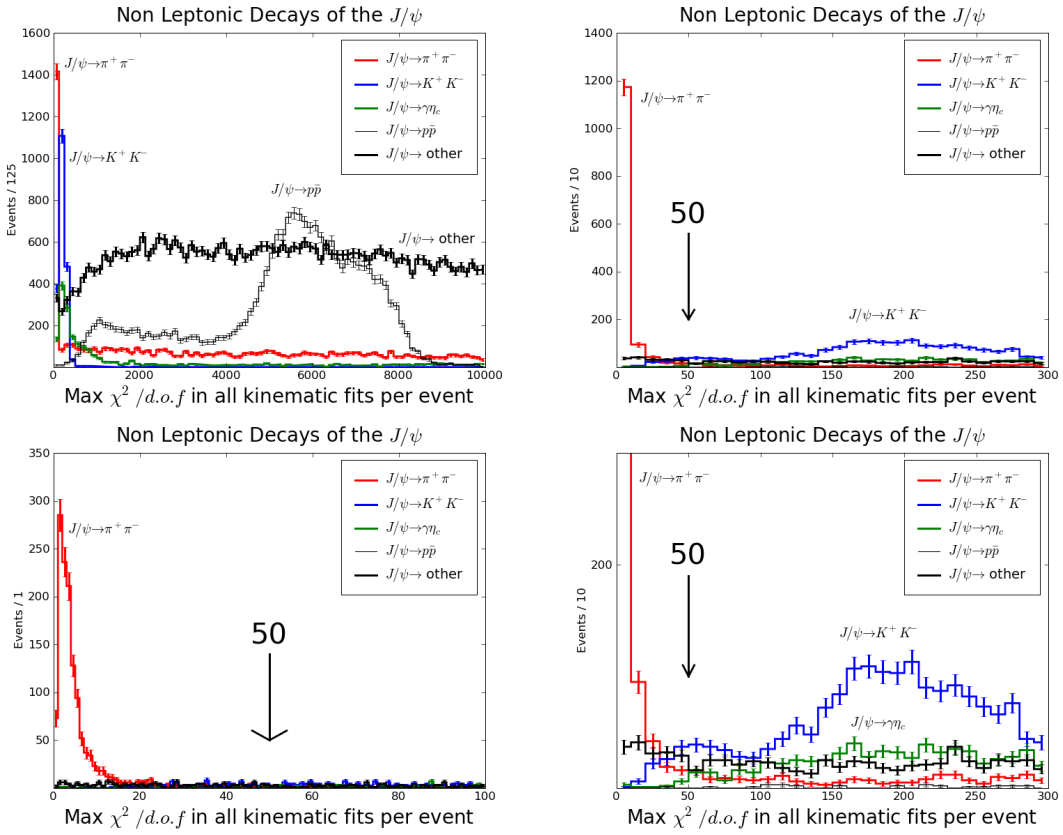

Figure 5.13: `MaxChi2`, defined as the maximum $\chi^2/d.o.f$ value in all kinematic fits in each event, for various backgrounds. The upper left plot highlights the $J/\psi \to p\bar{p}$ background. The lower left plot highlights the shape of the $J/\psi \to \pi^+\pi^-$ background. The plots on the right highlight (with different y-ranges) the background in the vicinity of the cut at 50.

5.8 Kinematic Preparation for Fitting

The purpose of event selection is to provide the likelihood fitter with a set of background-free events. The likelihood fitter, to be discussed in section 6, takes as input a set of five fourvectors. The set contains the `LabNet4Momentum`, the fourmomenta of the pions, and the fourmomenta of the leptons. It does not contain information of recovered showers.

At this point, event selection has produced events with either one or two `Fit`s with `MaxChi2` below 50. If there are two `Fit`s we choose the one with smaller `MaxChi2`. This procedure will be justified in a moment. We then extract the kinematically fitted pion and lepton fourvectors. Since the lepton `4C` fit can change the fourmomenta of the J/ψ, we use this adjusted J/ψ momenta to re-fit the fourvectors of the leptons.

When using `FitWithBrem`, we need to *reattach* the photons. The reason is that the fitter assumes the leptons have not radiated. For each lepton, we add to its back-propagated fourmomenta the back-propagated fourmomenta of any associated `bremShowers`. This effectively relabels the leptons, in the sense that,

$$J/\psi \to e^+ (\gamma e^-) \qquad \Longrightarrow \qquad J/\psi \to e^+ \ \text{“}e^-\text{”}, \tag{5.6}$$

where $p^\mu_{\text{“}e^-\text{”}} = p^\mu_{e^-} + p^\mu_\gamma$. The adjusted leptons are now inevitably (slightly) off-shell.

We now return to the decision to select the `Fit` with the smaller `MaxChi2`. Consider figure 5.14, which shows a scatter plot of the `MaxChi2` for $\pi^+\pi^-(e^+e^-)$ and $\pi^0\pi^0(e^+e^-)$ in `Generic MC`. These are events where both `FitWithoutBrem` and `FitWithBrem` have `MaxChi2` below 50. There three distinct regions. First, the straight line identifies events where the photon does not influence the `MaxChi2` (where both `MaxChi2` are nearly identical). Second, the vertical band on left-hand side of the plots reveal

a concentration of events where FitWithoutBrem has significantly lower MaxChi2 than FitWithBrem. The third region is the horizontal band, which is a concentration of events where FitWithBrem has significantly lower MaxChi2. The algorithm that chooses the lower MaxChi2 chooses randomly when in the first region and easily separates the second and third region.

But we have yet to verify that events with lower MaxChi2, defined above as the maximum $\chi^2/d.o.f$ in the event, actually represents a better fit. We introduce two angles, the first of which is the angle between the MC Truth J/ψ momentum and FitWithBrem J/ψ momentum. The second angle is the corresponding angle for FitWithoutBrem. We then histogram (in figure 5.15) the minimum of and difference between these two angles. This minimum angle peaks at 1° or 2° and indicates how at least one of the two Fits has the J/ψ within a few degrees of MC Truth. The difference between the two angles is a measure of how much worse the other Fit gets the direction the J/ψ. Below 5° we would expect to isolate the straight line in figure 5.14. The result is in figure 5.16 and is arguable only somewhat successful. On the other hand, when the difference is greater than 5°, the two bands are easily separated as can be seen in figure 5.17). These last set of plots are our justification for selecting the Fit with the smallest MaxChi2.

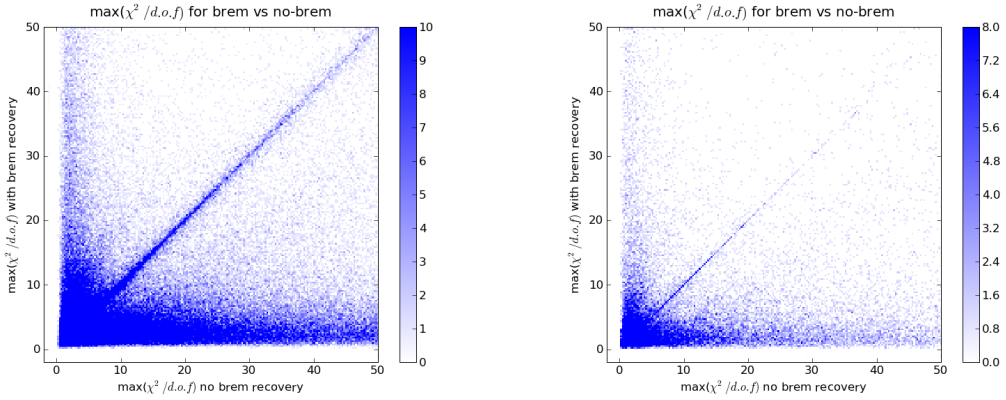

Figure 5.14: Kinematic Fit Qualities, FitWithBrem versus FitWithoutBrem, for Generic MC. On the left is $\pi^+\pi^-(e^+e^-)$ and on the right is $\pi^0\pi^(0e^+e^-)$.

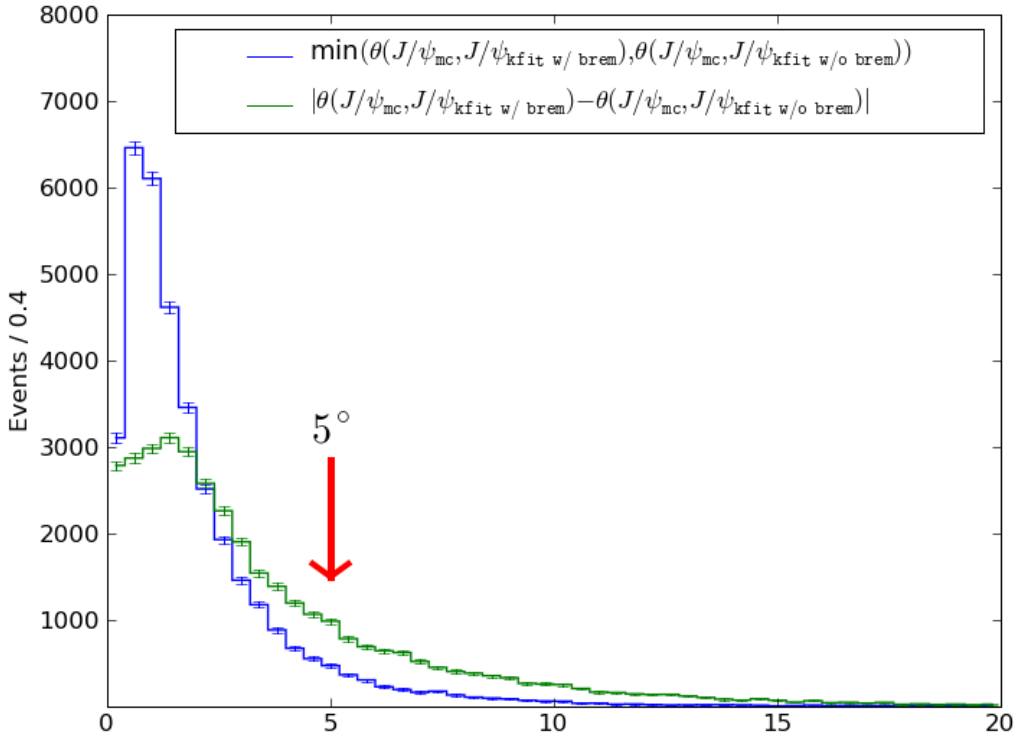

Figure 5.15: The minimum of and difference between the angle between the `MC Truth` J/ψ momentum and `FitWithoutBrem` J/ψ momentum or the `FitWithBrem` J/ψ.

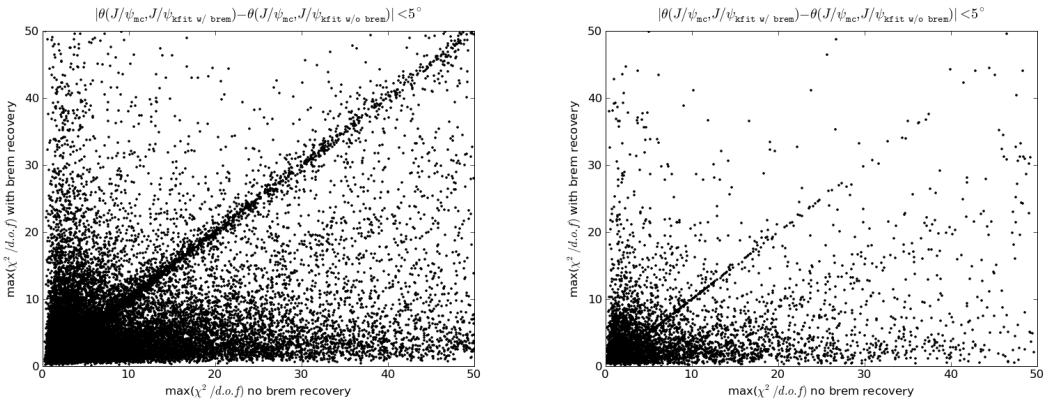

Figure 5.16: Same as figure 5.14 with the additional requirement that angular difference (see text) is less than 5°. On the left is $\pi^+\pi^-e^+e^-$ and on the right is $\pi^0\pi^0e^+e^-$.

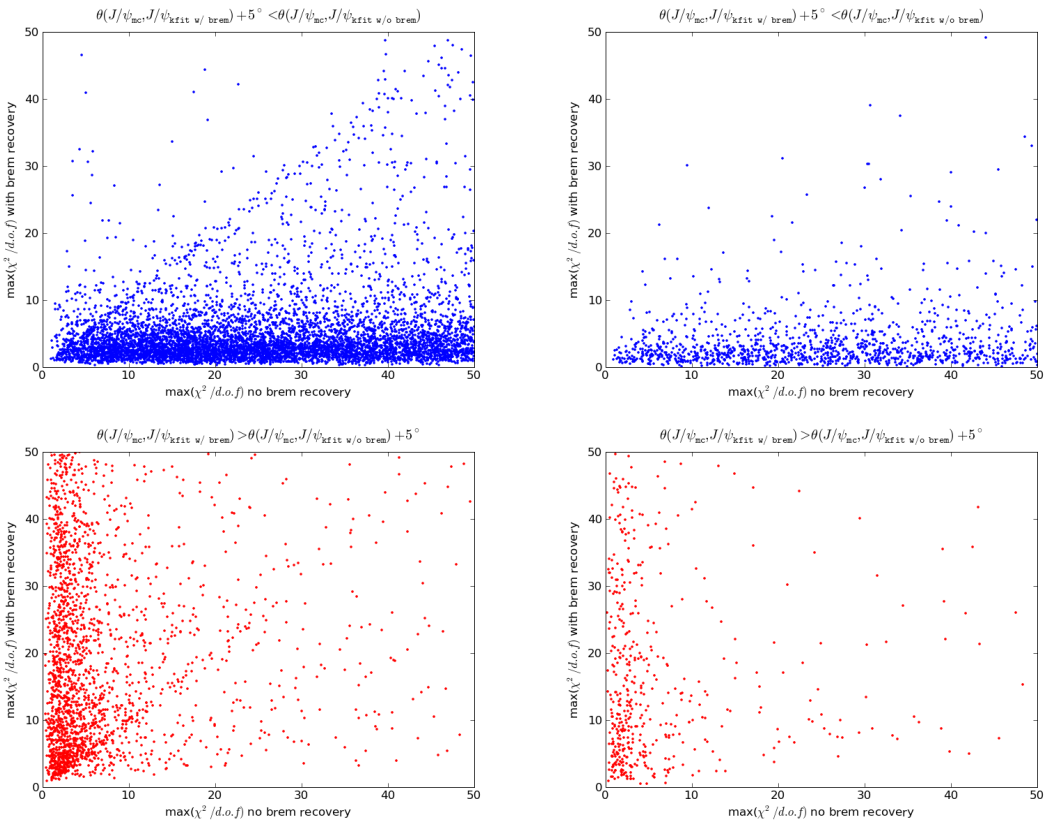

Figure 5.17: Same as figure 5.14 with the additional requirement that angular difference (see text) is greater than 5°. The first row is when `FitWithBrem` is better, in the sense that the fitted J/ψ 3-momentum has a closer alignment with the MC-Truth momentum. The Second row is when `FitWithoutBrem` is better. The first column is $\pi^+\pi^-(e^+e^-)$ and the second column is $\pi^0\pi^0(e^+e^-)$.

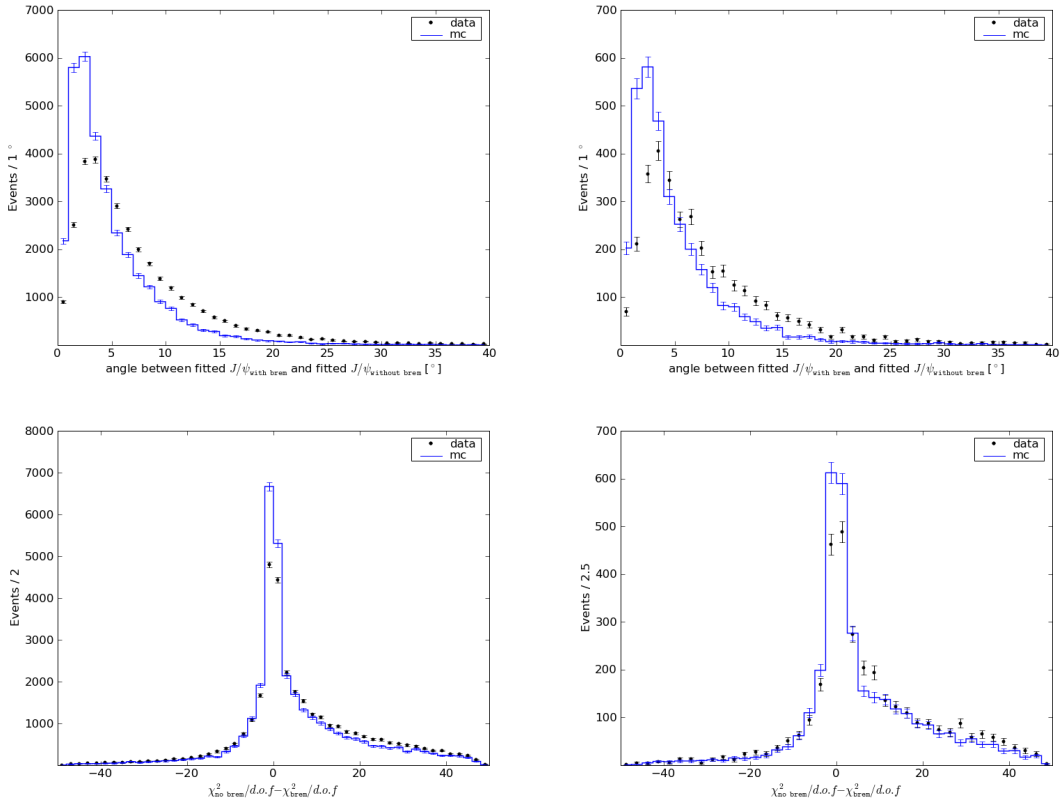

Figure 5.18: A comparison between our `Data` and `Generic MC`. The first row is the angle between the `FitWithBrem` and `FitWithoutBrem` J/ψ momentum. The second row is the difference between the kinematic fit qualities (`FitWithoutBrem` minus `FitWithBrem`). The first column is $\pi^+\pi^-e^+e^-$ and the second column is $\pi^0\pi^0e^+e^-$. The bottom row is far more important as we decide whether we keep `FitWithBrem` or `FitWithoutBrem` depending on the sign of the entries in the histograms.

And last but not least, we investigate the agreement between our Data and Generic MC. The top row in figure 5.18 histograms the angle between he FitWithoutBrem J/ψ momentum and the FitWithBrem J/ψ momentum. The bottom row plots difference between the MaxChi2 (FitWithoutBrem minus FitWithBrem). When this difference is positive, when the FitWithBrem MaxChi2 is smaller, we use the fourvectors from the FitWithBrem. Similarly, when the difference is negative with use the FitWithoutBrem fourvectors.

CHAPTER 6

LIKELIHOOD FITTER

This section explains our unbinned likelihood fitter that takes into account all angular correlations.

6.1 Covariant Matrix Elements

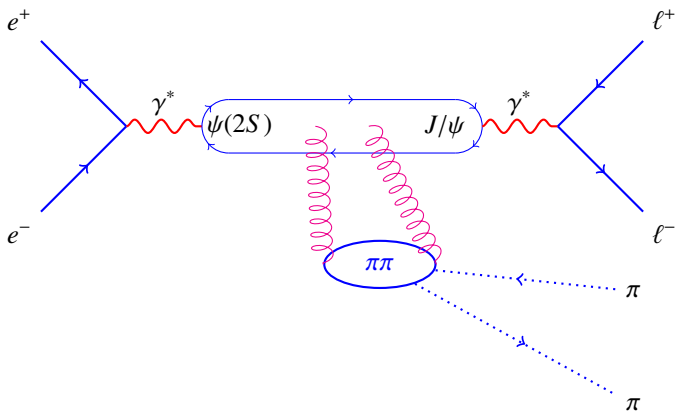

Figure 6.1: Feynman diagram for $\psi(2S) \to \pi\pi J/\psi$; $J/\psi \to \ell^+\ell^-$

Take a look at the above Feynman diagram, call λ' and λ the helicities of the $\psi(2S)$ and the J/ψ respectively, and write the amplitude as,

$$\langle e^+e^-|\mathcal{M}|\pi\pi\ell^+\ell^-\rangle = \sum_{\lambda',\lambda}\langle e^+e^-|\psi(2S)(\lambda')\rangle \times \langle \psi(2S)(\lambda')|\pi\pi J/\psi(\lambda)\rangle \times \langle J/\psi(\lambda)|\ell^+\ell^-\rangle. \quad (6.1)$$

Next, introduce polarization fourvectors, $\epsilon^{\mu}_{\lambda^{(\prime)}}$, to carry the $c\bar{c}$ spin-1 degrees of freedom, and write,

$$\mathcal{M} = \sum_{\lambda',\lambda} \underbrace{\bar{e}\gamma_\mu e\ \epsilon^{\mu *}_{\lambda'}}_{e^+e^-\to\psi(2S)(\lambda')} \times \underbrace{\epsilon^{\alpha}_{\lambda'}\mathcal{M}_{\alpha\beta}\epsilon^{\beta *}_{\lambda}}_{\psi(2S)(\lambda')\to\pi\pi J/\psi(\lambda)} \times \underbrace{\epsilon^{\nu}_{\lambda}\bar{\mu}\gamma_\nu\mu}_{J/\psi(\lambda)\to\ell^+\ell^-} \ . \tag{6.2}$$

These complex-valued fourvectors are nothing more than momentum-space representations of spin-1. However, the freedom to define the phase and quantization axis requires a convention, such as the canonical or helicity formalisms. It is possible to avoid these conventions by summing over helicities. The sum over λ' introduces a projection operator,

$$\sum_{\lambda'} \epsilon^{\mu *}_{\lambda'}\epsilon^{\alpha}_{\lambda'} = -g^{\mu\alpha} + \frac{p^{\mu}_{\psi(2S)}p^{\alpha}_{\psi(2S)}}{p^2_{\psi(2S)}}. \tag{6.3}$$

When applied to $\bar{e}\gamma_\mu e$, the projection operator acts as the *negative* identity. Similarly, the sum over λ creates a projection operator that can be absorbed into $\bar{\mu}\gamma_\nu\mu$, with another negative sign that cancels the first negative sign.

The result is a covariant expression that does not depend on a spin formalism,

$$\mathcal{M} = \bar{e}\gamma_\mu e\ \mathcal{M}^{\mu\nu}\ \bar{\mu}\gamma_\nu\mu. \tag{6.4}$$

This is our defining equation for the amplitude $\mathcal{M}^{\mu\nu}$. (The discussion involving helicities was only to help motivate eq. 6.4) The absolute square of the amplitude is then

$$|\mathcal{M}|^2 = \left(\bar{e}\gamma_\mu e\mathcal{M}^{\mu\nu}\bar{\mu}\gamma_\nu\mu\right)\left(\bar{e}\gamma_\alpha e\mathcal{M}^{\alpha\beta}\bar{\mu}\gamma_\beta\mu\right)^* . \tag{6.5}$$

The next step is to sum over external spins. You should start with the outgoing leptons, and recall how the spin-summed lepton current in $J/\psi \to \mu^+\mu^-$ is,

$$T^{\nu\beta} \equiv \sum_{\text{muon spins}} (\bar{\mu}\gamma^{\nu}\mu)\left(\bar{\mu}\gamma^{\beta}\mu\right)^{*} \propto p^{\nu}_{\mu^+} p^{\beta}_{\mu^-} + p^{\beta}_{\mu^+} p^{\nu}_{\mu^-} - g^{\nu\beta}\left(m^2_{\mu} + p_{\mu^+} \cdot p_{\mu^-}\right). \tag{6.6}$$

Use this $T^{\nu\beta}$ to write,

$$\sum_{\text{muon spins}} |\mathcal{M}|^2 \propto \bar{e}\gamma_{\mu} e \mathcal{M}^{\mu\nu} T_{\nu\beta} \mathcal{M}^{\alpha\beta *} (\bar{e}\gamma_{\alpha} e)^{*}. \tag{6.7}$$

At this point, it is easier to switch back to polarization fourvectors for $e^+e^- \to \psi(2S)$. When working in the $\psi(2S)$ rest frame, there is no convention ambiguity as both canonical and helicity formalisms use,

$$\boldsymbol{\epsilon}_{\pm} = \frac{\mp 1}{\sqrt{2}}(\hat{x} \pm i\hat{y}) \qquad \boldsymbol{\epsilon}_0 = \hat{z}. \tag{6.8}$$

If the $\psi(2S)$ has polarization fourvector $\boldsymbol{\epsilon_+}$, the probability of the transition, in matrix form, is

$$\sum_{\text{muon spins}} |\mathcal{M}|^2 \propto \boldsymbol{\epsilon}_{+} \mathcal{M} T \mathcal{M}^{\dagger} \boldsymbol{\epsilon}^{*}_{+}. \tag{6.9}$$

This result is sufficiently general because $\boldsymbol{\epsilon_-}$ contributes the same weight and the high-energy electrons do not allow for the $\psi(2S)$ to have a $\boldsymbol{\epsilon_0}$ polarization.

The expression in eq. 6.9 provides a probability density function for event kinematics. For notational convenience, let $\vec{\theta}$ denote the event kinematics ($\vec{\theta}$ is suggestive of "vector of angles" even though $\texttt{mass}(\pi\pi)$ is not an angle). With this notation, a glance at eq. 6.9 reveals how the dynamics of $\psi(2S) \to \pi^+\pi^- J/\psi$ are accounted for in the functional form,

$$\mathcal{M}^{\mu\nu} = \mathcal{M}^{\mu\nu}(\vec{\theta}). \tag{6.10}$$

Most theoretical parameterizations can be expressed as

$$\mathcal{M}^{\mu\nu}(\vec{\alpha}, \vec{\theta}) = \sum_k \alpha_k \mathcal{M}_k^{\mu\nu}(\vec{\theta}) \tag{6.11}$$

where $\vec{\alpha} = \{\alpha_i\}$ are unknown parameters. In other words, the probability density function of $\vec{\theta}$ given $\vec{\alpha}$ is

$$\begin{aligned} pdf(\vec{\theta}|\vec{\alpha}) &\propto \boldsymbol{\epsilon}_+(\vec{\theta})\mathcal{M}(\vec{\alpha}, \vec{\theta})T(\vec{\theta})\mathcal{M}(\vec{\alpha}, \vec{\theta})^\dagger \boldsymbol{\epsilon}_+(\vec{\theta})^* & (6.12)\\ &= \sum_i \alpha_i \alpha_j^* \underbrace{\boldsymbol{\epsilon}_+(\vec{\theta})\mathcal{M}_i(\vec{\theta})T(\vec{\theta})\mathcal{M}_j(\vec{\theta})^\dagger \boldsymbol{\epsilon}_+(\vec{\theta})^*}_{\mathcal{M}_{ij}(\vec{\theta})} & (6.13)\end{aligned}$$

The new symbol, $\mathcal{M}_{ij}(\vec{\theta})$, defined in eq. 6.13, is the weight of $\mathcal{M}_i^{\mu\nu}(\vec{\theta})$ interfering with $\mathcal{M}_j^{\mu\nu}(\vec{\theta})$. The pdf is nothing more than a quadratic form in $\vec{\alpha}$,

$$pdf(\vec{\theta}|\vec{\alpha}) \propto \sum_{ij} \alpha_i \alpha_j^* \, \mathcal{M}_{ij}(\vec{\theta}) \quad \text{where} \quad \mathcal{M}_{ij}(\vec{\theta}) = \boldsymbol{\epsilon}_+(\vec{\theta})\mathcal{M}_i(\vec{\theta})T(\vec{\theta})\mathcal{M}_j(\vec{\theta})^\dagger \boldsymbol{\epsilon}_+(\vec{\theta})^*. \tag{6.14}$$

6.2 The Likelihood

Now, the likelihood of an experiment (a set of n-measurements $\{\vec{\theta}_i\}_{i=1,\ldots,n}$) given parameters ($\vec{\alpha}$) may be written as

$$\mathcal{L}(\{\vec{\theta}_k\}|\vec{\alpha}) = \prod_k \frac{\epsilon(\vec{\theta}_k) pdf(\vec{\theta}_i|\vec{\alpha})}{N(\vec{\alpha})} = \prod_k \frac{\epsilon(\vec{\theta}_k)\left(\sum_{ij} \alpha_i \alpha_j^* \mathcal{M}_{ij}(\vec{\theta}_i)\right)}{N(\vec{\alpha})}. \tag{6.15}$$

The product is taken over all reconstructed events (passing event selection) and combines an efficiency, $\epsilon(\vec{\theta})$, with the pdf taken from eq. 6.14, and a normalization, $N(\vec{\alpha})$. At this point there are two issues:

1. The point-wise efficiency, $\epsilon = \epsilon(\vec{\theta})$, is impossible to estimate from `MC` because there are too many degrees of freedom. Specifically, $\epsilon(\vec{\theta})$ is a map from $\mathbb{R}^d \to \mathbb{R}$ where d is the number of degrees of freedom. A value of $d = 4\times3-4-1 = 7$ may be found by taking 4 outgoing on-shell particles, and subtracting off a constrained initial four-momentum, and the J/ψ mass. Using 100 bins per dimension would therefore require a simulation capable of populating 100^7 bins.
2. It is not at all obvious how to compute the normalization, $N(\vec{\alpha})$, given that it depends on $\epsilon(\vec{\theta})$ and the unnormalized pdf in eq. 6.14.

The first problem has a fiendishly clever solution that David Cassel attributes to Robert Perchonok who developed it for a 1981 Cornell anlaysis [6]. The idea is use the logarithm to break eq. 6.15 into two terms,

$$\log \mathcal{L}(\{\vec{\theta}_k\}|\vec{\alpha}) = \sum_k \log \epsilon(\vec{\theta}_k) + \sum_k \log \frac{\left(\sum_{ij} \alpha_i \alpha_j^* \mathcal{M}_{ij}(\vec{\theta}_k)\right)}{N(\vec{\alpha})} \tag{6.16}$$

The point-wise efficiency, $\epsilon(\vec{\theta}_i)$, is now isolated in the first term on the right-hand-side of eq. 6.16. This term is a constant with respect to $\vec{\alpha}$. And since the eventual goal is to maximize $\log \mathcal{L}$ with respect to $\vec{\alpha}$, the numerical values of $\epsilon(\vec{\theta}_i)$ never need to be computed.

To tackle the second problem, the computation of $N(\vec{\alpha})$, use eq. 6.15 and write

$$N(\vec{\alpha}) = \int d\vec{\theta}\, \epsilon(\vec{\theta}) \left(\sum_{ij} \alpha_i \alpha_j^* \mathcal{M}_{ij}(\vec{\theta}) \right) \tag{6.17}$$

$$= \sum_{ij} \alpha_i \alpha_j^* \underbrace{\int d\vec{\theta}\, \epsilon(\vec{\theta}) \mathcal{M}_{ij}(\vec{\theta})}_{N_{ij}}. \tag{6.18}$$

The numbers, N_{ij}, may be estimated from `MC`. If n events are reconstructed (`cleog` and `mcpass2`) and event-selected from N phase space decays, produced by the EvtGen PHSP Model for $\psi(2S) \to \pi\pi J/\psi$, an estimate for N_{ij} is,

$$N_{ij} = \frac{1}{N} \sum_{k=1}^{n} \mathcal{M}_{ij}(\vec{\theta}_k) \qquad \text{where the sum only includes events passing all cuts.} \tag{6.19}$$

Combining eq. 6.18 with eq. 6.16, and removing the point-wise efficiency term, gives a log-likelihood that can be maximized with respect to $\vec{\alpha}$,

$$\mathcal{W}(\{\vec{\theta}_k\}|\vec{\alpha}) \equiv \sum_k \log \frac{\sum_{ij} \alpha_i \alpha_j^* \mathcal{M}_{ij}(\vec{\theta}_k)}{\sum_{ij} \alpha_i \alpha_j^* N_{ij}}. \tag{6.20}$$

6.3 Numerical Maximization

The fitter numerically maximizes eq. 6.20 with respect to $\vec{\alpha}$. In doing so, we are implicitly assuming $\mathcal{W}(\vec{\alpha}|\{\vec{\theta}_k\}) \propto \mathcal{W}(\{\vec{\theta}_k\}|\vec{\alpha})$. This is the frequentist perspective where the Bayesian priors on $\vec{\alpha}$ are uniform. The result of numerical maximization is a maximum likelihood estimator (MLE) for $\vec{\alpha}$,

$$\widehat{\vec{\alpha}} = \arg\max \mathcal{W}(\vec{\alpha}|\{\vec{\theta}_i\}). \tag{6.21}$$

The "arg max" is shorthand for "the argument that maximizes" and the $\widehat{\ }$ in $\widehat{\vec{\alpha}}$ turns $\vec{\alpha}$ into a random variable with respect to an ensemble of experiments,

As the number of events becomes large, the distribution of $\widehat{\vec{\alpha}}$ across multiple experiments asymptotically approaches a multivariate normal distribution. By definition, this distribution takes the form,

$$pdf(\widehat{\vec{\alpha}}) \sim \frac{1}{\sqrt{|\Sigma|}} exp\left(-\frac{1}{2}\left(\widehat{\vec{\alpha}} - \widehat{\vec{\alpha}_0}\right)^T \Sigma^{-1} \left(\widehat{\vec{\alpha}} - \widehat{\vec{\alpha}_0}\right)\right) \text{ where } \Sigma \text{ is the covariance matrix.} \tag{6.22}$$

Somewhat remarkably, the covariance matrix for the $\widehat{\vec{\alpha}}$ may be estimated directly from the log-likelihood, in the sense that,

$$\mathcal{W}(\vec{\alpha}|\{\vec{\theta}_k\}) \sim \text{constant} - \frac{1}{2}\left(\vec{\alpha} - \vec{\alpha}_0\right)^T \Sigma^{-1} \left(\vec{\alpha} - \vec{\alpha}_0\right). \tag{6.23}$$

After finding optimal value of $\vec{\alpha}$, our fitter uses eq. 6.23 to estimate errors on $\widehat{\vec{\alpha}}$. The matrix of numerical second derivatives, when inverted, estimates Σ. This covariance matrix will give symmetric errors on the components of $\vec{\alpha}$. Of course, the asymptotic condition in eq. 6.23 is never perfect. As such, any asymmetric errors are estimated by walking away from the MLE until the log-likelihood drops by $1/2$.

6.4 The Parameter Map and Implementation Details

Specifying a model is equivalent to providing the fitter with the following expansion (see eq. 6.11),

$$\mathcal{M}^{\mu\nu}(\vec{\alpha},\vec{\theta}) = \sum_i \alpha_i \mathcal{M}_i^{\mu\nu}(\vec{\theta}). \tag{6.24}$$

6.4.1 Implementing the ABCλ Model

For example, the ABCλ model,

$$\mathcal{M} = \mathcal{A}\left[(q^2 - 2m_\pi^2) + \lambda m_\pi^2\right]\epsilon' \cdot \epsilon + \mathcal{B}E_1E_2\epsilon' \cdot \epsilon + C\left(\epsilon' \cdot q_1\epsilon \cdot q_2 + \epsilon' \cdot q_2\epsilon \cdot q_1\right), \tag{6.25}$$

in the notation of eq. 6.24 is,

$$\mathcal{M}^{\mu\nu}(\vec{\alpha},\vec{\theta}) = \underbrace{\mathcal{A}}_{\alpha_1}\underbrace{(q^2 - 2m_\pi^2)g^{\mu\nu}}_{\mathcal{M}_1^{\mu\nu}} + \underbrace{\lambda}_{\alpha_2}\underbrace{m_\pi^2 g^{\mu\nu}}_{\mathcal{M}_2^{\mu\nu}} + \underbrace{\mathcal{B}}_{\alpha_3}\underbrace{E_1E_2g^{\mu\nu}}_{\mathcal{M}_3^{\mu\nu}} + \underbrace{C}_{\alpha_4}\underbrace{\left(q_1^\mu q_2^\nu + q_2^\mu q_1^\nu\right)}_{\mathcal{M}_4^{\mu\nu}} \tag{6.26}$$

The meaning of each symbol is provided in the following table.

Table 6.1: Symbols for ABCλ.

$\mathcal{A}, \mathcal{B}, C$	form factors
λ	form factor (the σ-term) ; "should be small"
ϵ' and ϵ	polarization fourvectors of the $\psi(2S)$ and J/ψ
q_1 and q_2	fourvectors of the two pions
E_1 and E_2	energies of the pions in the $\psi(2S)$ rest frame
q^2	squared mass of dipion system

In practice, $\mathcal{A}$ is set to unity and the fitter extracts $\mathcal{B}/\mathcal{A}$, $C/\mathcal{A}$ and $\lambda/\mathcal{A}$. In other words, there are only three parameters in the fit. This is indeed a subtlety in the notation: the components of the "parameter vector" $\vec{\alpha}$ need not be independent. Internally, the fitter

has a list of parameters $p_1, p_2, \ldots, p_n$, which get mapped to $\vec{\alpha}$. The map for the ABCλ model is,

$$\alpha_1(p_1, p_2, p_3) = 1 \tag{6.27}$$

$$\alpha_2(p_1, p_2, p_3) = p_1 \tag{6.28}$$

$$\alpha_3(p_1, p_2, p_3) = p_2 \tag{6.29}$$

$$\alpha_4(p_1, p_2, p_3) = p_3. \tag{6.30}$$

The three parameters p_1, p_2, and p_3 are interpreted as $\mathcal{B}/\mathcal{A}$, $C/\mathcal{A}$ and $\lambda/\mathcal{A}$ respectively. So why are we making things confusing? The answer is in terms of computational efficiency. We treat the $\mathcal{M}_i^{\mu\nu}$ matrices as constants with respect to the data. By caching them at start-up, we get a huge boost in fitting speed. Our jargon calls $\vec{\alpha}$ parameters in the sense that the components get recomputed during each iteration of the fit. This setup has one crucial constraint: *the map from p_i, the true parameters, to $\vec{\alpha}$ cannot depend on event kinematics*. Imposing this constraint allows us to avoid looping through the data during each iteration of the fit. In fact, once the $\mathcal{M}_i^{\mu\nu}$ values are cached, the data can be purged from memory.

In terms of implementation details, it is worth pointing out that nearly everything we compute is in terms of fourvectors. The "vector of angles," $\vec{\theta}$, should really be thought of as five fourvectors, representing the four final state particles and the initial $\psi(2S)$. See figure 6.2 for example analysis code that computes the $\mathcal{M}_i^{\mu\nu}$ for the ABCλ model.

```
  void AAmp::update(const DiPion& dipion)
  {
      double scale =
          dipion.pipi_p4().m2() -
          2 *
          dipion.first_pion_p4().m() *
          dipion.second_pion_p4().m();

      m_M.set_to_scaled_metric(scale);
  }

  void LambdaAmp::update(const DiPion& dipion)
  {
      double scale = dipion.first_pion_p4().m() *
                     dipion.second_pion_p4().m();

      m_M.set_to_scaled_metric(scale);
  }
void BAmp::update(const DiPion& dipion)
{
    FourVector lab(dipion.lab_momentum_p4());
    double m = lab.m();
    double E1 = (dipion.first_pion_p4() * lab) / m;
    double E2 = (dipion.second_pion_p4() * lab) / m;

    m_M.set_to_scaled_metric(E1 * E2);
}


void CAmp::update(const DiPion& dipion)
{
    FourVector q1 = dipion.first_pion_p4();
    FourVector q2 = dipion.second_pion_p4();

    m_M = Tensor(q1,q2) + Tensor(q2,q1);
}
```

Figure 6.2: Above is the analysis code for the ABCλ model that updates the four $\mathcal{M}_i^{\mu\nu}$ matrices.

6.4.2 Implementing the KappaFSI Model

We start with the natural yet improper way to write the KappaFSI Model (see eq. 4.16 and eq. 4.18) in the notation of eq. 6.24,

Will Not Work:
$$\mathcal{M}^{\mu\nu}(\vec{\alpha},\vec{\theta}) = \underbrace{1}_{\alpha_1}\underbrace{\left(q^2+m_\pi^2\right)g^{\mu\nu}}_{\mathcal{M}_1^{\mu\nu}} + \underbrace{-\kappa}_{\alpha_2}\underbrace{\left(1+\frac{2m^2}{q^2}\right)\left(\frac{(q\cdot P')^2}{P'^2}-\frac{1}{4}q^2\right)g^{\mu\nu}}_{\mathcal{M}_2^{\mu\nu}} + \underbrace{e^{-i\Delta\delta(q)}\frac{3\kappa}{2}}_{\alpha_3}\underbrace{\frac{l_{\mu\nu}P'^{\mu}P'^{\nu}}{P'^2}g^{\mu\nu}}_{\mathcal{M}_3^{\mu\nu}} \quad . \tag{6.31}$$

The problem is that the implied parameter map,

$$\begin{aligned}
\alpha_1(\kappa,a,b) &= 1 \\
\alpha_2(\kappa,a,b) &= -\kappa \\
\alpha_3(\kappa,a,b) &= e^{-i(a+bx))}\frac{3\kappa}{2} \quad \text{where} \quad x=\frac{(q-464\text{ MeV})}{124\text{ MeV}},
\end{aligned} \tag{6.32}$$

now depends on q, an event kinematic, which is not allowed. We get around this problem by expanding the exponential in a power series,

$$e^{-i(a+bx)} = \sum_{j=0}^{\infty} c_j(a,b)x^j \quad , \tag{6.33}$$

where, $c_j(a,b) = (-ib)^j e^{-ia}$. We can easily truncate the series after a few terms without loss of precision (we conservatibly keep six terms). This allow us to preserve the "no kinematics" rule for the parameter map, by writing,

$$\mathcal{M}^{\mu\nu}(\vec{\alpha},\vec{\theta}) = \underbrace{1}_{\alpha_1}\underbrace{\left(q^2+m_\pi^2\right)g^{\mu\nu}}_{\mathcal{M}_1^{\mu\nu}} + \underbrace{-\kappa}_{\alpha_2}\underbrace{\left(1+\frac{2m^2}{q^2}\right)\left(\frac{(q\cdot P')^2}{P'^2}-\frac{1}{4}q^2\right)g^{\mu\nu}}_{\mathcal{M}_2^{\mu\nu}}$$
$$+ \underbrace{c_0(a,b)\frac{3\kappa}{2}}_{\alpha_3}\times\underbrace{x^0\times\frac{l_{\mu\nu}P'^\mu P'^\nu}{P'^2}g^{\mu\nu}}_{\mathcal{M}_3^{\mu\nu}}$$
$$+ \underbrace{c_1(a,b)\frac{3\kappa}{2}}_{\alpha_4}\times\underbrace{x^1\times\frac{l_{\mu\nu}P'^\mu P'^\nu}{P'^2}g^{\mu\nu}}_{\mathcal{M}_4^{\mu\nu}} \tag{6.34}$$
$$\vdots \qquad\qquad \vdots \qquad . \tag{6.35}$$

where the parameter map is,

$$\begin{aligned}
\alpha_1(\kappa,a,b) &= 1\\
\alpha_2(\kappa,a,b) &= -\kappa\\
\alpha_3(\kappa,a,b) &= c_0(a,b)\frac{3\kappa}{2}\\
\alpha_4(\kappa,a,b) &= c_1(a,b)\frac{3\kappa}{2}\\
\vdots \quad &\quad \vdots\\
\alpha_{j+3}(\kappa,a,b) &= c_j(a,b)\frac{3\kappa}{2}
\end{aligned} \tag{6.36}$$

6.4.3 Implementing the Binned Fit

The binned fit, the one introduced in section 4.6.2, is essentially a cut on $\texttt{mass}(\pi\pi)$. We take ten 25 MeV Bins from 340 MeV to 590 MeV. For each bin, a cut on $\texttt{mass}(\pi\pi)$ is imposed, data is selected, normalization is computed, and a fit is performed. Since the fitter extracts *shape* parameters, and the data is restricted to one bin, it is only possible

to measure the $\mathcal{D}/\mathcal{S}$ ratio. When converting eq. 4.24 into the notation of eq. 6.11, we get,

$$\mathcal{M}^{\mu\nu} = \underbrace{1}_{\alpha_1} \times \underbrace{g^{\mu\nu}}_{\mathcal{M}_1^{\mu\nu}} + \underbrace{(a_i + b_i i)}_{\alpha_2} \underbrace{d^2_{00}(\cos\theta_{\texttt{helicity}}) g^{\mu\nu}}_{\mathcal{M}_2^{\mu\nu}}, \tag{6.37}$$

where

$$\begin{aligned} \alpha_1(a,b) &= 1 \\ \alpha_2(a,b) &= a + bi \quad . \end{aligned} \tag{6.38}$$

CHAPTER 7

STATISTICAL AND SYSTEMATIC ERROR

The starting point for our treatment of error is a full detector simulation of $e^+e^- \to \psi(2S) \to \pi\pi J/\psi$, $J/\psi \to \ell^+\ell^-$ where only phase space weights $\psi(2S) \to \pi\pi J/\psi$. By appropriately reweighting this MC, we can perform a number of systematic checks. The decays are generated by EvtGen and sent through `cleog` and `mcpass2`. We use the `20060802_MCP2_A_1` release. We use Photos to add final state radiation to the J/ψ decay. The 3-body $\psi(2S) \to \pi\pi J/\psi$ decay uses the EvtGen `PHSP` model. Table 7.1 lists, by channel, the number of reconstructed events passing all cuts. We refer to these datasets as `PhaseSpaceMC`.

Table 7.1: Number of reconstructed events (passing event selection) in our `PhaseSpaceMC`.

Channel	Reconstructed Events
$\pi^+\pi^-(\mu^+\mu^-)$	2,095,271
$\pi^+\pi^-(e^+e^-)$	1,989,037
$\pi^0\pi^0(\mu^+\mu^-)$	876,340
$\pi^0\pi^0(e^+e^-)$	832,978

In what follows, we use the `Kappa` Model as the stereotypical example. Figure 7.1 shows the fit results for the `Kappa` Model (figure 7.1 is identical to figure 3.1 and reproduced here for convenience). Our plan is to quote the charged result, $\pi^+\pi^-(\ell^+\ell^-)$, and the neutral results, $\pi^0\pi^0(\ell^+\ell^-)$.

In other words, the following sections will explain how to put systematic error on $\kappa_{\pi^+\pi^-(\ell^+\ell^-)} = 0.2740 \pm 0.0006_{\texttt{stat}}$ and $\kappa_{\pi^0\pi^0(\ell^+\ell^-)} = 0.2757 \pm 0.0015_{\texttt{stat}}$. But even at this point, we could quote an estimate of systematic error merely from the neutral vs. charged disagreement. Reading off difference between $\pi^+\pi^-(\ell^+\ell^-)$ and $\pi^0\pi^0(\ell^+\ell^-)$ we get $\Delta\kappa = 0.0017$, which is the same order as the neutral statistical error.

channel	κ	stat error
$\pi^+\pi^-(\mu^+\mu^-)$	0.2744	0.0009
$\pi^+\pi^-(e^+e^-)$	0.2735	0.0009
$\pi^0\pi^0(\mu^+\mu^-)$	0.2732	0.0021
$\pi^0\pi^0(e^+e^-)$	0.2785	0.0021
$\pi^+\pi^-(\ell^+\ell^-)$	0.2740	0.0006
$\pi^0\pi^0(\ell^+\ell^-)$	0.2757	0.0015
$\pi\pi(\ell^+\ell^-)$	0.2743	0.0006

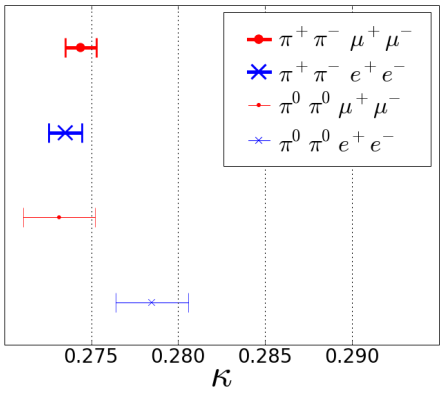

Figure 7.1: Fit results for the `Kappa` Model in our `Data` . The quoted errors are the symmetric, statistical errors as computed by the likelihood fitter.

7.1 Calculating Normalization Coefficients

Although calculating normalization coefficients is not a systematic check, we give an example because these coefficients will be *recalculated* in later sections.

Table 7.2: Normalization coefficient matrices for the `Kappa` Model.

$\pi^+\pi^-(\mu^+\mu^-)$

+0.735976	+0.933198	−0.004203
	+1.313892	−0.007686
		+0.003938

$\pi^0\pi^0(\mu^+\mu^-)$

+0.754912	+0.933321	+0.010242
	+1.280971	+0.017060
		+0.005717

$\pi^+\pi^-(e^+e^-)$

+0.732313	+0.928376	−0.004141
	+1.306897	−0.007548
		+0.003917

$\pi^0\pi^0(e^+e^-)$

+0.752318	+0.930802	+0.010126
	+1.278454	+0.016898
		+0.005707

For each channel of `PhaseSpaceMC`, we compute a symmetric matrix of normalization coefficients. For the `Kappa` Model, this matrix is 3×3. Specifically, in the language of eq. 6.11, the `Kappa` Model is,

$$\mathcal{M}^{\mu\nu} = \underbrace{1}_{\alpha_1} \times \underbrace{\left(q^2 + m_\pi^2\right)(g^{\mu\nu})}_{\mathcal{M}_1^{\mu\nu}} + \underbrace{-\kappa}_{\alpha_2} \underbrace{\left(1 + \frac{2m^2}{q^2}\right)\left(\frac{(q\cdot P')^2}{P'^2} - \frac{1}{4}q^2\right)(g^{\mu\nu})}_{\mathcal{M}_2^{\mu\nu}} + \underbrace{\frac{3\kappa}{2}}_{\alpha_3} \underbrace{\frac{l_{\alpha\beta}P'^\alpha P'^\beta}{P'^2}(g^{\mu\nu})}_{\mathcal{M}_3^{\mu\nu}}. \tag{7.1}$$

and the normalization coefficients are the integrated efficiencies of $\mathcal{M}_i^{\mu\nu}$ interfering with $\mathcal{M}_j^{\mu\nu}$ (see the discussion between equations 6.13 and 6.19, starting on page 60). Also, notice how this is an example where the components of $\vec{\alpha}$ are not independent. The `Kappa` Model normalization coefficients for $\pi^+\pi^-(\mu^+\mu^-)$, $\pi^0\pi^0(\mu^+\mu^-)$,$\pi^+\pi^-(e^+e^-)$, $\pi^0\pi^0(e^+e^-)$, are in table 7.2.

7.2 Resolution Smearing and Statistical Fluctuations

We need to verify that the fitter's estimate of the statistical error gives reasonable results. We also need to estimate the systematic error from resolution smearing.

Continuing with the `Kappa` Model as an example, we take the fitted value of κ for $\pi^+\pi^-(\ell^+\ell^-)$ in our `Data` , 0.2740, and use the `Kappa` Model pdf at this optimal value to reweight the charged transitions in `PhaseSpaceMC`. For neutral transitions, we use the fitted value of κ for $\pi^0\pi^0(\ell^+\ell^-)$ in our `Data` , 0.2757. We then sample (with an accept-reject algorithm) from these datasets to simulate experiments. We sample the same number of events as were found in our `Data` on a per channel basis. That means, for example, that each pseudo-experiment has 302,345 events in $\pi^+\pi^-(\mu^+\mu^-)$ (see table 5.1 on page 46). Then for each experiment we perform the fit on the kinematically fitted `Geant`-smeared fourvectors.

We then compute the mean and standard deviation of the fitted values of κ across these pseudo-experiments. We then quote a sytematic error that adds the standard deviation and bias (from the mean) in quadrature. The result for the `Kappa` Model is,

$$\begin{aligned} \kappa_{\pi^+\pi^-(\ell^+\ell^-)} &= 0.2740 \pm 0.0006_{\texttt{stat}} \pm \mathbf{0.0006}_{\texttt{reso}} \\ \kappa_{\pi^0\pi^0(\ell^+\ell^-)} &= 0.2757 \pm 0.0015_{\texttt{stat}} \pm \mathbf{0.0025}_{\texttt{reso}}. \end{aligned} \tag{7.2}$$

This technique is overly conservature in that it double-counts statistical error. Putting it a different way, the minimum "systematic error" quoted here is bounded below by the true statistical error. But this procedure has its advantages as it can be automated across different models and does not require a detailed investigation of where the systematic erorr is coming from. For example, we do not need to differentiate a smearing induced

expanded variance from a fitting bias at the level of MC-Truth.

7.3 Cut Variation

There is a systematic error associated with the Generic MC mismodelling the shape of kinematic distributions which receive event selection cuts. We investigate variation in the E/p Lepton-ID (see section 5.1), the $\pi\pi$ recoil mass window (see section 5.3), MaxChi2 (see section 5.5), and neutral pion selection (see section 5.2).

Table 7.3 shows the variations we use along with the fit result shifts for the Kappa Model. The "Charged $\Delta\kappa$" and "Neutral $\Delta\kappa$" columns mean the shift in κ due to the cut variation in $\pi^+\pi^-(\ell^+\ell^-)$ and $\pi^0\pi^0(\ell^+\ell^-)$ respectively. The first three rows in the table reference cut variations that can be made in two directions. For example, the E/p cut can move from 0.6 to 0.7 or 0.6 to 0.5. The change quoted in the table is the larger of these two variations. The total systematic is the sum of all contributions added in quadrature.

The plots on the following pages compare Generic MC and our Data across the four channels in the vicinity of cut variation. The recoil mass window is on page 76. The MaxChi2 cut is on page 77. The unconstrained π^0 mass is on page 77. The minimum photon energy is on page 78. The π^0 shower cosine is on page 79. After including the cut variation, the results for the Kappa Model are,

$$\begin{aligned} \kappa_{\pi^+\pi^-(\ell^+\ell^-)} &= 0.2740 \pm 0.0006_{\mathtt{stat}} \pm 0.0006_{\mathtt{reso}} \pm \mathbf{0.0002}_{\mathtt{cuts}} \\ \kappa_{\pi^0\pi^0(\ell^+\ell^-)} &= 0.2757 \pm 0.0015_{\mathtt{stat}} \pm 0.0025_{\mathtt{reso}} \pm \mathbf{0.0019}_{\mathtt{cuts}}. \end{aligned} \tag{7.3}$$

Table 7.3 also shows (in parentheses) the change in data sample size after applying the cut and statistical significance of the cut variation. For exampe, the π^0 mass cut variation of 0.00170 has a statistical signifiance of 5.7σ. (A subset fit on $p\%$ of the data is expected to have a variance of $p/(1-p)$ relative to the superset variance; when $p = 0.96$, $\sqrt{p/(1-p)} \times 0.0015_{\texttt{stat}} \approx 0.0003$ and $0.00170/0.0003 \approx 5.7\sigma$.)

Table 7.3: Cut Variation for the Kappa Model.

Cut Variation	Charged $\Delta\kappa$	Neutral $\Delta\kappa$
E/p (0.6 ± 0.1)	0.00001 (100%; 6.2σ)	0.00001 (100%; $\infty\sigma$)
recoil($\pi\pi$) $(20 \pm 5$MeV)	0.00004 (99%; 1.0σ)	0.00046 (92%; 1.0σ)
max $\chi^2/d.o.f.$ (50 ± 10)	0.00018 (101%; 2.7σ)	0.00008 (101%; 0.6σ)
E_γ $(> 30\text{MeV} \rightarrow > 40\text{MeV})$		0.00044 (82%; 0.7σ)
π^0 mass $(\rightarrow$ 100 MeV-160 MeV)		0.00170 (96%; 5.7σ)
$\lvert\cos(\gamma)\rvert$ $(\rightarrow < 0.70)$		0.00054 (64%; 0.5σ)
Total (in quadrature)	0.00018	0.00190

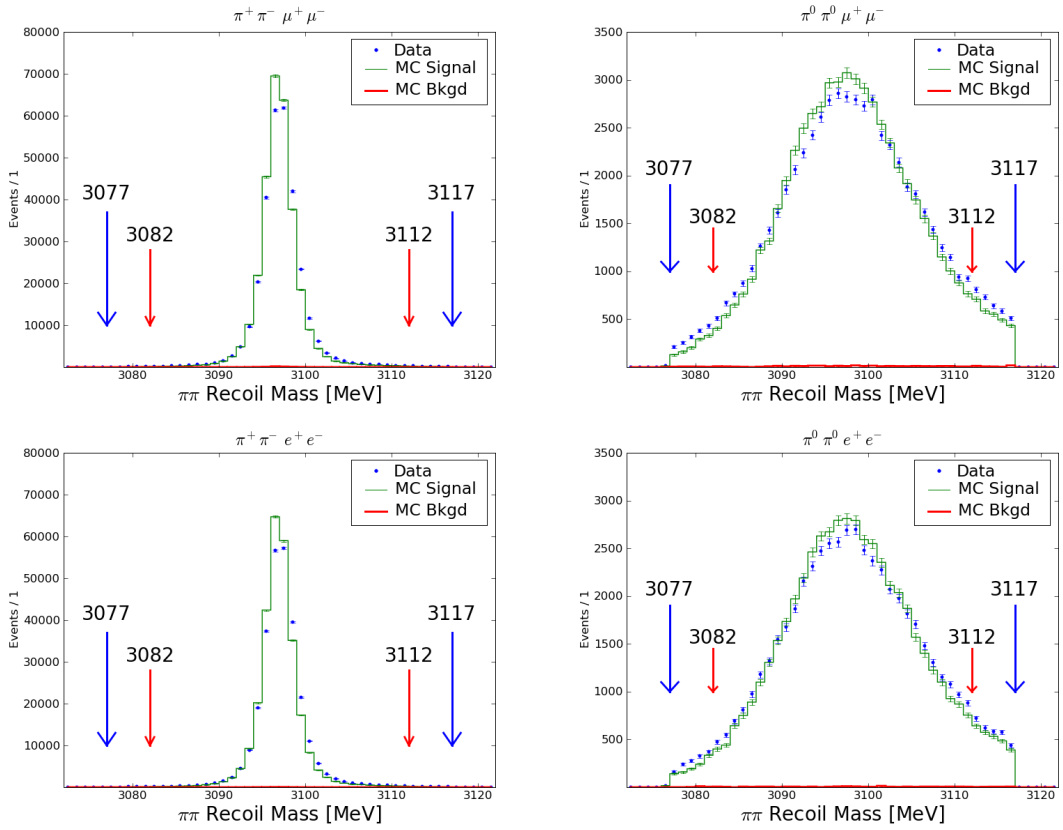

Figure 7.2: The $\pi\pi$ recoil mass cuts. The units are MeV. The loose cut (±25) is at the edge of the histograms. The standard cut (±20MeV) and tight cut (±15MeV) are shown.

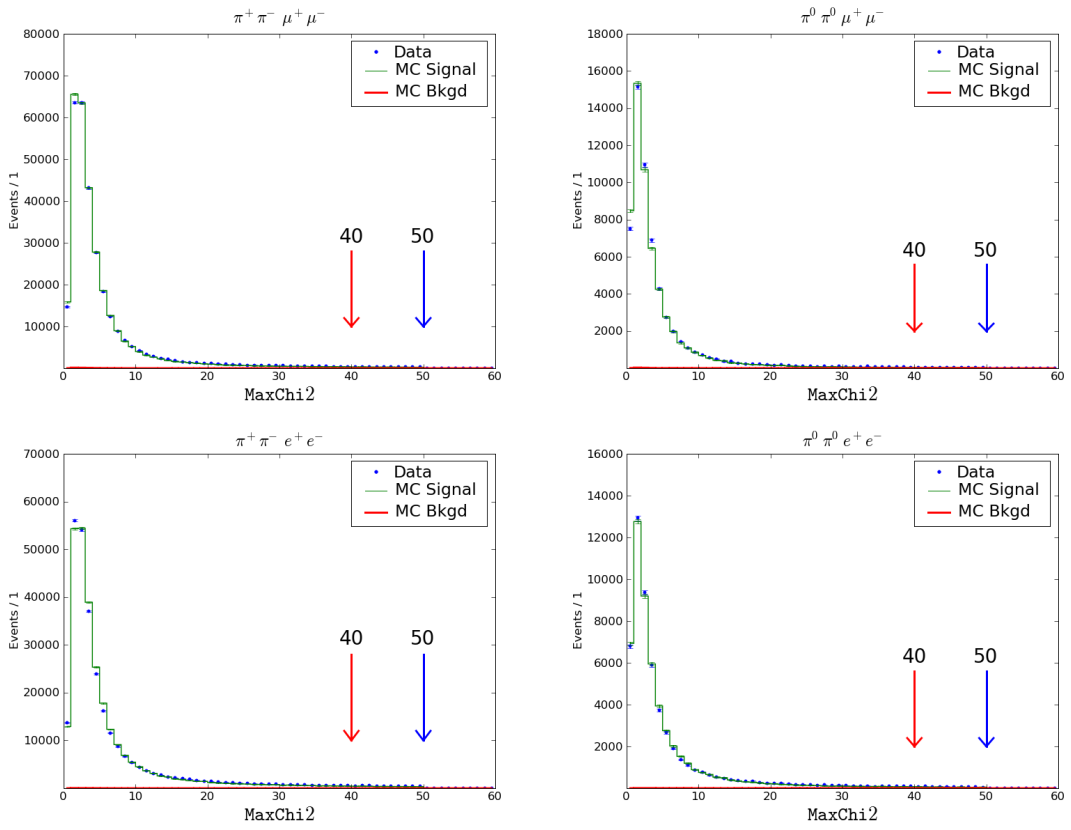

Figure 7.3: The `MaxChi2` standard cut at 50, tight cut at 40 and loose cut at 60 (edge of plot).

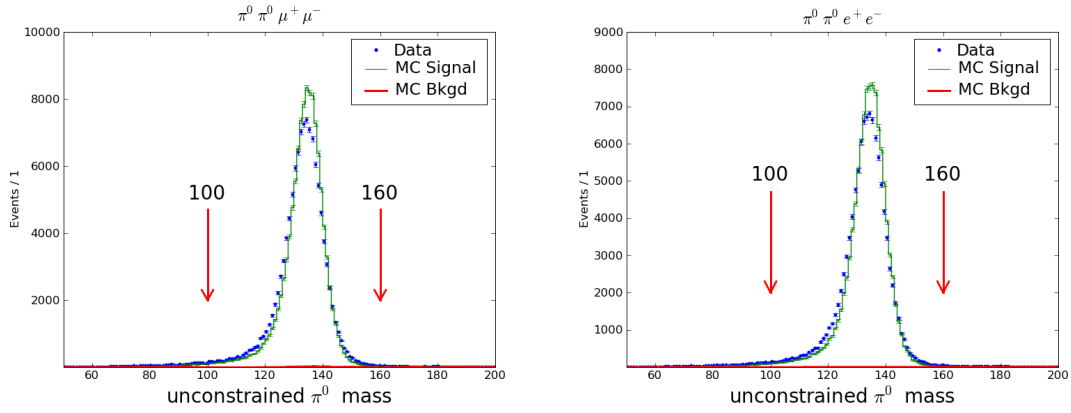

Figure 7.4: The unconstrained π^0 mass cut. Normally, there is no cut. The tight cut (100 MeV to 160 MeV) is shown.

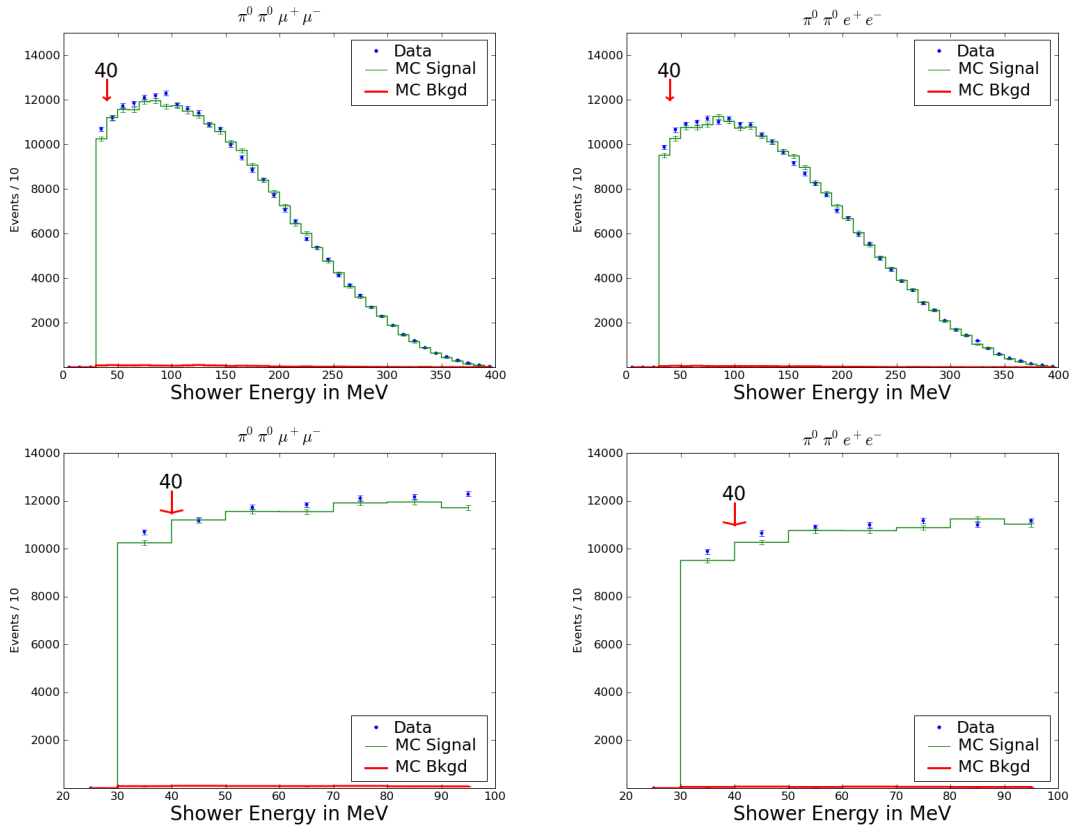

Figure 7.5: The minimum photon energy cut in $\pi^0 \to \gamma\gamma$. The first and second column are $\pi^0\pi^0\mu^+\mu^-$ and $\pi^0\pi^0 e^+e^-$. The second row changes the binning. The standard cut ($E_\gamma > 30$ MeV) is not labeled but is visible where the histogram goes to zero. The tight cut ($E_\gamma > 40$ MeV) is labeled.

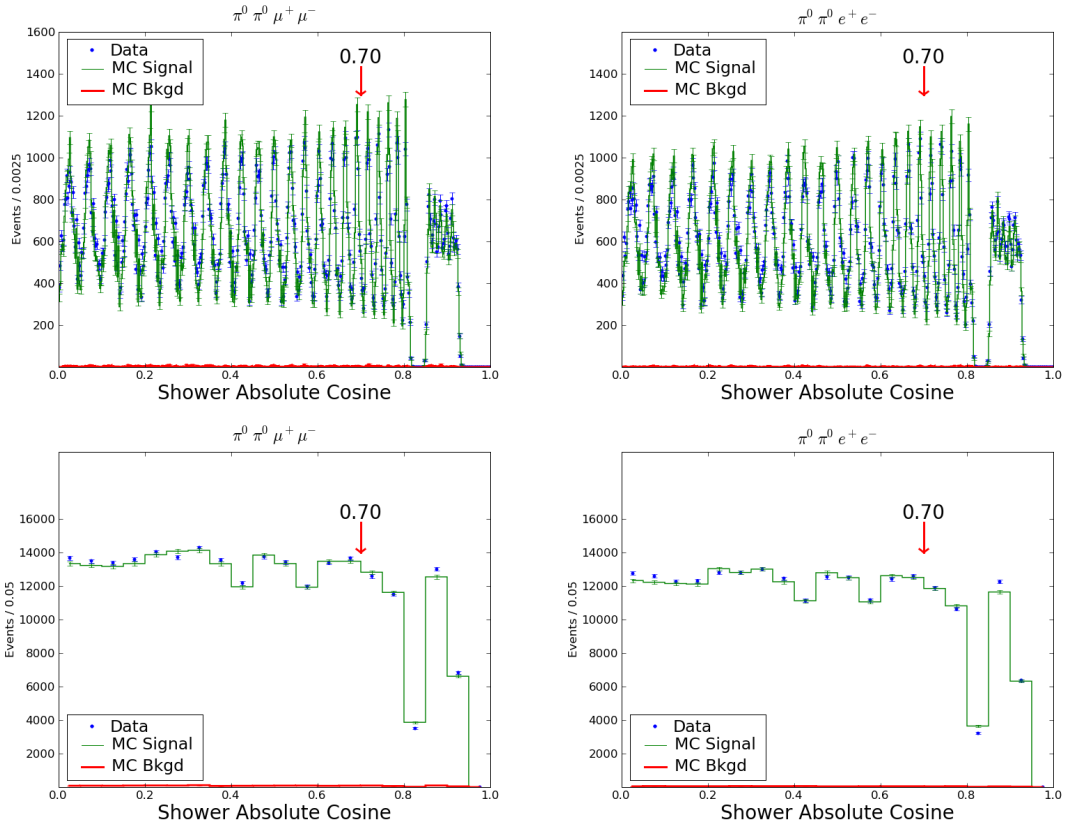

Figure 7.6: The maximum absolute value of the photon cosine cut in $\pi^0 \to \gamma\gamma$. The first and second column are $\pi^0\pi^0\mu^+\mu^-$ and $\pi^0\pi^0 e^+e^-$. The second row changes the binning. The tight cut is shown. The standard cuts are good barrel and good endcap.

7.4 Pion Tracking Efficiency

The normalization coefficients in the likelihood fitter are calculated from MC. We need to estimate any systematic problems with this computation. It is important to point out how the difference in efficiency shapes between neutral and charged transitions already offers an essential crosscheck in this analysis. Nevertheless, in this section, we go further and use our Data to reweight the efficiency.

We exploit the fact that the kinematics in $\psi(2S) \to \pi\pi J/\psi$; $J/\psi \to \ell^+\ell^-$ are over-constrained. This allows us to select events of the form,

$$\psi(2S) \to \pi J/\psi \;\; ; \;\; J/\psi \to \ell^+\ell^-, \tag{7.4}$$

and determine whether there should be a second π merely by looking at the missing fourmomentum. The trick here is that we can ask the question in both our Data and MC. We then ask whether or not the tracking system actually sees the second pion and compare how well MC predicts the answer in our Data .

We need to be precise about what we measure. Generally speaking, we can write the pointwise efficiency in the form,

$$\epsilon(\texttt{Event Selection}) = \epsilon(\texttt{B}|\texttt{A}) \times \epsilon(\texttt{A}), \tag{7.5}$$

where A and B are currently unspecified criteria. The notation "B|A" means "B given A." We assume ϵ(A) is perfectly modeled in MC, and compare how well ϵ(B|A) in MC agrees with ϵ(B|A) in our Data . The answer will be in the form of a ratio,

$$\frac{\epsilon_{our}\texttt{Data(B|A)}}{\epsilon_{\texttt{MC}}\texttt{(B|A)}}. \tag{7.6}$$

We project this *pointwise* ratio onto various kinematic variables in an attempt to find the largest disagreement.

Roughly speaking, we define A to mean that we have a good kinematically fit $J/\psi \to \ell^+\ell^-$, one pion and a missing mass consistent with a second pion. Our definition of B is the presence of a second pion and a successful 4C kinematic fit.

The cuts are the same as event selection (section 5) with a few qualifications. For charged transitions, after 1C fitting the $J/\psi \to \ell^+\ell^-$, we select events with at least one additional track and compute the missing fourmomentum and cut on the missing mass: 75MeV < MM < 200MeV. If there are two charged pions present, we keep the event if one of the two missing fourmomenta pass the missing mass cut. This is condition A. The meaning of ϵ(B|A) is the presence of a second charged pion (of opposite charge) and a successful 4C fit.

For neutral transitions, the presense of seven or more showers disqualifies the event. For each combination of three showers, we compute a squared missing mass. Events without a squared missing mass below 200 MeV^2 are skipped. We then select the shower triplet with the smallest missing mass. There are three possible π^0 configurations that may decay to two of these three showers. For each of these, we look for a π^0 reconstructed by PhotonsDecayProd. We select the π^0 from the three possibilities by taking the one with a missing mass closests to m_{π^0}. The last step is to apply the same missing mass cut: 75MeV < MM < 200MeV. This is condition A. The meaning of ϵ(B|A) is then the usual $\pi^0\pi^0$ event selection with a 4C fit.

We stress that ϵ(B|A) should *not* be interpreted as the efficiency of seeing a π. Rather,

it is the efficiency of reconstructing a *second* π (and getting a good 4C fit) under the above algorithm. Figure 7.7 plots the missing mass cut, 75MeV $<$ MM $<$ 200MeV, across the four channels.

We then investigate the ϵ_{our}Data(B|A)/ϵ_{MC}(B|A) ratio as a function of all the kinematic variables. The biggest disagreement is in mass($\pi\pi$) and the absolute value of the pion helicity angle. We therefore plot, in figure 7.8, the ratio in these two dimensions. Table 7.4 tabulates the numerical values with errors. Figure 7.9 shows ϵ(B|A) in our Data . Figure 7.10 shows ϵ(B|A) in Generic MC. The four plots in figure 7.4 are the ratios of plots in figure 7.9 divided by plots in figure 7.10. For any easier comparison, figure 7.11 shows ϵ_{our}Data(B|A)/ϵ_{MC}(B|A) and ϵ_{our}Data(B|A) for $\pi^+\pi^-(\mu^+\mu^-)$ and $\pi^0\pi^0(\mu^+\mu^-)$.

When computing these double ratios we were concerned about correctly modeling 1σ error-bars especially in regions where the yields drop off rapidly. The problem is that both Poisson (and even Binomial errors) behave poorly when a ratio is close to zero or unity. We employ a Bayesian technique [19] whose algorithm is implemented in the Root class TGraphAsymmErrors (we use our own implementation using the gsl [20] and R [21]). The Bayesian prior on the efficiency is set be uniform from 0 to 1 and zero otherwise. We then find the smallest interval in the posterior distribution that contains 68.3% probability. The end result is pair of asymmetric errors on each efficiency calculation. The quoted (asymmetric) errors on the double ratio are the largest possible fluctuations when the efficiencies are moved within their (asymmetric) error-bars. This last step implies that the error calculation is conservative.

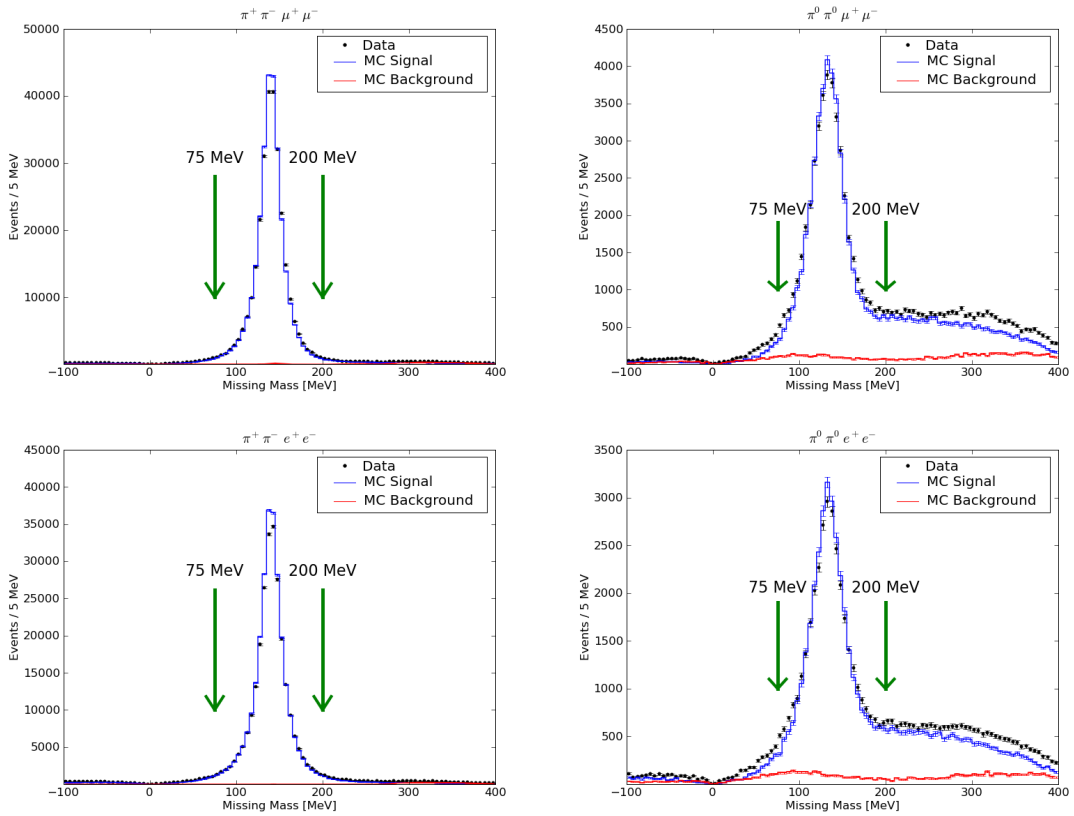

Figure 7.7: The missing mass cut,75MeV $<$ MM $<$ 200MeV. The MC estimated background rates are 0.3% for $\pi^+\pi^-\mu^+\mu^-$, 1.2% for $\pi^0\pi^0\mu^+\mu^-$, 5.3% for $\pi^+\pi^-e^+e^-$, and 5.9% for $\pi^0\pi^0e^+e^-$.

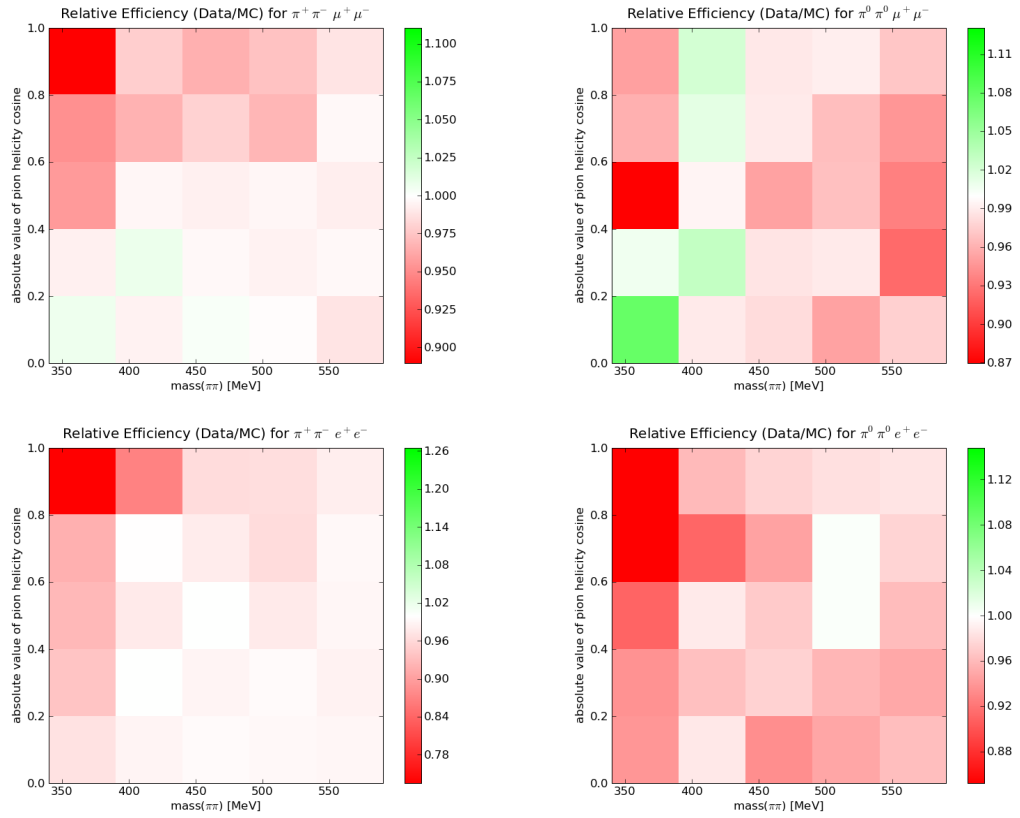

Figure 7.8: Relative Pion Tracking Efficiency, $\frac{\epsilon_o ur\texttt{Data(B|A)}}{\epsilon_{\texttt{MC}}\texttt{(B|A)}}$, for $\pi^+\pi^-\mu^+\mu^-$, $\pi^0\pi^0\mu^+\mu^-$, $\pi^+\pi^-e^+e^-$, and for $\pi^0\pi^0e^+e^-$. See next page for numerical values.

Table 7.4: Relative Pion Tracking Efficiency, $\frac{\epsilon_{our}\mathtt{Data(B|A)}}{\epsilon_{\mathtt{MC}}\mathtt{(B|A)}}$, for $\pi^+\pi^-\mu^+\mu^-$, $\pi^0\pi^0\mu^+\mu^-$, $\pi^+\pi^-e^+e^-$, and for $\pi^0\pi^0e^+e^-$. See previous page for scales.

$\pi^+\pi^-\mu^+\mu^-$

$0.89^{+0.06}_{-0.06}$	$0.98^{+0.03}_{-0.03}$	$0.97^{+0.02}_{-0.02}$	$0.97^{+0.01}_{-0.01}$	$0.99^{+0.00}_{-0.00}$
$0.95^{+0.04}_{-0.04}$	$0.97^{+0.02}_{-0.02}$	$0.98^{+0.01}_{-0.01}$	$0.97^{+0.01}_{-0.01}$	$1.00^{+0.00}_{-0.00}$
$0.96^{+0.02}_{-0.02}$	$1.00^{+0.01}_{-0.01}$	$0.99^{+0.01}_{-0.01}$	$1.00^{+0.01}_{-0.01}$	$0.99^{+0.00}_{-0.00}$
$0.99^{+0.02}_{-0.02}$	$1.01^{+0.01}_{-0.01}$	$1.00^{+0.01}_{-0.01}$	$0.99^{+0.01}_{-0.01}$	$1.00^{+0.00}_{-0.00}$
$1.01^{+0.02}_{-0.02}$	$0.99^{+0.01}_{-0.01}$	$1.00^{+0.01}_{-0.01}$	$1.00^{+0.01}_{-0.01}$	$0.99^{+0.01}_{-0.00}$

$\pi^0\pi^0\mu^+\mu^-$

$0.95^{+0.07}_{-0.07}$	$1.02^{+0.04}_{-0.04}$	$0.99^{+0.03}_{-0.03}$	$0.99^{+0.02}_{-0.02}$	$0.97^{+0.02}_{-0.02}$
$0.96^{+0.07}_{-0.07}$	$1.01^{+0.04}_{-0.04}$	$0.99^{+0.03}_{-0.03}$	$0.97^{+0.02}_{-0.02}$	$0.95^{+0.02}_{-0.02}$
$0.87^{+0.07}_{-0.07}$	$0.99^{+0.04}_{-0.04}$	$0.95^{+0.03}_{-0.03}$	$0.97^{+0.02}_{-0.02}$	$0.94^{+0.02}_{-0.02}$
$1.01^{+0.07}_{-0.07}$	$1.03^{+0.04}_{-0.04}$	$0.99^{+0.03}_{-0.03}$	$0.99^{+0.02}_{-0.02}$	$0.92^{+0.02}_{-0.02}$
$1.08^{+0.08}_{-0.07}$	$0.99^{+0.04}_{-0.04}$	$0.98^{+0.03}_{-0.03}$	$0.95^{+0.02}_{-0.02}$	$0.98^{+0.02}_{-0.02}$

$\pi^+\pi^-e^+e^-$

$0.74^{+0.06}_{-0.06}$	$0.87^{+0.03}_{-0.03}$	$0.96^{+0.02}_{-0.02}$	$0.97^{+0.01}_{-0.01}$	$0.98^{+0.01}_{-0.01}$
$0.92^{+0.04}_{-0.04}$	$1.00^{+0.02}_{-0.02}$	$0.98^{+0.01}_{-0.01}$	$0.96^{+0.01}_{-0.01}$	$0.99^{+0.01}_{-0.01}$
$0.93^{+0.03}_{-0.03}$	$0.98^{+0.02}_{-0.02}$	$1.00^{+0.01}_{-0.01}$	$0.98^{+0.01}_{-0.01}$	$0.99^{+0.01}_{-0.01}$
$0.94^{+0.03}_{-0.03}$	$1.00^{+0.01}_{-0.01}$	$0.99^{+0.01}_{-0.01}$	$0.99^{+0.01}_{-0.01}$	$0.99^{+0.01}_{-0.01}$
$0.97^{+0.03}_{-0.03}$	$0.99^{+0.01}_{-0.01}$	$1.00^{+0.01}_{-0.01}$	$0.99^{+0.01}_{-0.01}$	$0.99^{+0.01}_{-0.01}$

$\pi^0\pi^0e^+e^-$

$0.85^{+0.07}_{-0.07}$	$0.96^{+0.05}_{-0.04}$	$0.97^{+0.03}_{-0.03}$	$0.98^{+0.02}_{-0.02}$	$0.98^{+0.02}_{-0.02}$
$0.85^{+0.08}_{-0.07}$	$0.91^{+0.04}_{-0.04}$	$0.95^{+0.03}_{-0.03}$	$1.00^{+0.02}_{-0.02}$	$0.97^{+0.02}_{-0.02}$
$0.91^{+0.08}_{-0.08}$	$0.99^{+0.05}_{-0.05}$	$0.97^{+0.03}_{-0.03}$	$1.00^{+0.02}_{-0.02}$	$0.96^{+0.02}_{-0.02}$
$0.94^{+0.08}_{-0.08}$	$0.96^{+0.05}_{-0.04}$	$0.97^{+0.03}_{-0.03}$	$0.96^{+0.02}_{-0.02}$	$0.95^{+0.02}_{-0.02}$
$0.94^{+0.08}_{-0.07}$	$0.99^{+0.05}_{-0.05}$	$0.93^{+0.03}_{-0.03}$	$0.95^{+0.02}_{-0.02}$	$0.96^{+0.02}_{-0.02}$

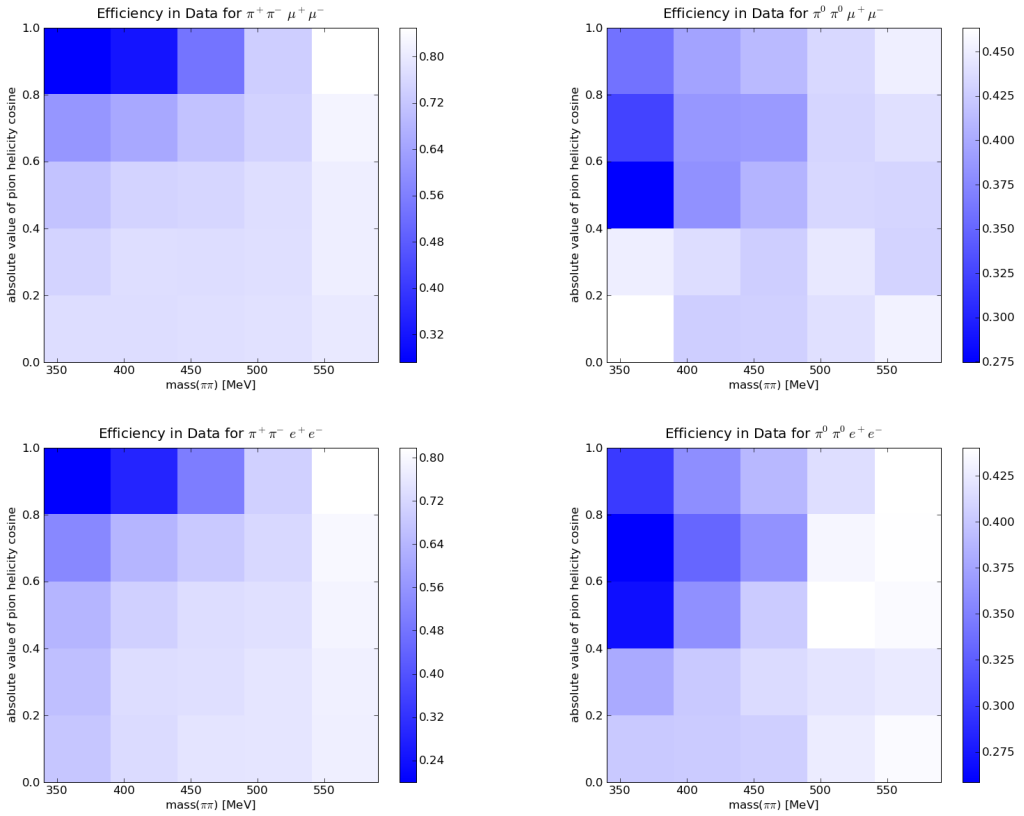

Figure 7.9: Efficiency in our `Data`, ϵ_our`Data`(`B`|`A`), for $\pi^+\pi^-\mu^+\mu^-$, $\pi^0\pi^0\mu^+\mu^-$, $\pi^+\pi^-e^+e^-$, and for $\pi^0\pi^0e^+e^-$. The drop in efficiency for charged transitions (upper left-hand corner for first column plots), is due to curlers. Notice how the neutral transistions do not have a drop in efficiency in these region. This is, of course, because neutral pions do no curl, and is an example of how neutral transition offer an essential check for this analysis.

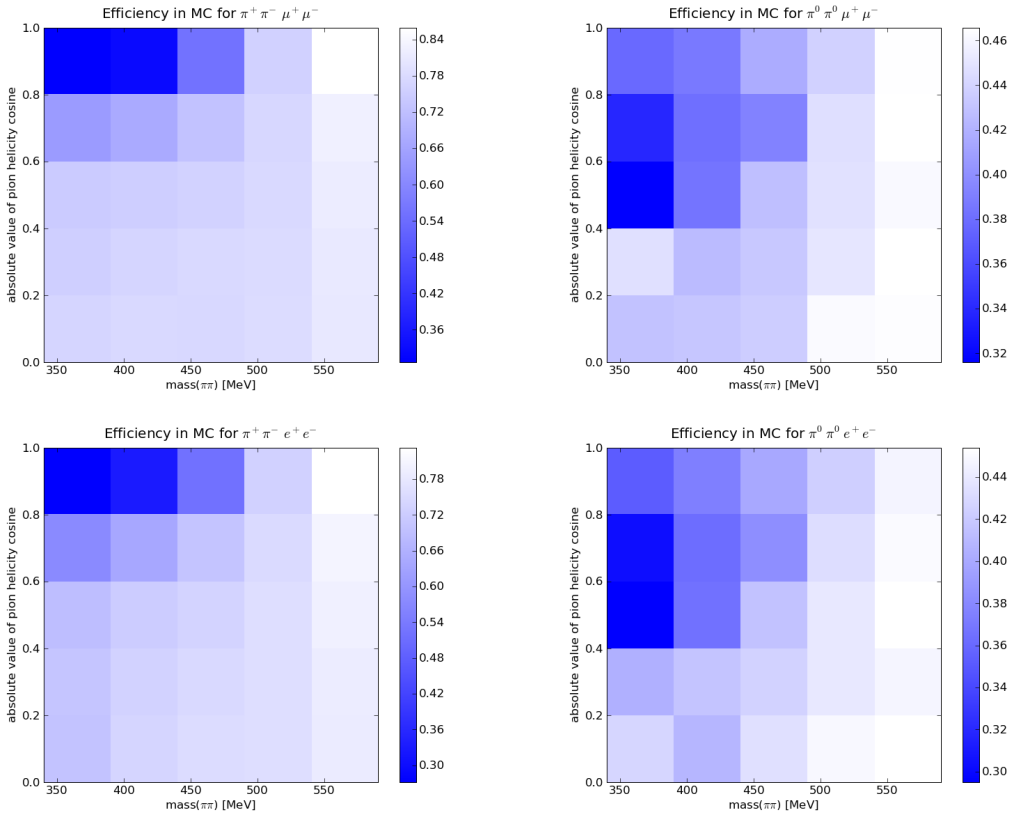

Figure 7.10: Efficiency in `Generic MC`, $\epsilon_{\mathtt{MC}}(\mathtt{B}|\mathtt{A})$, for $\pi^+\pi^-\mu^+\mu^-$, $\pi^0\pi^0\mu^+\mu^-$, $\pi^+\pi^-e^+e^-$, and for $\pi^0\pi^0e^+e^-$.

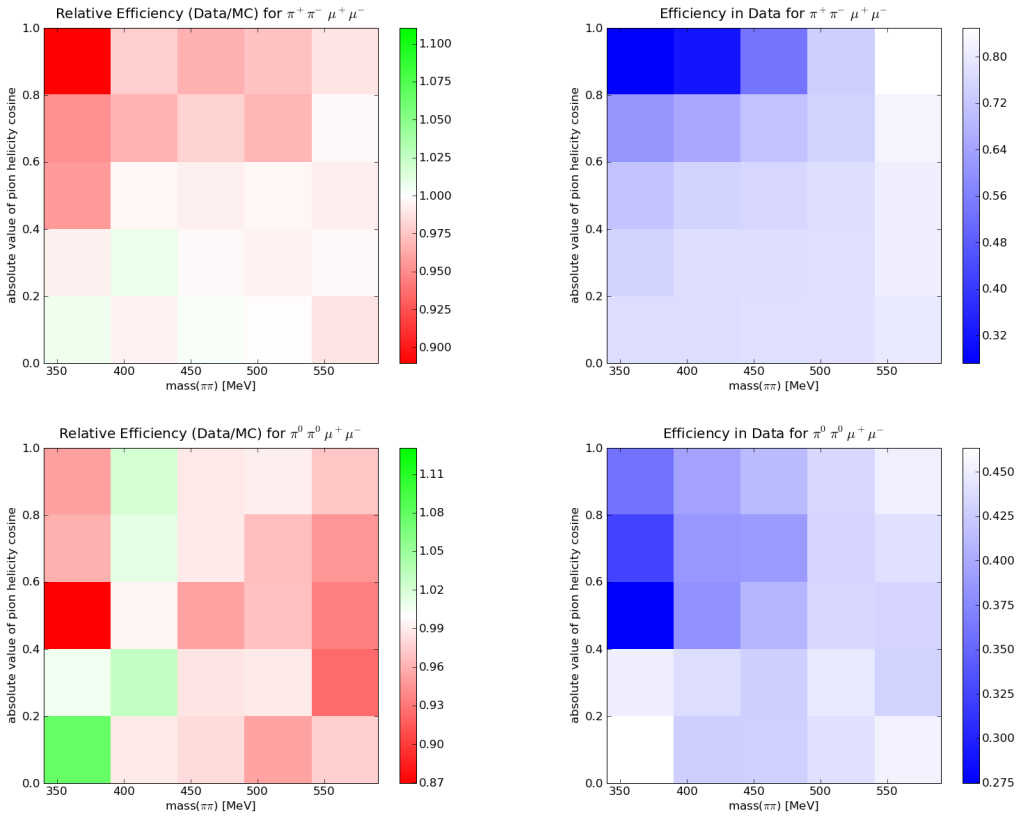

Figure 7.11: Relative Efficiency, $\frac{\epsilon_o ur\texttt{Data(B|A)}}{\epsilon_{\texttt{MC}}\texttt{(B|A)}}$, and Efficiency in `Data`, $\epsilon_o ur\texttt{Data(B|A)}$, for $\pi^+\pi^-\mu^+\mu^-$ (first row) and $\pi^0\pi^0\mu^+\mu^-$ (second row).

With the correction factors in table 7.4, we reweight PhaseSpaceMC. This means that for each event, we compute the dipion mass and pion helicity angle and set the event-weight equal to the corresponding number in table 7.4. Next, we accept-reject the entire PhaseSpaceMC in order to properly weight each event. We then recalculate normalization coefficients and refit our Data . The shifts for $\pi^+\pi^-(\ell^+\ell^-)$ and $\pi^0\pi^0(\ell^+\ell^-)$ are estimates for systematic error.

The results for the Kappa Model are,

$$\begin{aligned}
\kappa_{\pi^+\pi^-(\ell^+\ell^-)} &= 0.2740 \pm 0.0006_{\texttt{stat}} \pm 0.0006_{\texttt{reso}} \pm 0.0002_{\texttt{cuts}} \pm \mathbf{0.0007}_{\texttt{eff}} \\
\kappa_{\pi^0\pi^0(\ell^+\ell^-)} &= 0.2757 \pm 0.0015_{\texttt{stat}} \pm 0.0025_{\texttt{reso}} \pm 0.0019_{\texttt{cuts}} \pm \mathbf{0.0015}_{\texttt{eff}} \quad . \qquad (7.7)
\end{aligned}$$

CHAPTER 8

RESULTS

The final numbers for the Kappa Model are,

$$\kappa_{\pi^+\pi^-(\ell^+\ell^-)} = 0.2740 \pm 0.0006_{\mathtt{stat}} \pm 0.0009_{\mathtt{sys}} \tag{8.1}$$

$$\kappa_{\pi^0\pi^0(\ell^+\ell^-)} = 0.2757 \pm 0.0015_{\mathtt{stat}} \pm 0.0035_{\mathtt{sys}} \quad . \tag{8.2}$$

When comparing to the BES result [2], $\kappa_{\mathtt{BES}} = 0.183 \pm 0.002 \pm 0.003$, it is important to add a few qualifications. When fitting for κ, the BES analysis used a different version of the Kappa Model. BES followed [24], which makes non-relativistic approximations in the writing of covariant terms and explicitly sets $m_\pi^2 = 0$ in first term of the Kappa Model (by writing q^2 instead of $q^2 + m_\pi^2$). These differences are only qualifications because they do not explain why our Data provides a much larger value of κ. For one, the non-relativistic simplifications should be excellent approximations. And secondly, we have fit a modified Kappa Model where this m_π^2 term is removed and find a value of $\kappa = 0.23$ which is statistically inconsistent with our standard value of $\kappa = 0.27$ and the BES value of $\kappa = 0.18$.

The fit results for other models are presented in the following tables. Table 8.1 is for the ABCλ Model. Compare this to what the fitted κ value of 0.2740 would predict (from equation 4.8),

$$\mathcal{B}/\mathcal{A} = 2.069$$

$$C/\mathcal{A} = 0$$

$$\lambda/\mathcal{A} = 3.776 \quad . \tag{8.3}$$

The likelihood ratio test estimates an infinitesimal `p-value` for the `ABC`λ Model fitting for a fake, non-zero value of C.

Table 8.1: Fit Results for the `ABC`λ Model.

`ABC`λ `Model`								
	`optimal values`	`statistical correlation`			`systematic correlation`		
$\pi^+\pi^-$	$\mathcal{B}/\mathcal{A} = -0.878 \pm 0.004 \pm 0.027$	+1.000	+0.424	−0.600	+1.000	+0.104	−0.985
	$C/\mathcal{A} = -0.051 \pm 0.003 \pm 0.005$		+1.000	+0.017		+1.000	−0.017
	$\lambda/\mathcal{A} = +0.564 \pm 0.010 \pm 0.099$			+1.000			+1.000
$\pi^0\pi^0$	$\mathcal{B}/\mathcal{A} = -0.853 \pm 0.010 \pm 0.056$	+1.000	+0.453	−0.586	+1.000	+0.292	−0.945
	$C/\mathcal{A} = -0.036 \pm 0.008 \pm 0.010$		+1.000	+0.041		+1.000	−0.145
	$\lambda/\mathcal{A} = +0.362 \pm 0.025 \pm 0.218$			+1.000			+1.000

Table 8.2 is for the Voloshin Model. The likelihood ratio test estimates an infinitesimal `p-value` for the fitted $\chi_m \neq 0$ and $\chi_2 \neq 0$. On the other hand, zeros value of χ_m and χ_2 are within the statistical and systematic error bars.

Table 8.2: Fitted results for the `Voloshin` Model.

`Voloshin Model`								
	`optimal values`	`statistical correlation`			`systematic correlation`		
$\pi^+\pi^-$	$\kappa = +0.286 \pm 0.004 \pm 0.019$	+1.000	−0.987	+0.904	+1.000	−0.999	+0.993
	$\chi_m = -0.024 \pm 0.008 \pm 0.033$		+1.000	−0.902		+1.000	−0.993
	$\chi_2 = -0.031 \pm 0.011 \pm 0.050$			+1.000			+1.000
$\pi^0\pi^0$	$\kappa = +0.279 \pm 0.012 \pm 0.018$	+1.000	−0.992	+0.943	+1.000	−0.974	+0.930
	$\chi_m = -0.008 \pm 0.021 \pm 0.034$		+1.000	−0.942		+1.000	−0.908
	$\chi_2 = -0.020 \pm 0.032 \pm 0.054$			+1.000			+1.000

Table 8.3 is for the `KappaFSI` Model. Figure 8.1 shows the fitted phase shift in comparison with the expected shape (the statistical and systematic errors are negligible in this figure). Notice how the phase looks wrong! The likelihood ratio test estimates an infinitesimal `p-value` for seeing a fake phase shift.

Table 8.3: Fit Results for the KappaFSI Model. The units for a and b are degrees.

KappaFSI Model								
	optimal values	statistical correlation			systematic correlation		
$\pi^+\pi^-$	$\kappa = +0.283 \pm 0.001 \pm 0.001$	+1.000	−0.004	+0.010	+1.000	+0.337	+0.481
	$a = +58.217 \pm 0.012 \pm 0.687$		+1.000	−0.031		+1.000	+0.014
	$b = +2.459 \pm 0.009 \pm 2.180$			+1.000			+1.000
$\pi^0\pi^0$	$\kappa = +0.284 \pm 0.002 \pm 0.004$	+1.000	+0.001	−0.002	+1.000	+0.250	+0.190
	$a = +54.044 \pm 0.027 \pm 2.132$		+1.000	−0.078		+1.000	+0.071
	$b = -6.917 \pm 0.029 \pm 7.332$			+1.000			+1.000

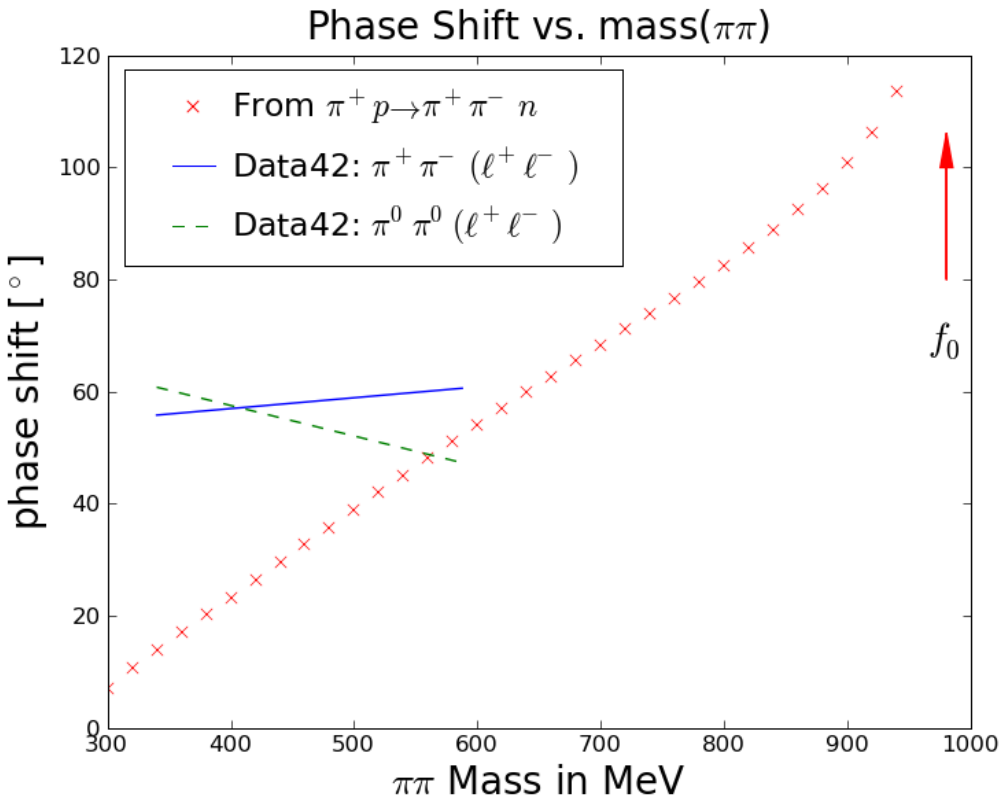

Figure 8.1: Fit Results for the KappaFSI Model in comparison with the expected shape.

Table 8.4 is for the $\mathcal{D}/\mathcal{S}$ ratio fits in mass($\pi\pi$) bins. Figure 8.2 plots the same results.

Table 8.5 is for the Quasi Model-Independent (QMI) Parameterization. Recall (see section 4.7) how the QMI model assumes,

$$\mathcal{M} = \mathcal{S}(q)\epsilon' \cdot \epsilon + \mathcal{D}(q)d^2_{00}(\cos\theta)\epsilon' \cdot \epsilon, \tag{8.4}$$

Table 8.4: Fit Results for magnitude of the $\mathcal{D}/\mathcal{S}$ ratio in mass($\pi\pi$) Bins.

$\mathcal{D}/\mathcal{S}$ Amplitude-Ratio Magnitudes		
Bins [MeV]	$\pi^+\pi^-$ Ratio	$\pi^0\pi^0$ Ratio
340-365	0.274 ± 0.022 ± 0.028	0.236 ± 0.042 ± 0.064
365-390	0.189 ± 0.015 ± 0.021	0.262 ± 0.027 ± 0.056
390-415	0.144 ± 0.010 ± 0.016	0.158 ± 0.019 ± 0.038
415-440	0.110 ± 0.007 ± 0.009	0.128 ± 0.014 ± 0.032
440-465	0.080 ± 0.005 ± 0.008	0.093 ± 0.011 ± 0.021
465-490	0.059 ± 0.004 ± 0.008	0.073 ± 0.009 ± 0.019
490-510	0.051 ± 0.004 ± 0.006	0.045 ± 0.008 ± 0.016
515-540	0.032 ± 0.003 ± 0.004	0.044 ± 0.008 ± 0.012
540-565	0.019 ± 0.003 ± 0.005	0.023 ± 0.007 ± 0.014
565-590	0.010 ± 0.004 ± 0.006	0.013 ± 0.009 ± 0.019

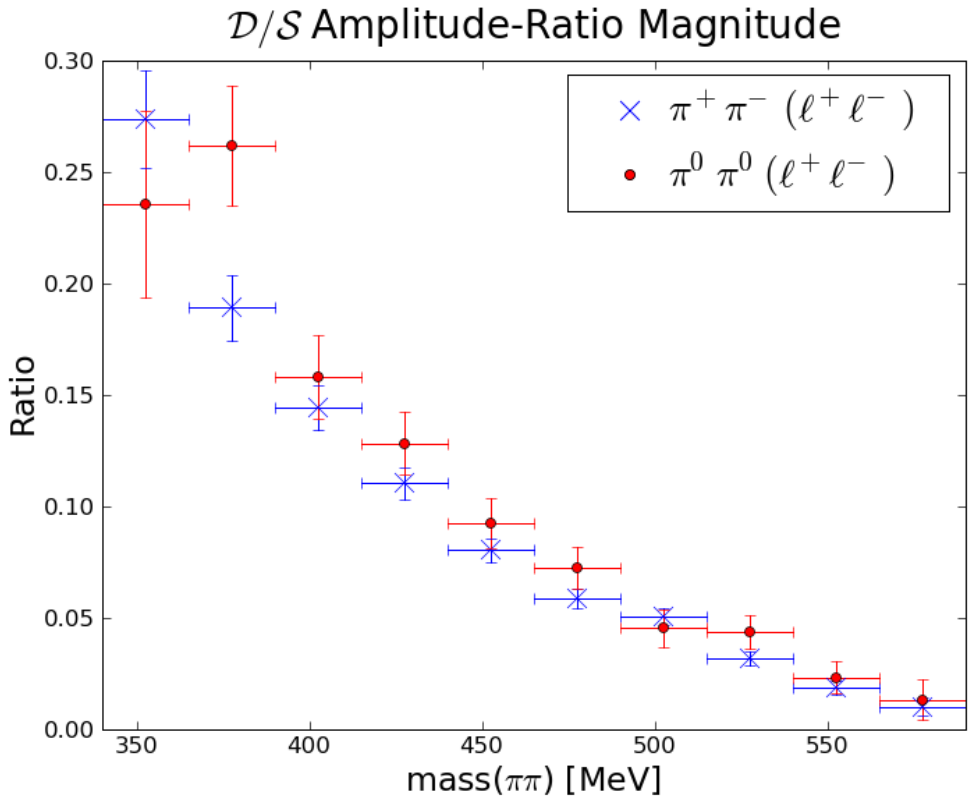

Figure 8.2: The Binned Fits for the magnitude of the $\mathcal{D}/\mathcal{S}$ amplitude-ratio

and,

$$\mathcal{S}(x) = 0.5 + s_1 x + s_2 x^2 + s_3 x^3 + s_4 x^4 \quad (8.5)$$

$$\mathcal{D}(x) = d_0 + d_1 x + d_2 x^2 \quad . \quad (8.6)$$

Figure 8.3 and figure 8.4 show the QMI fit results for $\pi^+\pi^-(\ell^+\ell^-)$ and $\pi^0\pi^0(\ell^+\ell^-)$. Figure 8.5 shows an estimate for the 1σ errors (combined statistical and systematic) on the $\pi^+\pi^-(\ell^+\ell^-)$ fit result. The plot is generated by sampling uniformly the space inside a 1σ-fluctuation as defined by the combined coviariance matrices. Each sample is then plotted. The result is only an approximate 1σ error region because information on the density of plotted lines is not displayed in the plot.

Figure 8.6 is the most important plot. It shows the Kappa, VVPIPI and QMI Models for $\pi^+\pi^-(\ell^+\ell^-)$. The plot reveals precisely how the Kappa Model fails to properly model $\mathcal{S}(q)$ and $\mathcal{D}(q)$.

Table 8.5: Fit Results for the Quasi Model-Independent Parameterization.

A Quasi Model-Independent Parameterization								
	optimal values	combined correlation (statistical and systematic)						
$\pi^+\pi^-$	$s_1 = +0.449 \pm 0.002 \pm 0.004$	+1.000	−0.343	−0.953	+0.006	+0.551	+0.140	−0.682
	$s_2 = +0.024 \pm 0.004 \pm 0.006$		+1.000	+0.483	−0.836	−0.280	+0.031	+0.357
	$s_3 = -0.026 \pm 0.003 \pm 0.007$			+1.000	−0.102	−0.569	−0.093	+0.692
	$s_4 = -0.005 \pm 0.004 \pm 0.005$				+1.000	+0.060	+0.025	−0.084
	$d_0 = +0.036 \pm 0.001 \pm 0.002$					+1.000	+0.195	−0.871
	$d_1 = -0.017 \pm 0.002 \pm 0.002$						+1.000	−0.252
	$d_2 = -0.014 \pm 0.003 \pm 0.008$							+1.000
$\pi^0\pi^0$	$s_1 = +0.451 \pm 0.004 \pm 0.006$	+1.000	+0.035	−0.847	+0.043	+0.052	−0.235	−0.013
	$s_2 = +0.029 \pm 0.009 \pm 0.015$		+1.000	+0.173	−0.953	−0.011	−0.114	+0.349
	$s_3 = -0.032 \pm 0.006 \pm 0.011$			+1.000	−0.203	−0.035	+0.160	+0.070
	$s_4 = -0.007 \pm 0.010 \pm 0.023$				+1.000	−0.032	+0.193	−0.401
	$d_0 = +0.043 \pm 0.003 \pm 0.004$					+1.000	−0.277	−0.565
	$d_1 = -0.018 \pm 0.003 \pm 0.006$						+1.000	−0.084
	$d_2 = -0.021 \pm 0.006 \pm 0.010$							+1.000

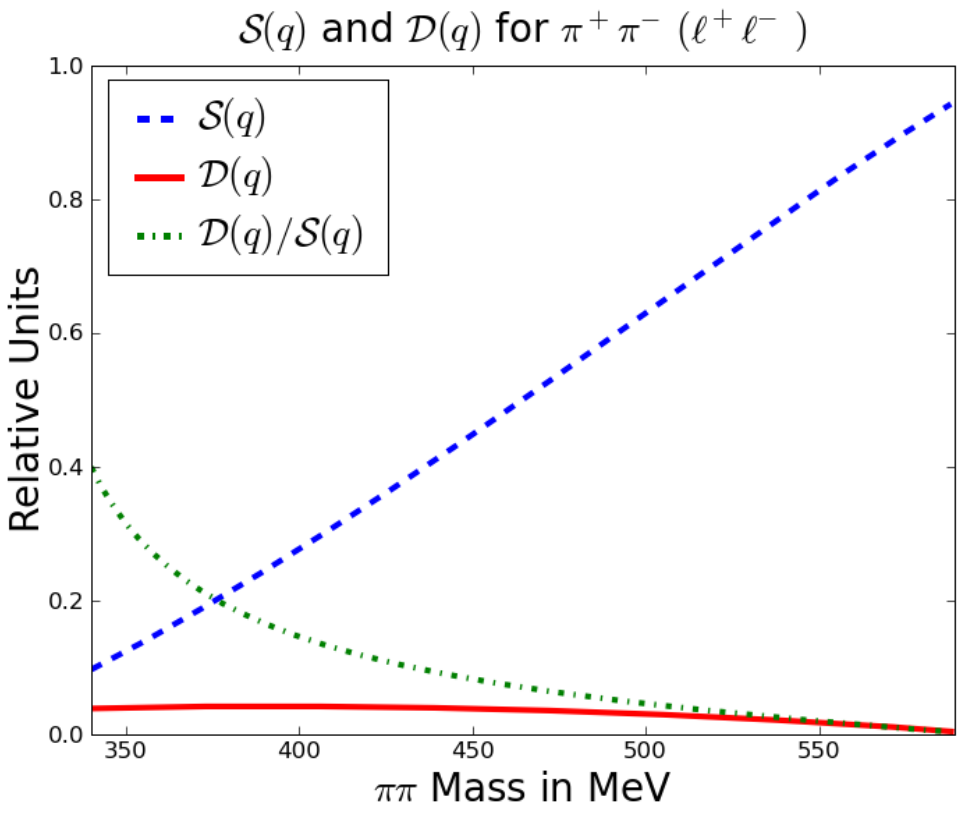

Figure 8.3: Fit Results for the `QMI` Model in the $\pi^+\pi^-(\ell^+\ell^-)$ channel.

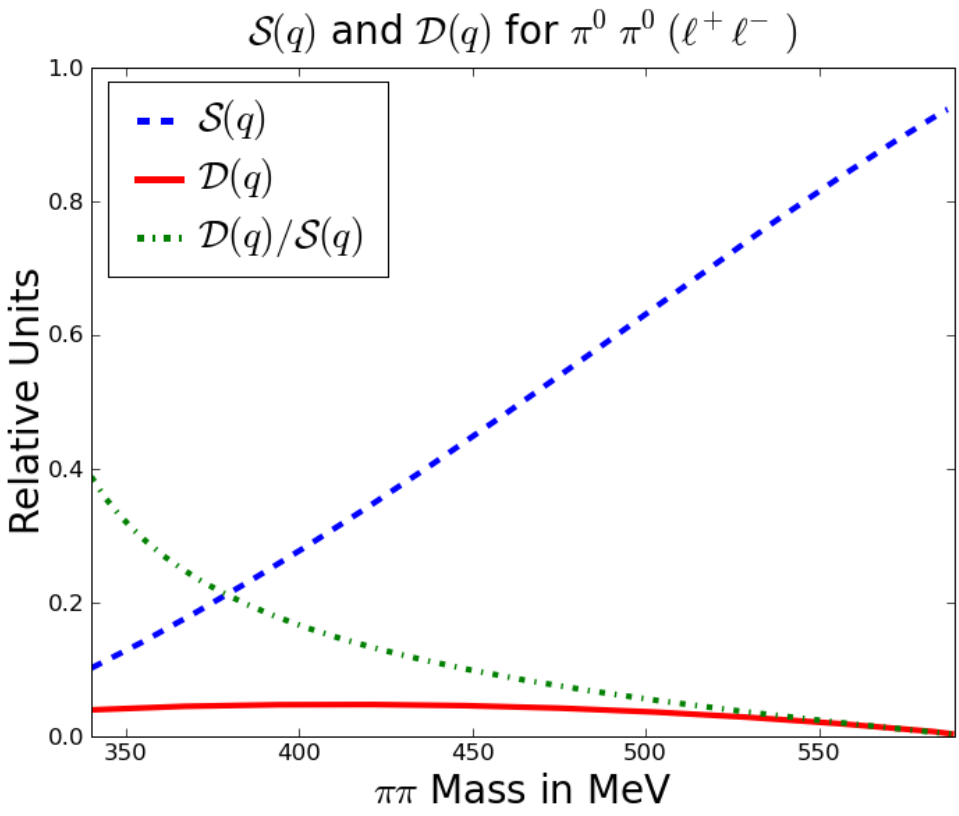

Figure 8.4: Fit Results for the `QMI` Model in the $\pi^0\pi^0(\ell^+\ell^-)$ channel.

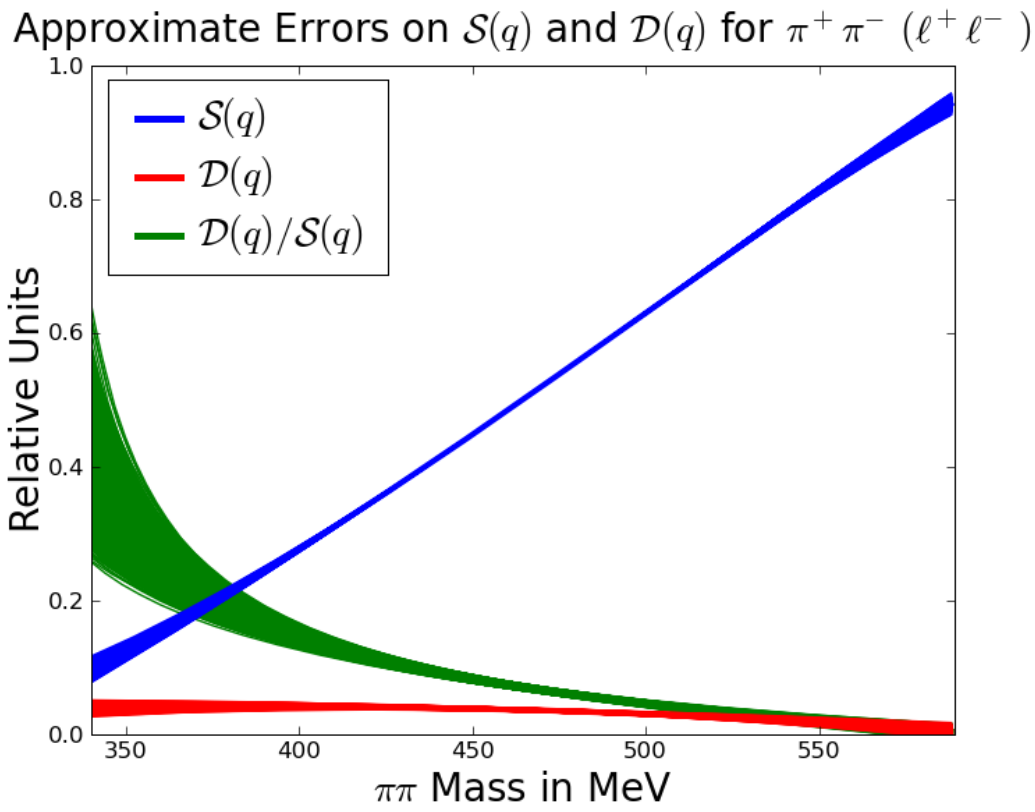

Figure 8.5: Statistical and systematic "error fluctuations" for the `QMI` Model fit results in $\pi^+\pi^-(\ell^+\ell^-)$

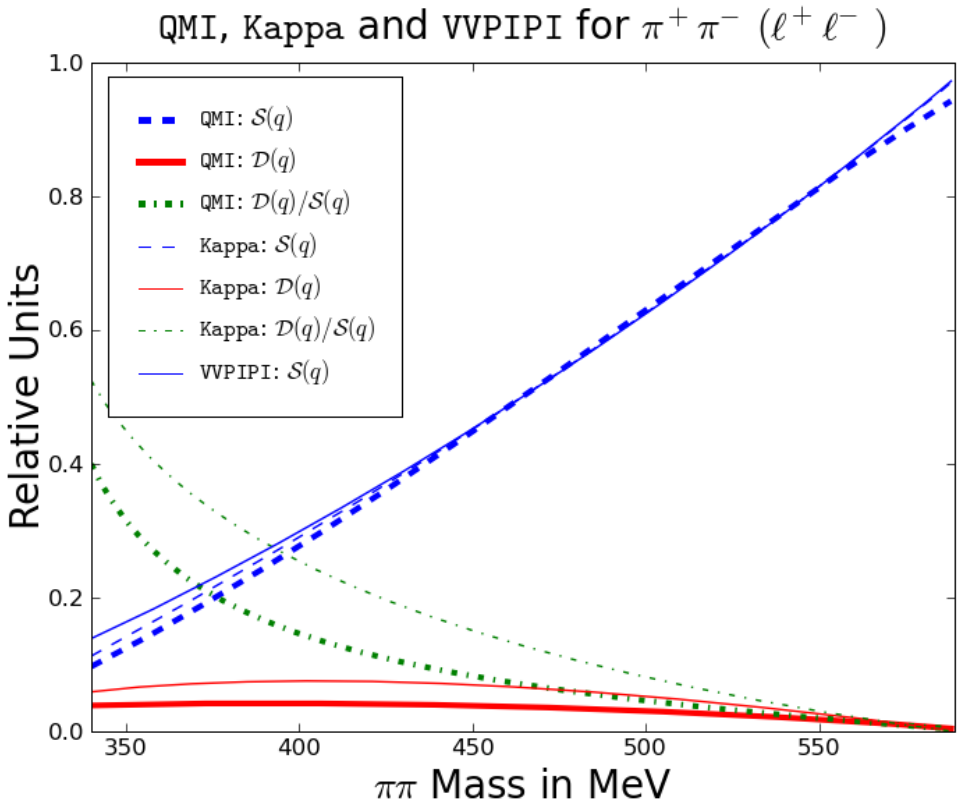

Figure 8.6: A comparison of the Kappa, VVPIPI and QMI Models for $\pi^+\pi^-(\ell^+\ell^-)$.

8.1 Projections

In order to find the optimal model, we compute χ^2 values of projected histograms. For each model, we take the associated pdf at the optimal parameters and use it to reweight `PhaseSpaceMC`. The result is a set of pseudo-datasets that look like they were sampled from the various models. We then histogram these datasets in important kinematic variables. We also put data on these histograms. We can then compute χ^2 values for the agreement between data and the reweighted `PhaseSpaceMC`. We use Pearson's χ^2, with an inflated error to take into account statistical uncertainty in the MC shape.

Table 8.6: $\chi^2/d.o.f.$ values for the models.

	$\chi^2/d.o.f.$ values							
	$\pi^+\pi^-$				$\pi^0\pi^0$			
	25 bins of $\texttt{mass}(\pi^+\pi^-)$		25 bins of $\cos(\theta_{\texttt{helicity}})$		20 bins of $\texttt{mass}(\pi^0\pi^0)$		10 bins of $\lvert\cos(\theta_{\texttt{helicity}})\rvert$	
`models`	$\mu^+\mu^-$	e^+e^-	$\mu^+\mu^-$	e^+e^-	$\mu^+\mu^-$	e^+e^-	$\mu^+\mu^-$	e^+e^-
`VVPIPI`	39.4	33.5	11.9	13.0	13.7	17.3	16.0	16.0
`Kappa`	9.3	6.8	6.1	5.8	2.9	5.5	6.1	5.7
`KappaFSI`	6.3	4.7	0.9	1.3	3.0	3.5	1.2	1.8
`ABC`λ	8.4	7.1	0.9	1.2	3.8	3.8	1.4	1.9
`Voloshin`	8.9	6.5	5.2	5.2	2.8	5.4	5.3	5.5
QMI	**1.2**	**1.3**	**0.7**	**1.3**	**1.5**	**1.9**	**1.2**	**1.9**

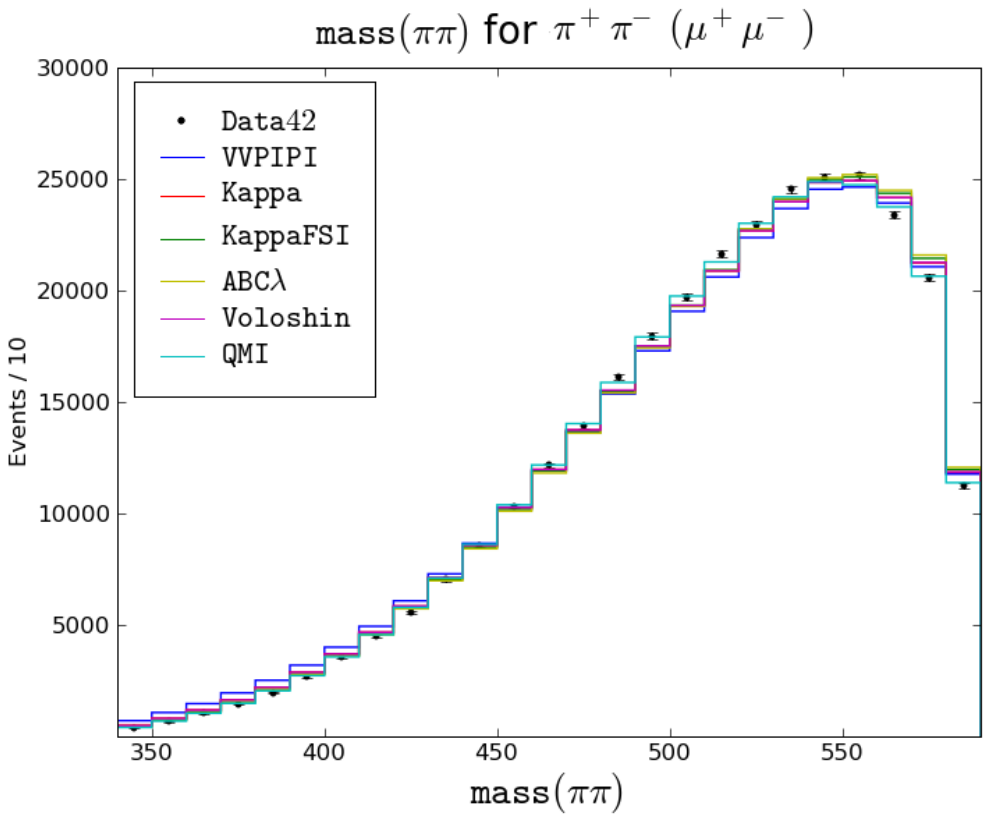

Figure 8.7: mass($\pi\pi$) for all models in ($\pi^+\pi^-(\mu^+\mu^-)$).

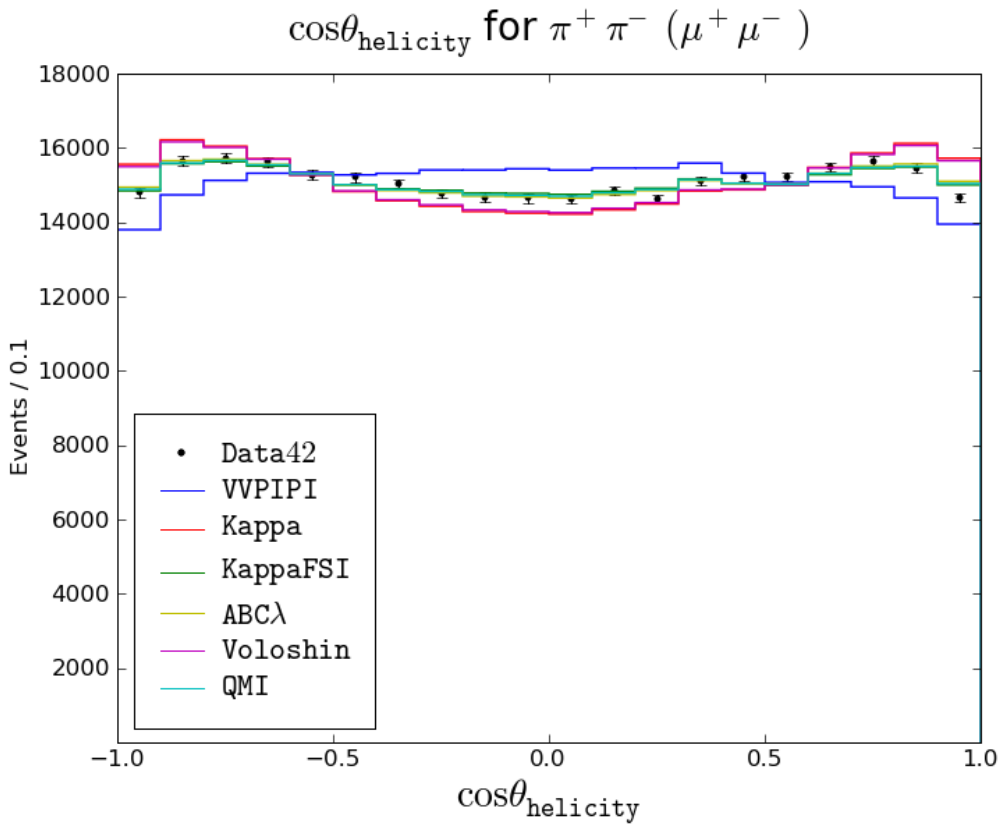

Figure 8.8: Pion Helicity Angle for all models in ($\pi^+\pi^-(\mu^+\mu^-)$).

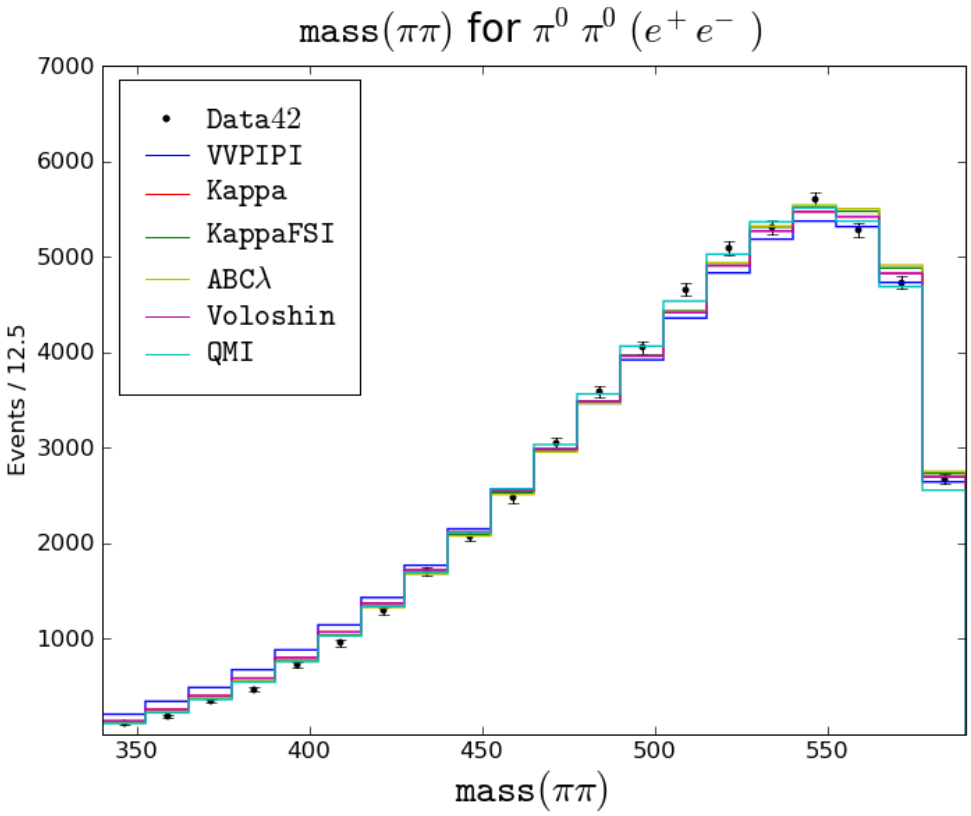

Figure 8.9: mass($\pi\pi$) for all models in ($\pi^0\pi^0(e^+e^-)$).

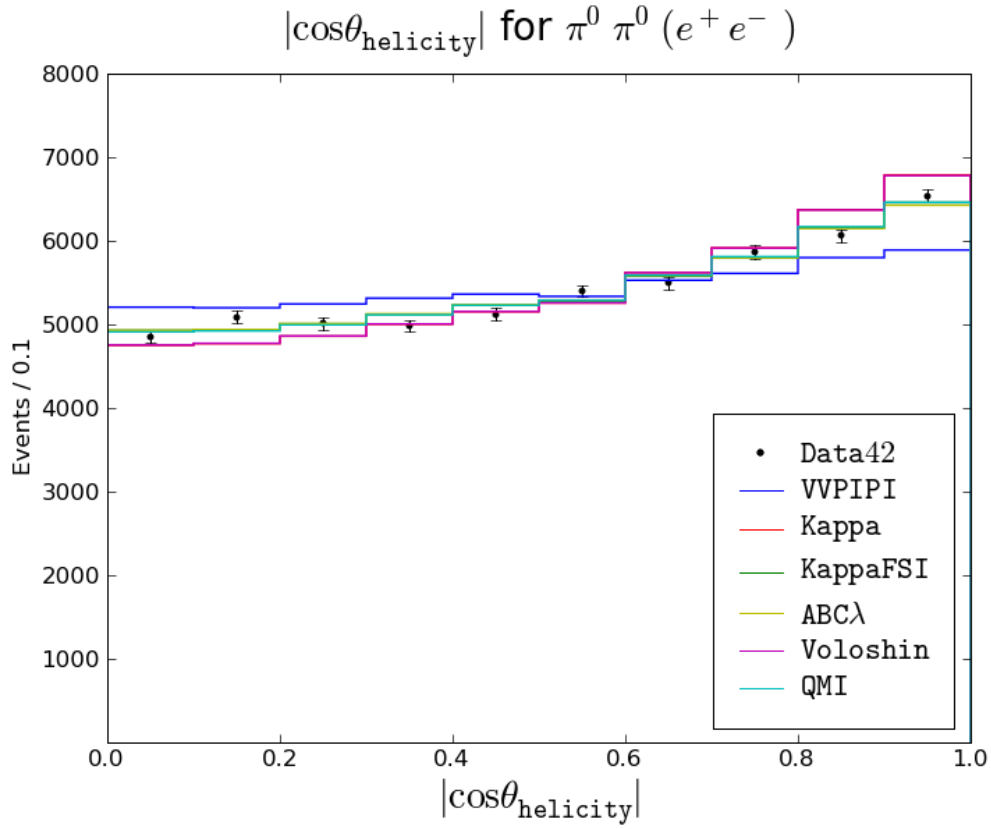

Figure 8.10: Pion Helicity Angle for all models in ($\pi^0\pi^0(e^+e^-)$).

In order to protect against overfitting, we swap the fit results for muons and electrons. For example, the $\pi^+\pi^-(\mu^+\mu^-)$ channel χ^2 compares our `Data` $\pi^+\pi^-(\mu^+\mu^-)$ with `PhaseSpaceMC` $\pi^+\pi^-(\mu^+\mu^-)$ reweighted with the fit results of $\pi^+\pi^-(e^+e^-)$.

Table 8.6 shows the $\chi^2/d.o.f.$ values for the models. The `QMI` Model is the only null hypothesis that cannot be rejected.

CHAPTER 9

CONCLUSIONS

We have three conclusions:

1. The `Kappa` Model has an optimal parameter that is statistically different from the BES result but does not pass χ^2 tests (the fit quality is poor).
2. Higher order theoretical corrections, which motivate the `KappaFSI`, `Voloshin` and `ABC`λ Models, do not describe the discrepency between our `Data` and the `Kappa` Model.
3. We offer a quasi-model independent paramatrization (`QMI`) that describes our `Data` . This model was partially motivated by a binned fit for the $\mathcal{D}/\mathcal{S}$ amplitude ratio that was only successfull at extracting the magnitude of the complex ratio.

The most important plot is in figure 8.6 on page 98. The plot shows how the `Kappa` Model fails to properly describe our `Data` .

APPENDIX

The Orbital Angular Momentum Spin-2 Tensor

Following Filippini, Fontana and Rotondi [22], we now derive the $l_{\mu\nu}$ tensor. We seek a covariant description of the $\pi\pi$ system having $J^{PC} = 2^{++}$.

For motivation, write a generic 3×3 matrix A_{ij} as,

$$A_{ij} = \overbrace{\underbrace{A_{kk}\delta_{ij}}_{\texttt{trace}}}^{\texttt{1 component}} + \overbrace{\underbrace{\frac{1}{2}\left(A_{ij} - A_{ji}\right)}_{\texttt{anti-symmetric}}}^{\texttt{3 components}} + \overbrace{\underbrace{\frac{1}{2}\left(A_{ij} + A_{ji}\right) - A_{kk}\delta_{ij}}_{\texttt{symmetric, traceless}}}^{\texttt{5 components}}. \tag{9.1}$$

and recognize the spin-0, spin-1 and spin-2 states. The first term on the right is the trace $\sum_k A_{kk}$ (with implied summation) multiplied by the unit matrix δ_{ij}. This decomposition suggests a procedure for constructing spin-2 objects. Suppose you want to construct a spin-2 object out of two regular 3-vectors, each of which is spin-1. You would form their direct product, symmetrize the result to remove spin-1 and subtract off the trace to remove spin-0. When dealing with relativistic systems (4×4 matrices), the procedure is the same except one has to identify the frame in which the spin is defined. For the $\pi\pi$ system, as required by J in $J^{PC} = 2^{++}$, the spin is defined in the $\pi\pi$ rest frame. In general, when in the frame where spin is defined, the time-energy components of spin tensors are always zero. This is a reflection of the fact that spin is a rotational property. The space-like nature of spin tensors is covariantly expressed through orthogonality relations, as will be shown below.

We label the fourmomenta in the $\pi^+\pi^-$ system as q_1 for π^+ and q_2 for π^-. For $\pi^0\pi^0$, since the distinction between q_1 and q_2 will not matter, we adopt an arbitrary convention by letting q_1 denote the first π^0 selected during event selection (see section 5.2). Introduce a change of variables,

$$q^\mu = q_1^\mu + q_2^\mu \tag{9.2}$$

$$r^\mu = q_1^\mu - q_2^\mu, \tag{9.3}$$

where q^μ is the momentum of the dipion system and r^μ is the "break-up" momentum. The spin-1 fourvector, call it S^μ, should look something like r^μ, as it should represent how the pions are moving in their rest frame. Then adding the condition $S \cdot q = 0$ will ensure that S^μ has no time components in the dipion rest frame. Additionally, add $S^2 = -1$ for normalization. With these conditions, S^μ takes the form,

$$S^\mu = r^\mu - (q \cdot r)q^\mu/q^2. \tag{9.4}$$

The next step is two add the two spin-1 fourvectors together via the direct product $(S^\mu S^\nu)$ and add a correction piece to kill the spin-0 and spin-1 components. Also, an orthogonality condition,

$$q_\mu l^{\mu\nu} = 0, \tag{9.5}$$

will ensure that $l^{\mu\nu}$ only has spacial components in the dipion rest frame. The correct form of this symmetric, traceless, space-like object is,

$$l^{\mu\nu} = S^\mu S^\nu - \frac{1}{3}S^2(g^{\mu\nu} - \frac{q^\mu q^\nu}{q^2}). \tag{9.6}$$

When the masses of both particles are the same, which is the case here, the above expression simplifies because,

$$\begin{aligned} q \cdot r &= (q_1 + q_2) \cdot (q_1 - q_2) \\ &= q_1^2 - q_2^2 \\ &= m_\pi^2 - m_\pi^2 \\ &= 0. \end{aligned} \tag{9.7}$$

The final result is,

$$l^{\mu\nu} = r^\mu r^\nu + \frac{1}{3}\left(1 - \frac{4m_\pi^2}{q^2}\right)\left(q^2 g^{\mu\nu} - q^\mu q^\nu\right). \tag{9.8}$$

Now this is all well and good, but what does it mean? In order to see, go to the rest frame of the dipion system where, implicitly defining $\vec{p}$,

$$q_1^\mu = (E, \quad \vec{p}) \tag{9.9}$$

$$q_2^\mu = (E, -\vec{p}), \tag{9.10}$$

which means that

$$q^\mu = (2E, \quad \vec{0}) \tag{9.11}$$

$$r^\mu = (\quad 0, 2\vec{p}). \tag{9.12}$$

Plugging these into (9.8) gives,

$$l^{\mu\nu} = 4\begin{bmatrix} 0 & 0 & 0 & 0 \\ 0 & p_x^2 - |\vec{p}|^2/3 & p_x p_y & p_x p_z \\ 0 & p_y p_x & p_y^2 - |\vec{p}|^2/3 & p_y p_z \\ 0 & p_z p_x & p_z p_y & p_z^2 - |\vec{p}|^2/3 \end{bmatrix}. \tag{9.13}$$

Recovering the Wigner-D functions develops intuition. The idea is to start with *rest-frame* polarization fourvectors as natural extension of polarization 3-vectors,

$$\epsilon_{\pm}^{\mu} = (0, \hat{\epsilon}_{\pm}) \text{ where } \hat{\epsilon}_{\pm} = \mp(\hat{x} \pm i\hat{y})/\sqrt{2} \tag{9.14}$$

$$\epsilon_{0}^{\mu} = (0, \hat{\epsilon}_{0}) \text{ where } \hat{\epsilon}_{0} = \hat{z} \tag{9.15}$$

evaluate the matrix elements,

$$\epsilon_{+,\mu} l^{\mu\nu} \epsilon^{*}_{+,\nu} = -2\left(\frac{|\vec{p}|^2}{3} - p_z^2\right) \tag{9.16}$$

$$\epsilon_{+,\mu} l^{\mu\nu} \epsilon^{*}_{0,\nu} = \frac{4}{\sqrt{2}}(p_x + ip_y)p_z \tag{9.17}$$

$$\epsilon_{+,\mu} l^{\mu\nu} \epsilon^{*}_{-,\nu} = 2\left(p_x + ip_y\right)^2 \tag{9.18}$$

and translate the result into the familiar form,

$$
\begin{aligned}
\epsilon_{+,\mu} l^{\mu\nu} \epsilon^{*}_{+,\nu} &= \frac{4|\vec{p}|^2\sqrt{10}}{3} \times \underbrace{\frac{1}{\sqrt{10}}}_{\langle 11|20;11\rangle} \times \underbrace{\left(\frac{3}{2}\cos^2\theta - \frac{1}{2}\right)}_{D^{2*}_{0,0}} \\
\epsilon_{+,\mu} l^{\mu\nu} \epsilon^{*}_{0,\nu} &= \frac{4|\vec{p}|^2\sqrt{10}}{3} \times \underbrace{-\sqrt{\frac{3}{10}}}_{\langle 11|21;10\rangle} \times \underbrace{-\sqrt{\frac{3}{2}} e^{i\phi}\sin\theta\cos\theta}_{D^{2*}_{1,0}} \\
\epsilon_{+,\mu} l^{\mu\nu} \epsilon^{*}_{-,\nu} &= \frac{4|\vec{p}|^2\sqrt{10}}{3} \times \underbrace{\sqrt{\frac{3}{5}}}_{\langle 21|22;1-1\rangle} \times \underbrace{\frac{\sqrt{6}}{4} e^{-2i\phi}\sin^2\theta}_{D^{2*}_{2,2}}.
\end{aligned}
\tag{9.19}
$$

Returning to the relativistic situation, we want to couple $l_{\mu\nu}$ in the simplest possible way to the rest of $\psi(2S) \to \pi\pi J/\psi$. By "simple," we mean without coupling to the spins of the vectors. The jargon here is $\Delta m_{\texttt{spin}} = 0$. Because of the orthogonality relation ($q_\mu l^{\mu\nu} = 0$, eq. 9.5), there is really only one option,

$$
\frac{P'_\mu P'_\nu}{P'^2}\, l^{\mu\nu}. \tag{9.20}
$$

After supplementing $q^\mu = (2E, \vec{0})$ and $r^\mu = (0, 2\vec{p})$, equations 9.11 and 9.12, with $P'^\mu = (E', \vec{p'})$, a dipion rest-frame version of the $\psi(2S)$ fourmomenta, we evaluate eq. 9.20 and get,

$$
\frac{P'^\mu P'^\nu}{P'^2} l_{\mu\nu} = \underbrace{\frac{8}{3}\,\frac{p'^2\; p^2}{P'^2}}_{g(p',\,p)}\; d^2_{00}(\cos\theta) \quad \text{where} \quad d^2_{00}(\cos\theta) = \frac{3}{2}\cos^2\theta - \frac{1}{2} \quad . \tag{9.21}
$$

The proportionality factor, $g(p', p)$, depends on both p', the 3-momentum magnitude of the $\psi(2S)$, and p, the 3-momentum magnitude of the first pion. These two 3-momenta are evaluated in the dipion rest frame. If the z-axis is aligned with the momentum of the

$\psi(2S)$, this result (eq. 9.21) follows directly from the matrix in eq. 9.13 and is equal to $l^{zz} p'^2_z / m^2_{\psi(2S)}$.

Figure 9.1 plots $g(p', p) = g(p'(q), p(q))$ as a function of q. The scale factor is an angular momentum threshold effect. When q is a minimum (on the left in the figure), there is no extra energy available to make a d-wave ($p = 0$ implies $P'^{\mu} P'^{\nu} l_{\mu\nu} = 0$). Meanwhile, when q is maximum (on the right in the figure), the dipion is at rest in the $\psi(2S)$ frame and rotational symmetry requires an s-wave decay ($p' = 0$ implies $P'^{\mu} P^{\nu} l_{\mu\nu} = 0$). Figure 9.1 also indicates the minimum dipion mass cut at 340 MeV (where the solid line becomes a dotted line).

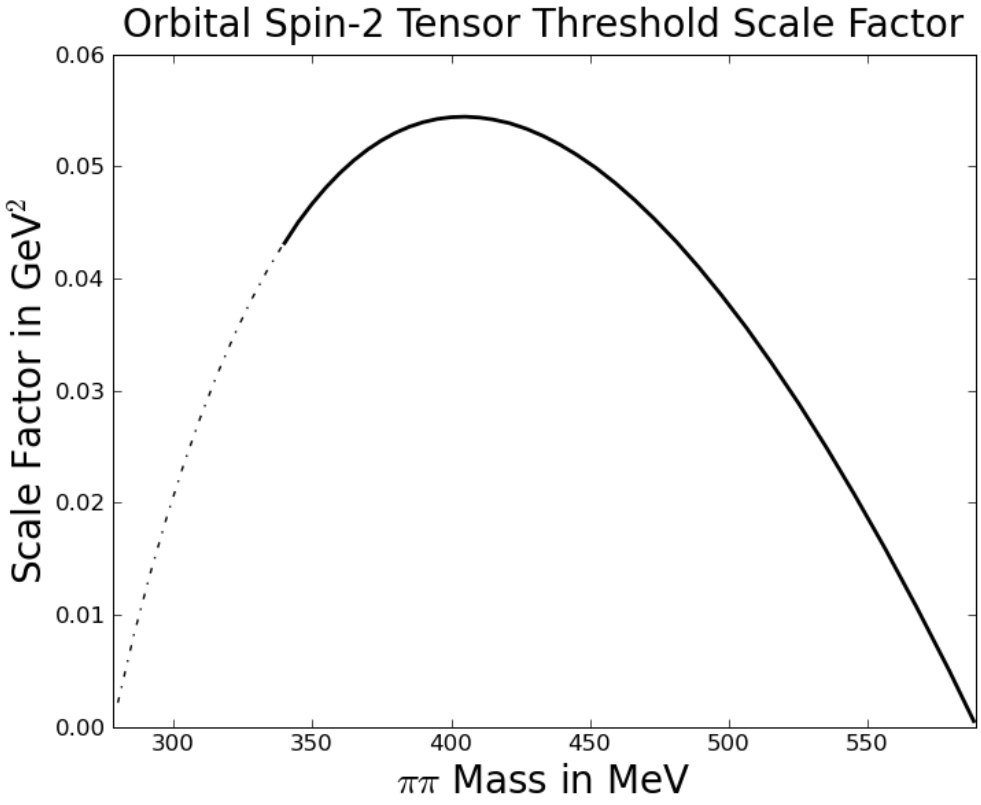

Figure 9.1: The $g(p', p)$ scale factor from eq. 9.21. The unit on the vertical axis is GeV^2. The minimum dipion mass is indicated at 340 MeV where the line switches from solid to dotted. The zeros at the endpoints disallow the d-wave (see text for details).

A few final thoughts are in order. The "energy dependant scale factor" that sits in

front the Wigner-d function is a relativistic correction. In general, whenever working with the non-relativistic helicity formalism, one could compute the scale factor and make the helicity amplitudes relativistic. This is the program advocated by S. U. Chung [23]. The debate is over how to how to define the amplitudes. The helicity formalism says one should measure $\mathcal{A}$ in

$$\mathcal{A}\, d^2_{00}, \tag{9.22}$$

Chung says you should measure $\mathcal{B}$ in

$$\mathcal{B}\, g(p', p) d^2_{00}. \tag{9.23}$$

and Filippini [22] says you should measure C in

$$C \frac{P'_\mu P'_\nu}{P'^2}\, l^{\mu\nu}. \tag{9.24}$$

The Filippini approach is equivalent to Chung in the sense that $\mathcal{B} = C$.

BIBLIOGRAPHY

[1] M. Oreglia *et al.* (Crystal Ball Collaboration), Phys. Rev. Lett. **45**, 959 (1980); H. Albrecht *et al.* (ARGUS Collaboration), Zeit. für Phys. **C35**, 283 (1987).

[2] J. Z. Bai *et al.* (BES Collaboration), Phys. Rev. **D62**, 032002 (2000).

[3] A. Rittenberg, UCRL-18863, Ph.D. Thesis (unpublished), 1969; G. W. London *et al.*, Phys. Rev. **143**, 1034 (1966); J. Badier *et al.*, Phys. Lett. **17**, 337 (1965).

[4] J. Z. Bai *et al.* (BES Collaboration), Phys. Lett. **B605**, 63 (2005); N. E. Adam *et al.* (CLEO Collaboration), Phys. Rev. Lett. **96**, 082004 (2006).

[5] C. Cawlfield *et al.* (CLEO Collaboration), Phys. Rev. **D73**, 012003 (2006).

[6] Exclusive ρ^0, ω, and ϕ Electroproduction. D.G. Cassel, *et al.*, Phys. Rev. **24**, 2787 (1981).

[7] D. Cronin-Hennessy *et al.* (CLEO Collaboration; CBX06-31 by R. S. Galik, S. P. Pappas and A. J. Weinstein), Phys. Rev. **D76**, 072001 (2007)

[8] S. R. Bhari *et al.* (CLEO Collaboration; CBX08-028 by T. K. Pedlar and S. R. Bhari), Phys. Rev. **D79**, 011103 (2009).

[9] B. Aubert *et al.* (BABAR Collaboration), Phys. Rev. Lett. **96**, 232001 (2006).

[10] K. F. Chen *et al.* (Belle Collaboration), Phys. Rev. Lett. **100**, 112001 (2008).

[11] B. Aubert *et al.* (BABAR Collaboration), Phys. Rev. **D71**, 052001 (2005).

[12] B. Aubert *et al.* (BABAR Collaboration), Phys. Rev. Lett. **95**, 142001 (2005); T. E. Coan *et al.* (CLEO Collaboration), Phys. Rev. Lett. **96**, 162003 (2006).

[13] H. Mendez *et al.* (CLEO Collaboration; CBX2008-019 by B. Heltsley and H. Mahlke), Phys. Rev. **D78**, 011102 (2008) .

[14] R. N. Cahn, Phys. Rev. **D12**, 3559 (1975).

[15] L. S. Brown and R. N. Cahn, Phys. Rev. Lett. **35**, 1 (1975).

[16] M. B. Voloshin, Phys. Rev. **D74**, 054022 (2006).

[17] M. B. Voloshin, Charmonium (2007), arXiv:0711.4556

[18] C. D. Froggatt and J. L. Petersen, Nucl. Phys. **B129**, 89 (1977).

[19] M. Paterno, `FERMILAB-TM-2286-CD` (2004)

[20] M. Galassi et al, GNU Scientific Lirary Reference Manual (3rd Ed.), ISBN 0954612078.

[21] R Development Core Team (2008). R: A language and environment for statistical computing. R Foundation for Statistical Computing, Vienna, Austria. ISBN 3-900051-07-0, URL http://www.R-project.org.

[22] V. Filippini, A. Fontana, and A. Rotondi, Phys. Rev. **D51**, 2247 (1995)

[23] S. U. Chung, Phys. Rev. **D48**, 1225 (1993)

[24] V. A. Novikov and M. A. Shifman, Z. Phys. C **8**, 43 (1981)